The Development of Components for Ultrafast All-Optical Communication Networks

Elisabeth Marley Koontz

B.S., Electrical Engineering
Southern Methodist University (1994)

S.M., Electrical Engineering and Computer Science
Massachusetts Institute of Technology (1996)

Submitted to the
Department of Electrical Engineering and Computer Science
in partial fulfillment of the requirements for the degree of

Doctor of Philosophy in Electrical Engineering

at the

MASSACHUSETTS INSTITUTE OF TECHNOLOGY

June 2000

© 2000 Massachusetts Institute of Technology
All Rights Reserved.

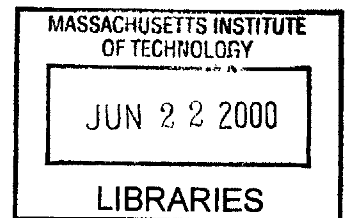

Author ______________________________
Elisabeth Marley Koontz
11 May 2000

Certified by ______________________________
Leslie A. Kolodziejski
Professor of Electrical Engineering
Thesis Supervisor

Accepted by ______________________________
Arthur C. Smith
Chair, Department Committee on Graduate Students
Department of Electrical Engineering and Computer Science

The Development of Components for Ultrafast All-Optical Communication Networks

by

Elisabeth Marley Koontz

Submitted to the Department of Electrical Engineering and Computer Science
on 11 May 2000, in partial fulfillment of the
requirement for the degree of
Doctor of Philosophy in Electrical Engineering

Abstract

The need for ultrafast (greater than 100 Gbps) all-optical communication networks is amplified as the amount of data-containing communication traffic continues to grow at an exorbitant rate. Multiplexing schemes are attractive, as they enable increased transmission over silica fiber already buried and in use. One of the key components enabling Wavelength Division Multiplexed (WDM) propagation is the distributed feedback (DFB) laser. A periodic index modulation, typically buried within the device structure (hence requiring an overgrowth step), is used to select the specific operating wavelength of the laser. As the WDM wavelength spacing continues to decrease, the increasing demands placed on the fabrication of the DFB lasers bring the fabrication issues to the forefront. Similar patterned surface overgrowth issues need to be addressed for realization of wavelength-selective filters, e.g. Bragg-resonant filters, for all-optical routing. Issues pertaining to the formation of buried index contrasts, for application to future WDM network components, are addressed.

Of importance to Time Division Multiplexed (TDM)-based propagation schemes is the multiplexing and demultiplexing of the ultrafast data streams. All-optical switching as well as optical (de)multiplexing are very attractive alternatives to optoelectronic conversion. Many optical switching schemes require the use of a semiconductor optical amplifier (SOA) as the nonlinear medium, as well as optical clock sources with repetition rates on the order of GHz (for integration with electronic components). For TDM network propagation rates on the order of Tbps, lasers must be capable of producing pulses shorter than a picosecond. Mode-locking of laser cavities is an attractive method of ultrashort pulse generation. A semiconductor saturable absorber mirror is a monolithically integrated device utilized for passive mode-locking of a wide variety of lasers. The development of SOAs as well as semiconductor saturable absorber mirrors is discussed.

Thesis Supervisor: Leslie A. Kolodziejski
Title: Professor of Electrical Engineering

Acknowledgements

The Massachusetts Institute of Technology is a unique institution. Time spent at MIT is generally conducted with one's head down, running full steam ahead, and looking up only occasionally to glimpse at the world outside. It is a place full of dichotomies; a place in which everyone is confident, yet everyone is intimidated. A place in which everyone is smart, yet never as smart as their colleague. A place in which everyone learns an enormous amount in very short period of time, yet it is not enough. The pursuit of a degree at MIT is also a dichotomy. The rewards are great upon leaving The Institution, however the arduous road to graduation will forever be ingrained in one's memory.

My time spent at MIT has been bittersweet at best. Were it not for the following individuals, my experience would have been much more bitter than sweet.

To Prof. Leslie A. Kolodziejski, I am eternally grateful. Thank you for giving me the opportunity to pursue my Ph.D. in your laboratory; were it not for you, I would not have made it through this place. You are an amazing individual, a fabulous advisor and boss, and most of all a wonderful friend. Please know that all you have endured has made you an amazing mentor, one that I can only hope to duplicate. Thank you for sharing your wisdom and experiences with me; you have taught me more than I could ever have hoped for!

To Dr. Gale S. Petrich, I can not thank you enough. We have learned a great deal from one another, and persevered though times that have made us both better people. Thank you for all of the time you invested in me with regard to the laboratory; you are a very wise man in the world of engineering. Thank you for all of the time you spent writing the many Matlab scripts for x-ray data and miscibility gap graphing. Thank you also for being a sounding board for x-ray discussions, and for your assistance with the interpretation of those equation things.

To Erik R. Thoen, you are a GREAT pal. Thank you for being a wonderful colleague; it has been a pleasure to work with you. You have taught me a lot, even though you're a "young punk". Thanks also for being a sounding board - we're finally allowed off of this joyous roller coaster!

To my thesis committee: Prof. Erich P. Ippen, Dr. Katherine L. Hall, and Prof. Mark S. Goorsky. Thank you for sitting on my committee and for all of your time invested in our collaborative projects. You all have taught me a great deal - thank you.

To Kuo-Yi Lim, my officemate for a large part of my MIT experience; thank you for being a great friend and enduring my early MIT years.

To Dan Ripin, a great tutor and good friend. It was a pleasure to work with you on the SBR project. Best of luck in your remaining time at MIT.

To Sandra Brown, an "old, bitter grad student" cohort. You have finally escaped - run like the wind!

To Dr. Gary Evans, Dr. Zeynep Çelik-Butler, and Dr. Carlos Davila at SMU: thank you for encouraging me to pursue advanced degrees in Electrical Engineering. Were it not for you all, I would not have attended MIT.

To Juliet Gopinath and Aleksandra Markina; although our overlap was brief, it was a pleasure to work with you both. Find a good support network; someone with which to be bitter will become increasingly important.

Research performed on the semiconductor saturable absorber mirror effort was a strong collaboration between the laboratories of Prof. Kolodziejski and Prof. Ippen. For this reason, a number of individuals contributed to the work: E.R. Thoen, F.X. Kärtner, P. Langlois, M. Joschko, T. Schibli, M.E. Grein, and J.T. Gopinath. All ultrafast optical characterization, fiber laser implementation, and various aspects of the structure design were performed in Prof. Ippen's laboratory. Theoretical analysis of the laser stability against Q-switched-mode-locking was accomplished in large part by F.X. Kärtner, E.R. Thoen, and T. Schibli. Dynamic differential reflectivity measurements and saturation fluence measurements were performed by E.R. Thoen, P. Langlois, M. Joschko, and J.T. Gopinath. Application of the saturable absorber mirror structures to fiber lasers was carried out by E.R. Thoen and M.E. Grein.

Many thanks is extended to those at Lincoln Laboratory, past and present, that were of great assistance in various ways. Thanks to C.C. Cook for depositing dielectric coatings on the semiconductor saturable absorber mirrors. Thanks for J.P. Donnelly, K.L. Hall, and M. Kuznetov for semiconductor optical amplifier designs and discussions. Thanks to D. Calawa for triple axis x-ray diffraction measurements.

The gratings utilized for buried index contrast structures were provided by M.H. Lim in Prof. Henry I. Smith's laboratory at MIT. Thanks is also extended to M.H. Lim for many SEM images.

Many of the reciprocal space maps generated for this thesis were created in Prof. M.S. Goorsky's laboratory at UCLA. Many thanks to M.S. Goorsky, G.D. U'Ren, and K.M. Matney for obtaining the data.

Thanks is also extended to J.L. House for preparation of the TEM samples, E.L. Shaw for operation of the sputtering Auger and AFM systems, and A. Garrett-Reed for TEM operation.

This document would not have been possible were it not for my family and friends who encouraged me to pursue my education. To Jill, my progressing 'type A' buddy - everything you ever wanted to know about optothermoelectronics, AND MORE, is finally published! To the Doughertys and Kolodziejskis - our family away from home (complete with virtual children); thanks for being who you are. To Mike and Steve - thanks for your love and encouragement; your geeky sister will finally get a "real" job. To Mom and Dad - thank you for your enduring love and support. And to my husband, Carl - the best combination chef and bartender in the world; this document is more yours than mine!

Contents

1 Introduction **17**

1.1 Motivation 17
1.2 Thesis Overview 19

2 Gas Source Molecular Beam Epitaxy of (In,Ga)(As,P) Materials **21**

2.1 (In,Ga)(As,P) Materials 21
2.2 Gas Source Molecular Beam Epitaxy 23

3 GSMBE Deposition on Atomic Hydrogen-Cleaned Surfaces **47**

3.1 Low Temperature Atomic Hydrogen-Assisted Oxide Removal 47
3.2 Regrowth of InP/InGaAs Heterostructures and Quantum Wells on GaAs-Terminated Distributed Bragg Reflectors 48
3.3 Low Temperature Atomic Hydrogen-Assisted Oxide Removal from Rectangular-Patterned Surfaces 53

4 Overgrowth of Submicron-Patterned Surfaces for Buried Index Contrast Devices **59**

4.1 Overgrowth of Sawtooth-Patterned Surfaces: A Review 61
4.2 Overgrowth of Rectangular-Patterned Surfaces 66
4.3 Patterned Surface Overgrowth Models 89

5 Development of Semiconductor Saturable Absorber Mirrors for Mode-Locked Lasers **95**

5.1 Mode-Locking, Q-Switching, and Q-Switched-Mode-Locking: A Brief Overview . . 95
5.2 Passive Mode-Locking via Semiconductor Saturable Absorber Mirrors 97

6 Development of Semiconductor Optical Amplifiers for All-Optical Switching Techniques **111**

6.1 Semiconductor Optical Amplifiers for All-Optical Switching 112
6.2 The Ultrafast Nonlinear Interferometer 115
6.3 Semiconductor Optical Amplifier Designs for the UNI 116

7 Summary and Future Work **127**

7.1 Accomplishments 127
7.2 Suggestions for Future Work 129

Appendix A Triple Axis X-ray Diffractometry and Reciprocal Space Mapping 131

A.1 Diffraction Theory 131
A.2 X-ray Diffractometry 134
A.3 Reciprocal Space Mapping 145

References **149**

List of Figures

Figure 1.1 Graph of current and forecasted Internet-related traffic on the communications network in North America. Figure from [1]. 17

Figure 2.1 Diagram of semiconductor material bandgap versus lattice constant. The black line indicates InGaAsP compositions lattice-matched to InP. 22

Figure 2.2 (a) 3-D, or bulk, electron diffraction from a rough InP surface. (b) Electron diffraction from an ordered, yet rough, surface. (c) 2-D, or surface, electron diffraction from a smooth InP surface along [01 1]. 27

Figure 2.3 4-fold RHEED pattern from an InP surface along [011]. 28

Figure 2.4 Diagram of the integrated II-VI/III-V system. All samples are introduced into the system via the Introduction Chamber. 29

Figure 2.5 Diagram of the photoluminescence setup used for measurements presented in this thesis. The highpass filter passes wavelengths greater than 550 nm. 33

Figure 2.6 (a) Nomarski microscopy image (200x magnification) of ~2 μm InP (lightly Si-doped) deposited on an InP substrate. Growth conditions: rate ~ 0.7 μm/hr, Tsub ~ 480°C, chamber pressure ~ $3x10^{-5}$ Torr, and V/III ~ 10. (b) Nomarski microscopy image (200x magnification) of ~0.17 μm InP and ~0.07 μm InGaAs deposited on an InP substrate. Growth conditions for InP: rate ~0.35 μm/hr, Tsub ~470°C, chamber pressure ~$1.9x10^{-5}$ Torr, V/III ~ 13. The ramped nucleation procedure was utilized in (b) only. 35

Figure 2.7 Nomarski microscopy image (200x magnification) of ~0.25 μm of InP (and 2 InGaAs quantum wells) deposited on a GaAs substrate. Growth conditions for InP: rate ~0.35 μm/hr, Tsub ~470°C, chamber pressure ~$1.9x10^{-5}$ Torr, V/III ~ 13. Note: the surface is slightly rough, but not unexpected due to the large lattice-mismatch. 37

Figure 2.8 Nomarski microscopy image (200x magnification) a typical AlGaAs/GaAs surface grown by GSMBE. 500 nm of $Al_{(1-x)}Ga_xAs$ (x ~ 0.85) deposited on GaAs. 38

Figure 2.9 Calculation of the miscibility gap for InGaAsP materials, using the regular solution approximation for the solid solution (after [40]). The area within each ring designates the miscibility gap for a given substrate temperature. The diagonal line represents the compositions of InGaAsP lattice-matched to InP [following Eq. (2.4)]. The filled-in circles are compositions that have been deposited in the GSMBE system at MIT. 470°C is the approximate substrate temperature used for layers and structures presented in this thesis. 41

Figure 2.10 PL at various temperatures for ~280 nm of $In_{(1-x)}Ga_xAs_yP_{(1-y)}$ (x ~ 0.12, y ~ 0.3), slightly compressive-strained. Graphs are offset for clarity. 42

Figure 2.11 PL measurements at multiple temperatures illuminating the spectral dependence of compositional modulation. Sample (b) is a compressive-strained InGaAsP (x~0.25, y~0.7) layer just inside the calculated miscibility gap. Sample (e) is a lattice-matched InGaAsP (x~0.33, y~0.7) layer within the calculated miscibility gap. Sample (h) is a tensile-strained InGaAsP (x~0.4, y~0.7) layer within the miscibility gap. Sample (i) is a tensile-strained InGaAsP (x~0.25, y~0.37) layer just inside the calculated miscibility gap. Figure from [13]. 43

Figure 2.12 PL at various temperatures for ~ 470 nm of $In_{1-x}Ga_xAs$ (x ~ 0.494), slightly tensile-strained. Graphs are offset for clarity. Peaks labeled "G" correspond to GaAs-rich features, peaks labeled "N" correspond to the expected InGaAs features, and peaks labeled "I" correpond to InAs-rich features. . . . 43

Figure 2.13 PL at various temperatures for ~200 nm of $In_{1-x}Ga_xAs$ (x ~ 0.47), deposited on InP. Graphs are offset for clarity. Peak labeled "N" is attributed to the average InGaAs composition. 45

Figure 3.1 (a) ~245 nm of InP, containing two InGaAs quantum wells centered ~220 nm from the GaAs, deposited on a GaAs/AlAs DBR. (b) ~245 nm of InP, containing four quantum wells centered within the InP layer, deposited on a GaAs/AlAs DBR. 49

Figure 3.2 Nomarski contrast microscopy image of ~ 250 nm of InP (containing two InGaAs quantum wells) deposited on a GaAs-terminated DBR. Magnification is 200x. 50

Figure 3.3 300K PL spectrum of ~250 nm of InP containing two InGaAs quantum wells (centered ~ 220 nm from the GaAs-InP interface) deposited on GaAs. 51

Figure 3.4 HRDAXD scan of a ~250 nm InP/InGaAs region deposited on a GaAs/AlAs DBR. 51

Figure 3.5 Auger Electron Spectroscopy scans of a patterned InP surface and the surface of an InP epi-ready wafer. The relative magnitude of elements on the surface of both samples is nearly identical. 54

Figure 3.6 (a) Scanning electron micrograph of an InP rectangular-patterned grating. (b) (400) reciprocal space map of the grating shown in (a). 54

Figure 3.7 {422} reciprocal space map of the corrugated InP surface shown in Figure 3.6(b). 55

Figure 3.8 TAD (400) $\Delta\omega$ scan for InGaAsP grown on a rectangular-patterned InP grating. The grey line is data obtained from a sample exposed to a P_2 flux prior to nucleation, whereas the black line is data obtained from a sample exposed to an As_2/P_2 flux mixture. 56

Figure 3.9 (a) SEM of a thermally cleaned InP grating. (b) SEM of a low temperature atomic hydrogen-cleaned InP grating. On both samples, the overlayer is InGaAs nominally lattice matched to InP. 57

Figure 3.10 Sputtering Auger electron spectroscopy scan of an InGaAs/patterned-InP-surface interface. The absence of both C and O suggests a very clean patterned InP surface prior to overgrowth. 58

Figure 3.11 Auger electron spectroscopy scan of the surface of an InP grating prior to any pre-epitaxy cleaning. Surface concentrations of C and O are ~58% and ~12%, respectively. 58

Figure 4.1 Calculated power in the dropped channel for a Bragg-resonant channel-dropping filter. (a) Calculated power for resonators with rectangular index modulations and (b) for resonators with sinusoidal index modulations. Calculation by J.N. Damask, MIT. 61

Figure 4.2 (a) Diagram of a sawtooth-patterned corrugation with (h11)A sidewalls. (b) Diagram of (a) following mass-transport alteration of the grating profile. 61

Figure 4.3 Cross-sectional transmission electron microscopy image of (a) InGaAsP deposited via OMVPE on a preserved sawtooth-patterned InP grating, and (b) a DFB laser structure deposited via OMVPE on a "smoothed" sawtooth-patterned InP grating. Images from [74]. 62

Figure 4.4 Schematic illustration of the proposed overgrowth of InGaAs(P) on submicron period sawtooth-patterned (100) InP substrates containing (h11)A sidewalls. The starting grating pattern in InP is outlined in black. 63

Figure 4.5 Schematic diagram of a generic overgrown structure on a rectangular-patterned surface. (*w*: tooth width at the tooth midpoint, *d*: tooth depth, Γ: grating width, Λ: grating period, *t*: overgrown layer thickness). 67

Figure 4.6 10K PL spectra of InP deposited on: untreated InGaAsP epilayer (black line), 30 sec. wet chemically etched InGaAsP epilayer (dark gray line), InGaAsP epilayer with ~100 nm removed via RIE (gray line), and ~100 nm-deep InGaAsP gratings (light gray line). Data is offset for clarity. 68

Figure 4.7 (a) SEM image of gratings fabricated in an InGaAsP epilayer. (b) (400) RSM of the gratings depicted in (a). (c) {422} glancing exit RSM of ~1 μm of InP deposited on the InGaAsP gratings depicted in (a). Intensity scale for (b) and (c) is $1\text{-}1\times10^4$. 69

Figure 4.8 AFM images of ~1 μm of InP deposited on the InGaAsP gratings shown in Figure 4.7(a). The white line in the image to the right is the profile of the gratings traced from Figure 4.7(a). 70

Figure 4.9 (a) (400) RSM of ~210 nm of InGaAsP deposited on a planar InP substrate. (b) (400) RSM of ~210 nm of InGaAsP deposited on rectangular-patterned InP gratings. Intensity scale is $1\text{-}1\times10^4$. 73

Figure 4.10 $\Delta q_x = 0$ scans (θ/2θ scans) of the planar sample (from Figure 4.9(a), gray line) and of the grating overgrowth sample (from Figure 4.9(b), black line). Data is offset for clarity. 74

Figure 4.11 {422} RSM of ~210 nm of InGaAsP deposited on rectangular-patterned InP gratings. The white lines indicate diffraction envelope shifts. The intensity scale is $1\text{-}1\times10^4$. 75

Figure 4.12 Glancing incidence {422} RSM of ~210 nm of InGaAsP deposited on an InP rectangular-patterned grating. The x-rays are incident parallel to the surface corrugation. The analyzer and monochrometer streaks are a function of the TAD measurement setup [57]. Both streaks are apparent due to the dispersive arrangement of the TAD system during this measurement. 76

Figure 4.13 (a) HRDAXD of ~200 nm of InGaAs deposited on a preserved rectangular-patterned InP grating (black curve). The gray curve is data obtained from the simultaneously grown planar monitor sample. A SEM of the sample is depicted in Figure 3.9(b). (b) HRDAXD data from ~200 nm of InGaAs deposited on a slightly altered rectangular-patterned InP surface. A SEM of the sample is depicted in Figure 3.9(a). The gray curve is data obtained from the simultaneously grown planar monitor sample. 78

Figure 4.14 10K PL spectrum of ~200 nm InGaAs deposited on a preserved InP rectangular-patterned grating. See Figure 3.6(b) for a cross-sectional SEM of the sample. 79

Figure 4.15 Schematic illustration of the overgrowth process of InGaAs(P) on rectangular-patterned (100) InP surfaces. 79

Figure 4.16 300K PL spectra of ~210 nm of InGaAsP deposited on a preserved InP grating (black line) and the simultaneously grown monitor sample (gray line). 82

Figure 4.17 (a) X-ray topography measurement of ~210 nm of InGaAsP deposited on an InP rectangular-patterned grating. The absence of distinct features suggests material of good quality having a low defect density. (b) X-ray topography measurement of InGaAs deposited on an InP substrate. The distinctive lines indicate the presence of misfit dislocations. 83

Figure 4.18 Scanning transmission electron microscopy measurement of the sample analyzed in Figure 4.9(a); ~210 nm of InGaAsP deposited on an InP substrate. 84

Figure 4.19 TAD-generated {311} glancing exit RSM of $In_{(1-x)}Ga_xAs_yP_{(1-y)}$ ($x \sim 0.12$, $y \sim 0.3$) overlayer on a rectangular-patterned InP grating. RSM intensity scale is $1\text{-}2.5\times10^3$. 84

Figure 4.20 TAD-generated (400) RSM of $In_{(1-x)}Ga_xAs_yP_{(1-y)}$ ($x \sim 0.12$, $y \sim 0.3$) overlayer on a rectangular-patterned InP grating. RSM intensity scale is $1\text{-}1 \times 10^4$. 85

Figure 4.21 An extreme example of roughness in the grating trenches of ~230 nm period InP gratings fabricated via RIE. 86

Figure 4.22 ~230 nm period gratings fabricated in an InGaAsP epilayer; gratings have been wet chemically etched for entry into the GSMBE system. The roughness apparent in the grating trenches detrimentally affects the quality of an InP overlayer. 86

Figure 4.23 (400) RSM of ~275 nm InP deposited on the InGaAsP grating shown in Figure 4.22. Intensity scale is $1\text{-}1 \times 10^4$. 87

Figure 4.24 SEM image of the ~230 nm period InP gratings discussed in Section 4.2.2. The gratings have been degreased and wet chemically etched following RIE. Note the smoothness of the grating trenches. 88

Figure 4.25 Scanning electron micrograph of InGaAsP gratings with a thin layer of the Ti etch mask remaining on the grating teeth. 88

Figure 4.26 Normarski interference contrast microscopy image of ~3.5 µm of InP deposited on InGaAsP having a thin layer of the Ti etch mask on the InGaAsP surface (200x magnification). The rough edge apparent in the photo is the edge of the Ti mask. 89

Figure 4.27 Schematic of deposition in rectangular trenches and on mesas as determined via the numerical model developed by Biasol and Kapon. Figure from [89]. The sl superscripts represent the self-limiting widths; $\Delta r = r_s - r_b$. 90

Figure 4.28 Calculation of the variation in the Ga diffusion length for different surface orientations. Figure from [110]. 92

Figure 4.29 Schematic of GaAs deposition on a 0.5 µm GaAs rectangular mesa as determined via the numerical model developed by Ohtsuka. Figure from [110]. 92

Figure 5.1 Measured transmission spectrum of a 22-pair GaAs/AlAs DBR. 99

Figure 5.2 Saturable absorber design in which the absorbing quantum wells are located near the null of the electric field (at $\lambda \sim 1.54$ µm) within the structure. The electric field is calculated as a function of position from the GaAs substrate; in order to obtain the intensity within the structure the electric field should be multiplied by the refractive index. A dielectric antireflection coating is also present on this structure. 100

Figure 5.3 Saturable absorber design in which the absorbing quantum wells are located near the maximum of the electric field (at $\lambda \sim 1.54$ µm) within the structure. The electric field is calculated as a function of position from the GaAs substrate; in order to obtain the intensity within the structure the electric field should be multiplied by the refractive index. A 5-layer dielectric resonant coating is also present on this structure. 101

Figure 5.4 Saturation fluence measurement of the structure shown in Figure 5.2. The inset depicts the pump-probe measurement at ~80 µJ/cm^2. 102

Figure 5.5 Saturation fluence measurements of the structure depicted in Figure 5.3. Inset (i) is a pump-probe measurement at ~10 µJ/cm^2; inset (ii) is a pump probe measurement at ~200 µJ/cm^2. 102

Figure 5.6 Calculated stability contours for a fast saturable absorber mode-locked laser. Q-switched mode-locking is present in regions labeled "Unstable". The area within the dotted line is the unstable region with TPA included in the model. 104

Figure 5.7 Diagram of the mode-locked fiber laser containing an Er/Yb codoped phosphate glass waveguide as the amplifying medium. 105

Figure 5.8 Schematic of an actively harmonically mode-locked fiber laser stabilized with a TPA structure. 106

Figure 5.9 Simulation of the reflectivity spectrum of a 6-pair GaAs/Al_xO_y DBR. The dark trace assumes 10% contraction of the Al_xO_y layer resulting from the oxidation process. 108

Figure 5.10 Nomarski interference contrast image (200x magnification) of the surface of the structure depicted in Figure 5.2. The slip lines and wire-like pieces are the result of oxidation of the AlAs layers in the DBR. 109

Figure 6.1 Depiction of the three regimes of operation for a SOA. 113

Figure 6.2 (a) Calculated phase response of a SOA a a continuous train of intense pulses. (b) Calculated phase response of a SOA to a variable train of intense pulses. Figures from [165]. 114

Figure 6.3 Diagram of the ultrafast nonlinear interferometer (UNI). PSI is polarization-sensitive isolator, SOA is semiconductor optical amplifier, BRF is birefringent fiber, and PC is polarization controller. . 115

Figure 6.4 Diagram of strain effects on energy band arrangements in semiconductor materials. Diagram after [109]. 117

Figure 6.5 Schematic of the current SOA structure under development. 120

Figure 6.6 (a) 3-D mode solver solution for a TE mode supported in a 2.5 μm ridge SOA structure (structure depicted in Figure 6.5). Depicted is the electric field intensity. (b) Horizontal and (c) vertical cross-section of the TE mode intensity graphed along with the index profile of the structure. 121

Figure 6.7 (a) 3-D mode solver solution for a TM mode supported in a 2.5 μm ridge SOA structure (structure depicted in Figure 6.5). Depicted is the electric field intensity. (b) Horizontal and (c) vertical cross-section of the TM mode intensity graphed along with the index profile of the structure. 122

Figure 6.8 Diagrams of the simulated electric field amplitude for the TE mode and TM mode in the SOA structure of Figure 6.5. 123

Figure 6.9 Schematics of other double heterostructure SOA designs being considered. 123

Figure A.1 Geometric representation of Bragg's Law. The path length difference between two layers is *ABC*. 132

Figure A.2 Geometrical representation of the Ewald sphere construction. 133

Figure A.3 The Ewald sphere constructed in reciprocal space. The (400) diffraction conditions are not satisfied in (a). The (400) diffraction conditions are satisfied in (b). Figure from [177]. 134

Figure A.4 Diagram of available diffraction conditions for (100) Si. 134

Figure A.5 Geometrical depiction of diffraction of an incident source having a linewidth $\beta_{1/2}$ due to an angular deviation, ε, from the Bragg condition. Figure from [31]. 135

Figure A.6 Basic diffraction geometries for symmetric and asymmetric arrangements. 136

Figure A.7 Diagram of diffraction geometries. 137

Figure A.8 General high-resolution double axis x-ray diffraction arrangement. 138

Figure A.9 Rocking curves depicting the increased beam conditioning obtained with an increase in the number of diffractions from a (220)-oriented Si crystal. Figure from [177]. 139

Figure A.10 Arrangement for a (400) θ/2θ scan in reciprocal space. An example of a double axis θ/2θ measurement of an InGaAsP ($x \sim 0.42, y \sim 0.81$) epilayer deposited on an InP substrate is shown to the right. 140

Figure A.11 An asymmetric {422} $\theta/2\theta$ scan depicted in reciprocal lattice space. 142

Figure A.12 Generic diagram of a triple axis x-ray diffractometry system. The conditioning crystals are typically configured in either a 2- or 4-bounce arrangement. Likewise, the analyzer crystal is typically configured in either a 2- or 4-bounce arrangement (or possibly a 3-bounce arrangement, depending on the crystal material). 143

Figure A.13 Diagram of the Bede D^3 diffractometer used at UCLA. 143

Figure A.14 Generic reciprocal space diagrams of reciprocal space map generation. 145

Figure A.15 Depiction of relaxation and curvature directions in asymmetric RSMs. Note, the figure on the left is a glancing incidence arrangement and the figure on the right is glancing exit. 146

Figure A.16 (a) (400) RSM of a rectangular-patterned InP substrate measured on a Philips MRD at Lincoln Laboratory. (b) (400) RSM of the same patterned substrate measured on the Bede D^3 at MIT. 147

Figure A.17 Geometrical depiction of $\Delta\omega$ and $\Delta\theta$ for Δq-space conversion. 147

1

Introduction

1.1 Motivation

The need for ultrafast (greater than 100 Gbps) all-optical communication networks is amplified as the amount of data-containing communication traffic continues to grow at an exorbitant rate. Within North America, market research indicates that the volume of data traffic has surpassed that of voice traffic on the telecommunications network [1]. Shown in Figure 1.1 is the current and forecasted Internet-related data traffic. Current terrestrial communication networks combine the well-developed electronic components

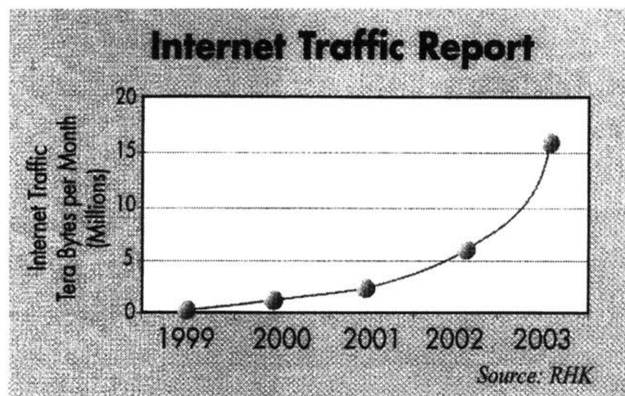

Figure 1.1 Graph of current and forecasted Internet-related traffic on the communications network in North America. Figure from [1].

(i.e. switching and routing) with the more recent optical propagation schemes. The method chosen to address the need to increase the aggregate data rate of the networks, in order to meet the demands driven in large part by the Internet, is to multiplex the data. Two standard (de)multiplexing schemes are geared towards terrestrial communication networks: wavelength division multiplexing (WDM) and time division

multiplexing (TDM). Multiplexing schemes are attractive, as they enable increased transmission over silica fiber already buried and in use.

Although WDM systems are in the process of being implemented, aggregate data rates may be limited by electronic signal processing speeds at the originating and terminating ends of the fiber transmission lines. The upper limit for operating speeds of electronic components is not yet established, however it is currently lower than achievable optical transmission speeds. The ability to move away from electronic processing and towards all-optical processing of the network-level data is attractive due to the simplicity of integration and the possible elimination of optoelectronic conversion.

In order to eliminate electronic processing on the network level, all-optical processing components must transfer, store, and rate-convert all data to and from the data rate of the source (i.e. a computer or a router) to the network data transmission rate. Thus, components such as passive wavelength-selective routers and all-optical switching mechanisms need to be implemented. Additionally, ultrafast (femtosecond) optical sources providing high bit data and clock rates are required for network transmission rates greater than 1 Tbps.

The multiplexing of a data segment, or word, onto multiple wavelengths allows an N times increase in the network transmission rate, where N is the number of wavelengths. Current systems (i.e. the WaveStar 400G manufactured by Lucent Technologies [2]) support 80 wavelengths in which the data carried by each wavelength has a base data rate of 2.5 Gbps (OC-48), making the effective transmission rate 200 Gbps. The WaveStar can also support OC-192 transmission rates (10 Gbps), and will multiplex 40 channels for an aggregate data rate of 400 Gbps. Although the severity is not yet clear, a future limitation of WDM is the minimum achievable spacing between the wavelength channels. In order to more closely space the channels, issues such as the linewidth of the optical source and the ability to maintain signal-to-noise ratios must be addressed. Furthermore, the selectivity of all-optical devices within the network must match that of the channel spacing. Thus, both material quality and fabrication techniques of the network components affect the ultimate network performance.

One of the key components enabling WDM propagation is the distributed feedback (DFB) laser. A periodic index modulation, typically buried within the device structure (hence requiring an overgrowth step), is used to select the specific operating wavelength of the laser. Although DFB lasers have been commercially available for more than 10 years, fabrication of these devices is still problematic. Furthermore, as the WDM wavelength spacing continues to decrease, the increasing demands placed on the fabrication of the DFB lasers bring the fabrication issues to the forefront. Similar patterned surface overgrowth issues need to be addressed for realization of wavelength-selective filters, e.g. Bragg-resonant filters, for all-optical routing. For closely spaced wavelength channels, the selectivity of the filters must likewise increase. Thus, issues pertaining to the corrugation definition (via lithography) as well as to the overgrowth (in regards to profile alteration) must be addressed for realization of future WDM network components.

Time division multiplexing of data streams has similar bandwidth requirements as does the WDM scheme. TDM propagation schemes, like WDM, can consist of multiple data streams propagating at lower

data rates. The multiplexing in this instance is performed in the time domain, i.e. bit interleaving or slot allocation. Various TDM-based network geometries have been developed in recent years, such as the helical local area network (HLAN) [3] and an all-optical packet routing architecture [4]. Of importance to TDM-based propagation schemes is the multiplexing and demultiplexing of the ultrafast data streams. In existing systems, for propagation rates on the order of Tbps, the data must be optically demultiplexed to data rates that the electronic components can process. Optoelectronic conversion must be performed not only at the edges of the network (i.e. for interfacing with a computer) but also along the network for switching and routing functions. All-optical switching as well as optical (de)multiplexing are very attractive alternatives to optoelectronic conversion. Optical switching and demultiplexing of TDM data has recently been demonstrated via various interferometric techniques (i.e. ultrafast nonlinear interferometers, semiconductor laser amplifiers in a loop mirror, etc.). Many optical switching schemes require the use of a semiconductor optical amplifier (SOA) as the nonlinear medium, as well as optical clock sources with repetition rates on the order of GHz (for integration with electronic components).

For TDM network propagation rates on the order of Tbps, lasers must be capable of producing pulses shorter than a picosecond. One method of ultrashort pulse generation in laser cavities is mode-locking. Mode-locking forces the temporal modes in a cavity to propagate in phase, and can be instigated either actively or passively. Passive mode-locking is typically preferred primarily due to ease of implementation and lack of external control. A semiconductor saturable absorber mirror is a monolithically integrated device utilized for passive mode-locking of a wide variety of lasers. The monolithic integration of an absorber with a mirror enables the replacement of a high reflector in a laser cavity with the absorber mirror, effectively leaving the number of components in the laser cavity unchanged.

Entrenched in the requirements for the realization of all-optical communication networks is the need for a highly nonlinear medium suitable for ultrafast switching. In order to implement all-optical networking schemes, the current switching, storage, clock recovery, etc. accomplished by electronic components must be performed in the optical domain. In recent years, various all-optical switching techniques utilizing semiconductor optical amplifiers (SOAs) have been demonstrated at reported data rates up to 1.5 Tbps [i.e. 5,6,7,8]. More recently, monolithic integration of all-optical switching schemes has been accomplished in InP-based materials [i.e. 9]. Requirements placed on the SOAs include the need for polarization insensitivity and as well as large intensity induced nonlinearities in the shortest possible device lengths.

1.2 Thesis Overview

This thesis addresses many aspects of the development of semiconductor components for all-optical communication networks. The ability to master the use of gas source molecular beam epitaxy (GSMBE) to realize devices based in InP and GaAs materials systems is a large part of this thesis, and will be discussed in detail in Chapter 2. The use of a low temperature atomic hydrogen-assisted oxide removal technique for both regrowth on GaAs/AlAs structures as well as overgrowth of surface corrugations in In(Ga,As)P

materials is addressed in Chapter 3. The realization of buried index contrasts, in which the modulation is unaltered from the fabricated profile, has been accomplished via the use of a low temperature atomic hydrogen-assisted oxide removal process and GSMBE. Preservation of the fabricated profile affords increased flexibility in device design as well as an anticipated decrease in compositional modulation in the deposited overlayer. Analysis of the resulting structures containing buried-index contrasts is addressed in Chapter 4. The design of semiconductor saturable absorber mirrors for implementation in fiber-based laser cavities is presented in Chapter 5. Preliminary development of SOAs for implementation in an ultrafast nonlinear interferometer has also been investigated; associated preliminary designs and simulations are presented in Chapter 6. Finally, Chapter 7 encompasses a summary as well as suggestions for extensions of the work discussed in this thesis.

2

Gas Source Molecular Beam Epitaxy of (In,Ga)(As,P) Materials

The use of Gas Source Molecular Beam Epitaxy (GSMBE) for the realization of high speed communication components, both optical and optoelectronic, is the backbone of this thesis. Specifically, the ability to utilize GSMBE for deposition of (In,Ga)(As,P) materials on both InP and GaAs substrates, either planar or patterned, is addressed. Both the growth technique and the subsequent analysis (both *in-situ* and *ex-situ*) of the resulting material and/or structures will be discussed. Thus far, specific issues being addressed in regard to materials growth include the effect of the oxide desorption technique and V/III ratio on the generation of defects.

2.1 (In,Ga)(As,P) Materials

The ability to deposit high quality InP-based materials for the fabrication of optical devices is an important aspect of the development of all-optical communication network components. The central material of interest is $In_{1-x}Ga_xAs_yP_{1-y}$; these quaternary materials are quite attractive due to the wide range of achievable bandgaps with lattice constants matching that of an InP substrate (0.75eV of InGaAs to 1.35eV of InP). Depicted in Figure 2.1 is the bandgap versus lattice parameter space for a wide range of materials. The solid line indicates the range of InGaAsP materials with the same lattice constant as InP. With the current state of the communications market, the demand for InP-based emitters and detectors exceeds that able to be supplied [10]. Additionally, performance specifications for both optical and electrical devices are placing ever more stringent requirements on the materials growth and fabrication processes used to realize the devices [11]. Unlike GaAs, which has been investigated in detail for material

properties as well as device implementation, deposition of InGaAsP is still plagued with issues as basic as substrate quality (many manufacturing lines still use 2"-diameter InP wafers whereas GaAs manufacturing lines are moving to 6"-diameter wafers). Furthermore, deposition of InGaAsP is inherently more difficult strictly due to the need to precisely control the deposition rate and relative ratio of four elements, two of which are group V elements; in comparison, materials typically deposited on GaAs contain only a single group V element. InGaAsP is also susceptible to spinodal-like decomposition; given the correct (or incorrect) growth parameters, an epilayer can experience lateral compositional modulation with the result being GaP- and InAs-rich regions throughout the layer [12,13]. Although growth parameter dependent, InGaAsP having λ~1.1-1.3 μm is often quoted as being the most difficult quaternary to deposit [14]. However, reports have also been published in regards to difficulty in depositing InGaAsP with λ near 1.55 μm, especially if the quaternary is tensile-strained [13]. Even though much is known about the deposition of InGaAsP materials, much is yet to be determined in order to fabricate new devices to meet the demands of the communication-based industry.

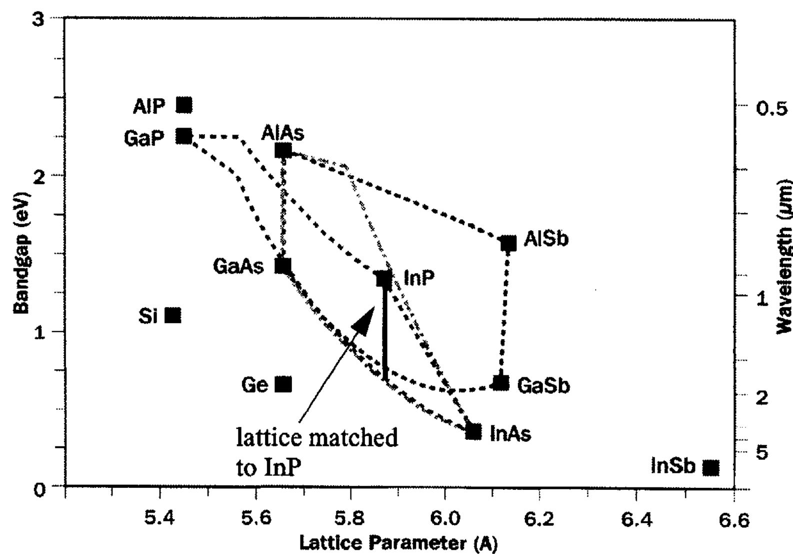

Figure 2.1 Diagram of semiconductor material bandgap versus lattice constant. The black line indicates InGaAsP compositions lattice-matched to InP.

2.1.1 Molar Composition Determination

As can be seen from Figure 2.1, the range of bandgaps for which InGaAsP is lattice-matched to InP is determined by the relative concentration of the four elements. In addition to being concerned about the bandgap, the lattice constant must also be taken into consideration. The ratio of both the group III elements and the group V elements must be set in order to obtain the desired bandgap and lattice constant.

For the derivation of various material properties of ternaries and quaternaries, a linear interpolation, dependent on the binary compounds that compose the material, is generally a reasonable approximation when experimentally determined expressions are not available. The equations for ternary and quaternary compounds of $A_xB_{1-x}C$ and $A_xB_{1-x}C_yD_{1-y}$ are:

$$P(A_xB_{1-x}C) = xP_{AC} + (1-x)P_{BC} \qquad \text{Eq. (2.1)}$$

$$P(A_xB_{1-x}C_yD_{1-y}) = xyP_{AC} + x(1-y)P_{AD} + y(1-x)P_{BC} + (1-x)(1-y)P_{BD} \qquad \text{Eq. (2.2)}$$

where P is any material property that can be interpolated. These equations may be used in general for calculating material properties such as lattice constant, refractive index, elastic stiffness constants, etc. The linear variation in lattice constant with respect to composition is known as Vegard's Law [15], and for $In_{1-x}Ga_xAs_yP_{1-y}$ is

$$a(x, y) = 0.1896y - 0.4175x + 0.0124xy + 5.8687 \qquad \text{Eq. (2.3)}$$

Rewriting Eq. (2.3) for InGaAsP lattice-matched to InP, the mole fractions, x and y, can be approximated by

$$x \approx 0.47y \qquad \text{Eq. (2.4)}$$

The bandgap equations for ternaries and quaternaries are derived from semiconductor band theory and experimental measurement techniques, such as photoluminescence, ellipsometry, etc. The experimentally obtained InGaAsP direct energy gap equation [11] is

$$E_g(x, y) = 1.35 + 0.668x - 1.068y + 0.758x^2 + 0.078y^2 - 0.069xy - 0.322x^2y + 0.03xy^2 \qquad \text{Eq. (2.5)}$$

2.2 Gas Source Molecular Beam Epitaxy

Molecular Beam Epitaxy (MBE) is a semiconductor material deposition technique developed in the late 1960s that is performed in an UtraHigh Vacuum (UHV) environment. The source material is supplied in a pure, solid elemental form and a heated semiconductor substrate acts as the template for deposition of crystalline material. The deposited semiconductor material crystallizes as the incident atoms migrate along the surface of the sample, and find a lowest energy location (i.e. preferred incorporation site) at which the atomic bonds are satisfied. The elemental source material is located in heated ovens that generate atomic or molecular beams of material via vaporization; the beams are controlled (blocked or not blocked from the

path to the substrate) via metallic shutters. In an UHV environment (i.e. 10^{-8} to 10^{-10} Torr) the generated atomic or molecular beams have a line-of-sight path to the semiconductor substrate. The molar composition of the elements within the deposited crystal is a function of the ratio of the elements incident on the semiconductor substrate. Doping of the semiconductor is a function of the relative arrival rate of the elements and dopant atoms at the sample surface. Typical growth rates for semiconductor materials via MBE are ~1 μm/hr.

The use of Gas Source Molecular Beam Epitaxy (GSMBE) for semiconductor materials growth has been in existence since the late 1970s [16]. The technique, based on MBE, is a marriage of solid sources and gaseous sources. By the mid- to late 1970s, MBE produced the most abrupt interfaces, the most accurate compositional changes, and the most controlled doping profiles. Initial attempts to deposit InGaAsP on InP via MBE were relatively unsuccessful due to the lack of a high quality source for generation of a stable P_2 flux. The early methods of using solid phosphorus involved vaporizing red phosphorus, P_4, directly. This method has multiple inherent difficulties, including: (1) P_4 is composed of various allotropic forms in which each form has a different vapor pressure, (2) P_4 has an extremely short lifetime on the sample surface and without an excessive flux during growth, In-rich material will be deposited, and (3) due to the excessive amounts of P_4 needed, a build-up of elemental (white) phosphorus, P, occurs in the growth chamber deteriorating the UHV environment necessary for MBE growth. The other common growth methods at the time, i.e. Liquid Phase Epitaxy (LPE) and Metal Organic Chemical Vapor Deposition (MOCVD), were likewise plagued by a set of inherent problems, such as interface grading and lack of control over the doping profile [16]. Thus, the need for a growth method that would combine the qualities of MBE and a constant phosphorus flux (without a by-product of white phosphorus) prompted the development of GSMBE [16].

GSMBE is essentially conventional MBE with group V elements supplied in the form of hydrides. Under typical MBE growth conditions, the rate of material deposition is essentially controlled via the supply rate of the group III element(s), whether the group V elements are supplied in solid or gaseous form. Thus, GSMBE takes advantage of the precise control of layer thickness (and associated deposition rate) achievable with the MBE technique. Although the low pressure and atmospheric pressure growth methods, such as MOCVD, tend to be preferred in manufacturing settings (e.g. due to less down time for routine maintenance, and less material build-up on the walls of the reactor) the UHV environment of MBE produces purer material with well-defined surfaces and interfaces [17]. Additionally, within the MBE growth environment, deposition of individual monolayers can be achieved (e.g. Migration-Enhanced Epitaxy (MEE) [18] or Atomic Layer Epitaxy (ALE) [31]).

The atomic beams of group III elements (i.e. In, Ga, Al) are generated in both MBE and GSMBE by heating of an effusion cell. An effusion cell is an oven comprised of a ceramic Pyrolytic Boron Nitride (PBN) crucible surrounded by a heating coil, in which the solid elemental material is placed within the crucible. The effusion cells are heated to temperatures ranging between 750°C and 1200°C (material dependant), at which point a molecular beam (or flux of material) is generated via vaporization [16]. The vaporized material in the effusion cells is blocked from the semiconductor substrate surface by a molybdenum or tantalum shutter. For growth, the shutter is opened for an interval of time corresponding to the desired thickness of the material being deposited, with a simultaneous provision of a group V flux.

A disadvantage of the effusion cell is the nonuniform flux generated as a result of the system geometry and the cosinusoidal distribution of molecules leaving the cell. However, this nonuniformity is rather adequately negated by rotating the semiconductor substrate, resulting in a more uniform distribution of atoms across the entire semiconductor surface. Additionally, the development of crucibles with narrower openings (i.e. the Sumo Cell manufactured by EPI [19]) and conical-shaped crucibles further enhance the flux uniformity.

The group V elements in GSMBE are generated from the hydrides phosphine, PH_3, and arsine, AsH_3. An advantage of using gaseous group V elements is the near instantaneous flux changes achievable as compared to the solid source alternative. The decomposition of the hydrides from MH_3 to M_2 and H_2 is accomplished by passing the pure (99.999%) hydride through a high-temperature-low-pressure gas cell. This gas cell is also known as a "cracker" since it thermally decomposes (or cracks) the hydrides at temperatures between 900°C and 1100°C. The internal arrangement of the cracking cell is such that the hydride is passed through a pyrolytic boron nitride (PBN) tube followed by a high temperature zone containing high purity PBN chips. The thermal cracking takes place in the high temperature zone when the hydride is in contact with the PBN chips [20]. The use of a mass flow controller (MFC) further enhances the attractiveness of gaseous group V sources as the MFCs accurately control the rate at which the hydrides enter the cracker. Since the cracking efficiency of AsH_3 and PH_3 is nearly 100% for cracker temperatures between 900-1100°C [20], the flux impinging on the semiconductor surface is likewise well controlled. In addition to precise flux control, MFCs offer more accurate and timely changes in hydride flow rates.

The MBE environment is typically cleaner than other growth environments, in many regards due to the ultralow pressure environment. In either atmospheric or low pressure (~ 76 Torr) MOCVD, the gases are introduced into the susceptor as hydrides and organometallics, and the cracking of the hydrogen and carbon molecules is performed in a 'boundary layer' [21]. The boundary layer is located at the surface of the semiconductor sample. If the temperature of the sample is such that the carbon and hydrogen molecules are separated from the group III atoms, the elements will then be able to incorporate into the

semiconductor crystal structure. Although GSMBE also utilizes hydrides for the group V sources, the hydrogen is separated from the group V atoms upon entry into the UHV environment, generating H_2 and group V dimers. The H_2 by-product is not harmful to semiconductor growth, and most likely does not affect the growing crystal because of the excessive temperatures required to break a H-H bond. For example, the cracking efficiency for H_2 passed through a PBN tube containing a tungsten filament held at ~2100°C is only ~3% [22]. Although the H_2 generated via cracking of the hydrides does not directly affect the growing crystal, the overpressure due to the H_2 in the GSMBE reactor may limit the maximum achievable group V flux (pumping system dependent).

An additional advantage of GSMBE being an extension of conventional MBE is that the well developed *in-situ* surface analysis technique, Reflection High Energy Electron Diffraction (RHEED), may be utilized. The electrons diffracted from the surface of the semiconductor substrate are directed to a phosphorus-coated screen for observation. These electrons typically have energies between 5 and 50 KeV. (GS)MBE is particularly suited for RHEED not only because of the effective line-of-sight in a UHV environment, but also because the internal arrangement of MBE-type machines are such that the electrons are incident on the semiconductor sample at a slight angle (1-3 degrees), and do not interfere with the placement of the molecular sources. A small incidence angle is desired in order to limit the depth in which the electron penetrates the semiconductor material. By limiting the penetration depth, the electron beam is sensitive to changes on the surface of the semiconductor. Thus, the surface can be monitored during deposition, and the status of the growth can be determined by monitoring the resulting RHEED pattern. In order to diffract from the semiconductor surface, the wavelength of the electron must be on the order of, or smaller than, the lattice constant; for high energy electrons (5-50 KeV) the deBroglie wavelength range is 0.17-0.06 Å.

A RHEED pattern is generated by the interference of the diffracted electrons. Analogous to multiple slit optical diffraction, diffraction from a crystal lattice produces the Fourier Transform of the periodic lattice. Thus, each lattice arrangement will have a characteristic RHEED pattern. Since RHEED is sensitive to the surface of the semiconductor, the diffracted pattern will be altered if there is any type of surface structure, e.g. steps or islands. Typically, a rough surface, or a randomly oriented three-dimensional surface, results in a spotty "bulk" RHEED pattern, as shown in Figure 2.2(a), since the diffracted electrons penetrate the sample and diffract from the 3-D features on the surface. A bulk RHEED pattern is typical of a semiconductor substrate prior to material deposition. An epitaxial layer of thickness that has surpassed the critical thickness (the thickness to which the deposited layer can maintain any lattice-mismatch-induced strain before relaxation begins) is also inherently rough due to strain relaxation mechanisms. However, the roughness is typically somewhat periodic. The resulting RHEED pattern from an epilayer

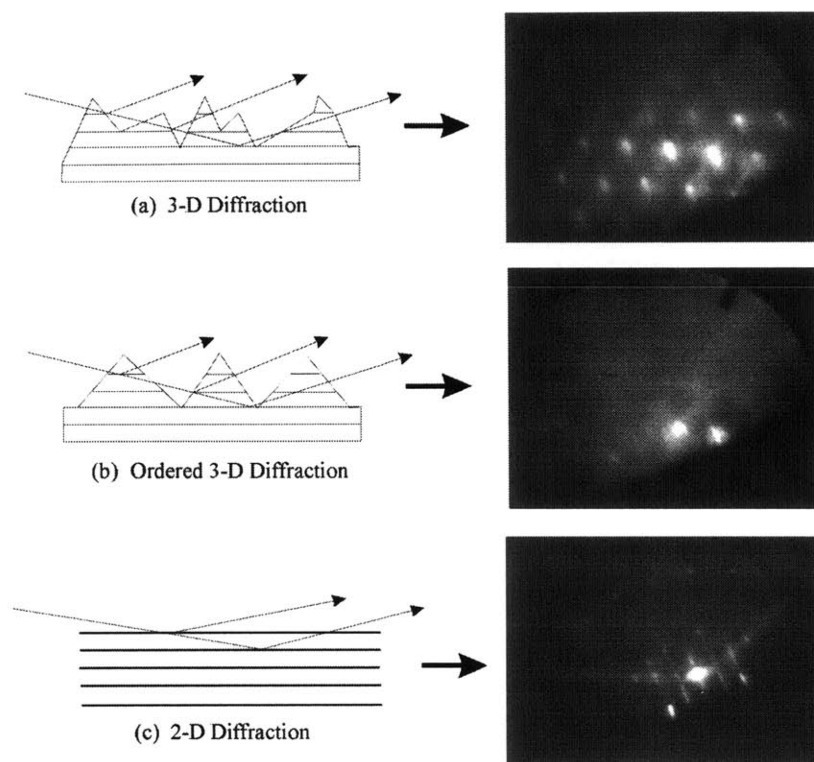

Figure 2.2 (a) 3-D, or bulk, electron diffraction from a rough InP surface. (b) Electron diffraction from an ordered, yet rough, surface. (c) 2-D, or surface, electron diffraction from a smooth InP surface along $[0\bar{1}\bar{1}]$.

that has recently surpassed the critical thickness is shown in Figure 2.2(b). A smooth surface, or a two-dimensional surface, results in a streaky surface RHEED pattern, as shown in Figure 2.2(c) since the electrons are coherently diffracted from the surface layers. Additionally, the surface RHEED pattern of a zincblende III-V (100)-oriented semiconductor surface usually differs between $[0\bar{1}\bar{1}]$ and $[0\bar{1}1]$, and is dependent on the arrangement of the bonds between surface atoms, e.g. the surface reconstruction. The RHEED pattern will further differ depending on the type of atoms present on the semiconductor surface (i.e. group III or V). Typical atomic configurations for a P-stabilized InP surface, at 480°C, are a four-fold periodicity along $[0\bar{1}1]$ and a two-fold periodicity along $[0\bar{1}\bar{1}]$. For an electron beam incident along $[0\bar{1}1]$, the resulting RHEED pattern will represent the four-fold periodicity and appear similar to see Figure 2.3. Likewise, an electron beam incident along $[0\bar{1}\bar{1}]$ will be sensitive to the two-fold periodicity [see Figure 2.2(c)].

RHEED patterns are observed not only to monitor the quality of each layer, but also to observe surface transitions such as oxide desorption. As a native surface oxide is inherently amorphous, exposure of the crystalline substrate following oxide desorption is easily observed via RHEED. RHEED patterns are also

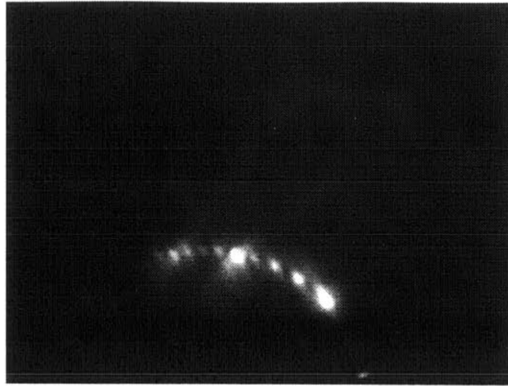

Figure 2.3 4-fold RHEED pattern from an InP surface along $[0\bar{1}1]$.

monitored in order to non-destructively determine the growth rate of deposited materials. Oscillations in time of the diffracted intensity during epitaxy correspond to the deposition of monolayers of material. The intensity is related to the changes in step edge density and the ordering of the atoms on the surface. The portions of higher intensity correspond to a smoother surface (i.e. a completed monolayer), whereas those of lower intensity represent a rough surface (i.e. partial monolayer completion). The combination of one period of high and low intensity is representative of the deposition of a single monolayer of material. RHEED oscillations are only observable within the first few minutes of layer deposition until the surface roughness reaches a steady state condition. Hence, RHEED oscillations are only apparent when there is a distinct change in the surface roughness, as in the case for growth on atomically smooth surfaces (as opposed to growth on rough 3-D surfaces).

Additional *in-situ* monitoring techniques that have been applied to MBE include reflectometry (for layer thickness determination), pyrometry (for sample temperature determination), and ellipsometry (for layer thickness and composition determination). Development of *in-situ* control of epilayer composition and thickness using an 88-wavelength ellipsometer is currently under development on the GSMBE system at MIT. Development of this technique is being performed by Dr. G.S. Petrich and S. Warnick in Prof. Leslie A. Kolodziejski's laboratory.

In the last few years, the use of GSMBE has been slowly declining. With the development of high quality solid phosphorus crackers [23,24,25], a number of GSMBE machines have been converted to solid source MBE because of safety considerations.

The GSMBE system used for deposition of all structures presented in this thesis is a Instruments SA Riber 32P machine. It is part of an integrated II-VI/III-V epitaxy system, as shown in Figure 2.4. All systems, both II-VI and III-V reactors, an Auger electron spectroscopy (AES) system, a sample bake-out

chamber, and an introduction chamber are connected *in-situ* by a transfer chamber; the base pressure of all systems is 5×10^{-9} Torr or lower. The solid group III sources available are Al, Ga, and two In sources. The group V materials are supplied via arsine and phosphine, and the dopant sources are solid Si and Be. The majority of the effusion cells are Riber single filament, straight-walled effusion cells with 35cc crucibles (one of the two In effusion cells is a Riber dual filament, straight-walled cell). Ceramic inserts, with an eight degree taper, have been added at the lip of each crucible in order to increase surface uniformity of the deposited material. The pumping systems on the Riber GSMBE system are a Pfieffer 2200 *l*/s turbomolecular pump (with an Edwards mechanical backing pump) and a CTI cryopump (as a back-up). The turbo pump is used in most cases, and always during growth, due to the higher chamber pressures ($\sim 10^{-5}$ Torr) that result from cracking the hydrides. This system also contains an EPI hydrogen cracking cell, for generation of atomic hydrogen for low temperature oxide removal techniques.

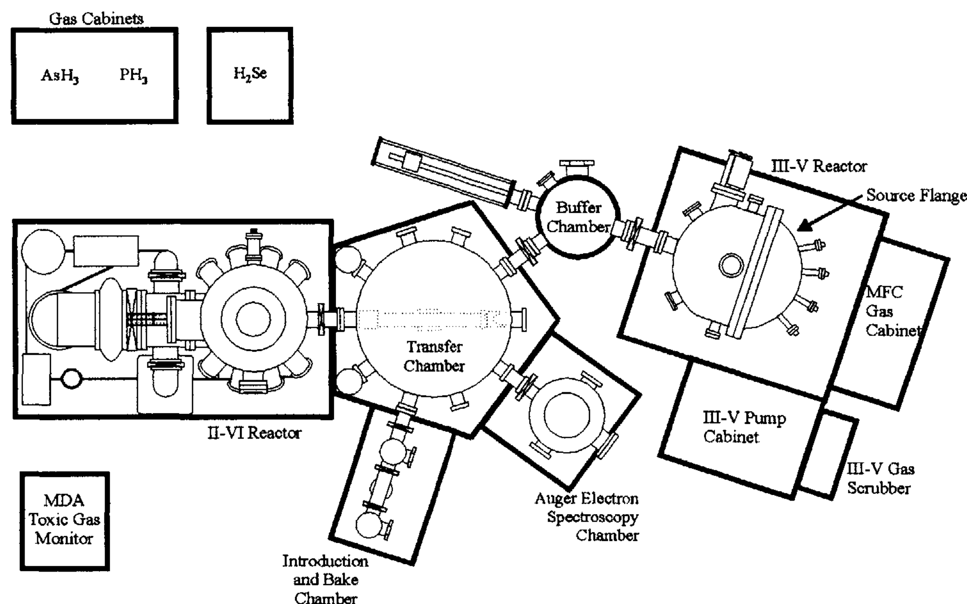

Figure 2.4 Diagram of the integrated II-VI/III-V system. All samples are introduced into the system via the Introduction Chamber.

Although the quality and rate of the GSMBE material deposition can be monitored *in-situ* via RHEED, extensive analysis of the materials and heterostructures must be accomplished *ex-situ*. External analysis techniques include photoluminescence (both low temperature (10K) and room temperature) for determination of material bandgap, and high resolution x-ray diffractometry for determination of the material lattice constants. In the case of InGaAsP material characterization, both photoluminescence and

x-ray diffraction measurements are analyzed in order to uniquely determine the mole fraction of all four elements.

2.2.2 Post-Growth Material Characterization: A Brief Overview

Post-growth characterization techniques are used to determine more precisely the compositions of the grown quaternary, and to complete a rather accurate feedback loop. The techniques utilized for layer growth include Auger electron spectroscopy (AES), high resolution double axis x-ray diffractometry (HRDAXD), and photoluminescence (PL). In order to accurately determine a composition, it is necessary to use a combination of HRDAXD and a luminescence technique. As will be described in more detail in the following sections, HRDAXD will illuminate strain in the crystal structure, whereas a luminescence method will reveal the bandgap of the material.

Auger Electron Spectroscopy

Auger electron spectroscopy (AES) is a technique for analyzing surfaces based on the Auger process. A surface atom, ionized via an impinging electron, may decay to a lower energy state (a doubly ionized state) via an electronic rearrangement. The energy difference between the steady state of the atom and the lower energy state of the doubly ionized atom is transferred to the ejected Auger electron, which will contain a kinetic energy characteristic of the atom from which it was ejected. If this process occurs within a few angstroms from the surface, the ejected Auger electron can be expelled without a loss of energy. This Auger electron then generates peaks in the secondary electron energy distribution function, from which the composition of the surface can be rather accurately identified [48].

An AES system is an UHV system consisting of an electron gun and an energy analyzer. The Auger peaks are more accurately identified by differentiating the secondary electron energy distribution, therefore the typical Auger spectrum is the function $\frac{dN(E)}{dE}$. The peak-to-peak amplitude of an Auger peak is related to the atomic concentration. When not using a calibration piece (e.g. silver), the surface concentration of some element x, C_x, can be approximated by

$$C_x = \frac{I_x}{d_x S_x}\left(\sum_{\alpha} \frac{I_\alpha}{d_\alpha S_\alpha}\right)^{-1} \qquad \text{Eq. (2.6)}$$

where I is the peak-to-peak amplitude of the element on the Auger scan, S is the relative sensitivity of element x as compared to silver, and d is the scale factor; the sum is over all elements detected. d_x is defined as

$$d_x = L_x E_{m,x} I_{p,x} \qquad \text{Eq. (2.7)}$$

where L_x is the lock-in amplifier sensitivity, $E_{m,x}$ is the modulation energy, and $I_{p,x}$ is the primary beam current [48].

High Resolution Double Axis X-ray Diffraction

HRDAXD is a non-destructive method of providing structural information about deposited layers. It can be used to determine the lattice constant of a single quaternary layer or the periodicity of a complex structure, such as a superlattice. By comparing the results of a scan with dynamical diffraction simulations it is possible to rather accurately determine the material composition. Details of the HRDAXD technique will not be presented in detail here, but can be found in Appendix A. This section will describe only the information obtained from the post-growth analysis technique.

For the growth of pseudomorphic layers, the value of the lattice constant perpendicular to the growth plane, a_z, is typically sufficient information for determining material mismatch and uniform strain. An HRDAXD scan using the (400) diffraction condition yields the value of a_z. Mathematically, a_z can be expressed as

$$a_z = \frac{a_{sub} \sin\theta_B}{\sin(\theta_B + \Delta\theta)} \qquad \text{Eq. (2.8)}$$

where a_{sub} is the lattice constant of the substrate, θ_B is the Bragg angle of the substrate, and $\Delta\theta$ is the diffracted angular difference between the epilayer and the substrate peaks. When a second material is deposited on top of the substrate, it can either be lattice-matched, or lattice-mismatched in one of two ways, namely compressive-strained or tensile-strained. A compressive-strained material has a lattice constant larger than the substrate lattice constant. Thus, when deposited on the substrate, the in-plane lattice constant of the epilayer will match that of the substrate, and the perpendicular lattice constant of the epilayer will increase in order to compensate for the smaller in-plane lattice constant. An increase in a_z corresponds to $\Delta\theta$ less than zero. Therefore, a compressive-strained material will appear on a (400) HRDAXD scan as a peak to the left of the substrate peak. Similarly, a tensile-strained material, whose lattice constant is smaller than that of the substrate, will have a_z smaller than a_{sub}. Thus, it will appear on a (400) HRDAXD scan as a peak to the right of the substrate peak.

In order to determine the strain in a material from an HRDAXD scan, x and y (the group III and group V compositions) must be deciphered. To do this, an HRDAXD simulation program is used to obtain a fit to the actual data. A good starting point for simulating the grown layer is the In and Ga compositions calculated from RHEED oscillations.

In addition to determining the composition of a material, HRDAXD also reveals the crystalline quality of the material. The smaller full-width-at-half-maximum (FWHM) of the x-ray feature, the higher the crystal quality. A high-quality MBE- or GSMBE-grown material will ideally have a FWHM equal to the resolution of the HRDAXD measurement system (i.e. the theoretical FWHM for InP is on the order of 1 arcsec [49]).

In order to more accurately determine the composition of a material, HRDAXD must be evaluated in conjunction with a bandgap analysis technique, such as photoluminescence, which is discussed in the following section.

Photoluminescence

When performing HRDAXD simulations of $In_{1-x}Ga_xAs_yP_{1-y}$, there can be multiple combinations of x and y that have identical perpendicular lattice constants. Therefore, the use of a bandgap analysis technique, such as photoluminescence (PL), is helpful in more accurately determining the material composition. Having obtained the bandgap from PL, only one of the various HRDAXD simulated compositions will satisfy Eq. (2.5).

PL is a process that involves the generation of electron and hole pairs in a sample by a laser whose energy is larger than the bandgap of the sample [50]. (See Figure 2.5 for a diagram of the setup used for data present in this thesis.) The incident photons will be absorbed by the material, creating electron-hole pairs; the carriers will recombine via spontaneous emission, revealing the characteristic bandgap of the sample. PL is typically performed at either room temperature or low temperature (between 4-77K, depending on the technique). Room temperature measurements are attractive for determining the bandgap of the material being analyzed. It is difficult, however, to accurately determine the material quality from a room temperature measurement since contributions from effects such as thermal broadening and alloy broadening [51] are significant. Low temperature PL provides a much more accurate estimate of the material quality since the above mentioned effects are minimized; the narrower the FWHM of the luminescence feature, the better the optical quality of the material. Also of significance in analyzing the PL spectrum is the resulting intensity of the signal(s). High intensity signals suggest high quality material, whereas low intensity signals suggest the existence of non-radiative recombination centers (typically in the form of defects).

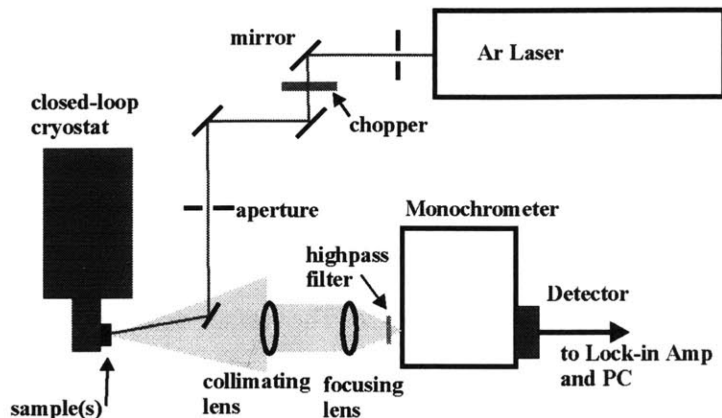

Figure 2.5 Diagram of the photoluminescence setup used for measurements presented in this thesis. The highpass filter passes wavelengths greater than 550 nm.

2.2.3 InP Materials Growth

Prior to introduction of a sample into the GSMBE reactor, the sample is outgassed, or baked, at 210°C for an hour in order to remove any water and other weakly bonded materials that may inhibit high quality epitaxial growth. The reactor must also be prepared for material deposition; the cryoshroud (or inner lining of the reactor) must be cooled to the temperature of liquid nitrogen (LN_2), 77K, so as to condense any impinging atoms or molecules in the chamber that are not immediately removed via the pumping systems. The temperature of the cryoshroud is maintained throughout the growth in order to minimize background contaminants in the growth environment, as well as thermally isolate the effusion cells. As the effusion cells are heated to temperatures ranging from 750-1200°C for material deposition, LN_2 flowing through the source flange also helps maintain a reasonable temperature distribution over the entire flange (see Figure 2.4 for location of the source flange). Furthermore, the cold source flange condenses atoms exiting the effusion cells, (those that skirt around a closed shutter), and minimizes cross contamination between the effusion cells.

For the elements required for material deposition, the respective effusion cells must be set to a temperature that corresponds to the required growth rate. The effusion cells are first outgassed (heated to temperatures above those typically used for growth) so as to remove the outermost layer of material on the charge (the material within the crucible). Since it is possible for stray atoms or molecules to contaminate

the solid sources, removal of the outermost layer minimizes the possible contamination. The flux emitted from the effusion cells is then monitored for each source for stability and repeatability.

Following introduction of the InP sample into the GSMBE reactor, the substrate temperature is ramped to the growth temperature in order to desorb the native amorphous oxide. An overpressure of phosphorus must be amply supplied, as the desorption temperature of phosphorus in an UHV environment is approximately 356°C. Desorption of phosphorus from an InP surface in the absence of replacement phosphorus results in the formation of bonds between In atoms, creating coalesced islands of In; subsequently, the surface of the InP wafer is destroyed. The surface oxide is typically completely desorbed from an InP wafer at a substrate temperature of approximately 450°C (calibrated via an optical pyrometer); this transition is displayed by a change in the RHEED pattern. The InP RHEED pattern along $[0\bar{1}\bar{1}]$ and $[0\bar{1}1]$, as the oxide begins to desorb and thin, transforms from indiscernible to a 2-fold by 3-fold reconstruction, respectively. Following oxide desorption, the InP crystal structure is fully exposed (as is evidenced by a (2x4) RHEED pattern) and provides a template for material deposition.

Since the surface of an epi-ready wafer, once the oxide is desorbed, is inherently rough (compared to that of an atomically-smooth epitaxial layer) as the result of surface preparation, the first epitaxial step is to deposit a buffer layer of the same composition as the substrate. This layer buries the rough wafer surface, and generates a smoother surface that results in both increased diffracted intensity of the RHEED beam and a more ideal surface for epitaxy. Following the deposition of the buffer layer, which is typically 100 nm or more, the desired structure is deposited.

Typical substrate temperatures for MBE of InP are near 480°C, and are extremely close to temperatures at which the evaporation of In becomes significant (> 500°C) [16]. For substrate temperatures greater than 500°C, the rate of arrival of In at the semiconductor surface must be higher than the rate of In evaporation. In general, for GSMBE growth of III-V semiconductors, the minimum V/III ratio required for stochiometric growth is unity. For a V/III ratio less than 1, the probability of In atoms bonding to one another due to the lack of available phosphorus atoms will be high; the result will be coalesced islands of group III atoms, and a defective surface and crystal structure. For a V/III = 1, ideally one group V atom is available for each group III atom. However, the probability of an In atom migrating along the surface (as a result of P desorption) and bonding to another In atom is great. This is evidenced by the observation of large defect densities in InP layers deposited with V/III ~ 1.

The substrate temperature range for deposition of InP is relatively narrow compared to that of GaAs. On the lower end of stochiometric InP, which is commonly ~400°C, the In atoms have a shorter migration length leading to the formation of a rough surface. On the upper end (greater than ~500°C), the growth rate of InP is controlled by the number of In atoms that incorporate into the growing layer (i.e. those that are

not evaporated from the surface); in this regime, the sticking coefficient of In is less than one, e.g. not every atom that impinges on the surface will incorporate into the layer. The ideal growth temperature range for InP is between ~450°C and ~530°C, where the sticking coefficient of In is essentially equal to unity [11]. The majority of InP and related materials grown for this thesis were grown at a substrate temperature of ~470-480°C, as measured by a thermocouple.

Defect generation resulting from the oxide desorption procedure and InP buffer layer nucleation conditions have been investigated for the typical InP growth conditions used at MIT. The previously determined growth conditions for InP materials encompass a substrate temperature of 480°C (as measured by a thermocouple located behind the sample) and a V/III ratio of approximately 6; although the designated growth conditions produce reasonable quality material, a large number of defects were still present within the deposited structures [26,27]. The generated defects are approximately rectangular in shape [see Figure 2.6(a)] and are categorized as a type of oval defect. The long axis of these oval defects is

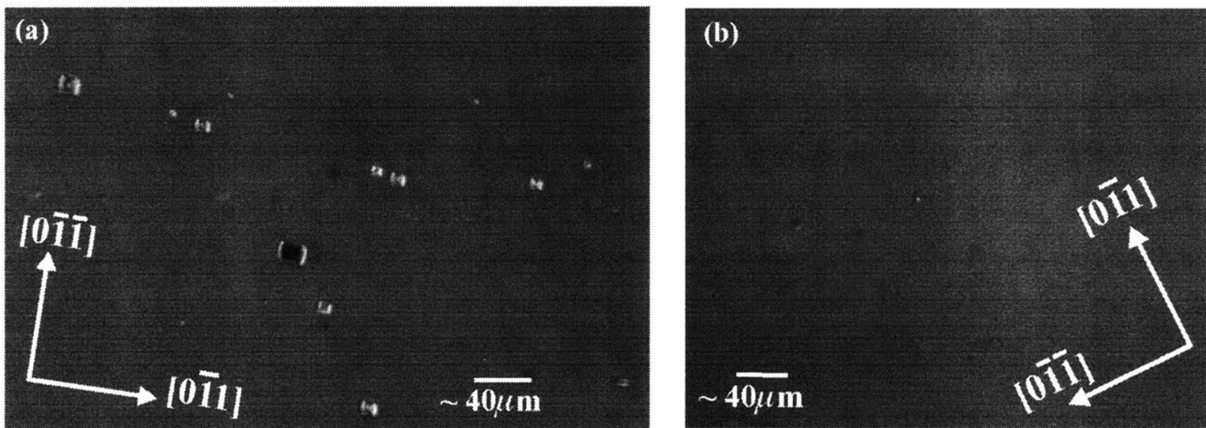

Figure 2.6 (a) Nomarski microscopy image (200x magnification) of ~2 μm InP (lightly Si-doped) deposited on an InP substrate. Growth conditions: rate ~ 0.7 μm/hr, Tsub ~ 480°C, chamber pressure ~ $3x10^{-5}$ Torr, and V/III ~ 10. (b) Nomarski microscopy image (200x magnification) of ~0.17 μm InP and ~0.07 μm InGaAs deposited on an InP substrate. Growth conditions for InP: rate ~0.35 μm/hr, Tsub ~470°C, chamber pressure ~$1.9x10^{-5}$ Torr, V/III ~ 13. The ramped nucleation procedure was utilized in (b) only. Any visible vertical and horizontal striations are caused by the printer.

typically aligned along [0$\bar{1}$1] for (100) InP substrates, and tend to increase in size as well as density with layer thickness. Cotta, *et al* have observed these same defects in metalorganic MBE (MOMBE), and they attribute the large defects to surface contamination and the small defects to growth conditions [28]. From the layers and structures deposited for this thesis, the oval defect density was observed to be somewhat dependent on the oxide desorption procedure, the growth conditions (specifically the growth rate used during nucleation of the buffer layer), and the epitaxial layer thickness. The most promising results thus far

have been obtained using a ramping oxide desorption procedure, a slow growth rate (~0.35 μm/hr) for the buffer layer, and a V/III ratio of ~13.

The ramping oxide desorption process involves increasing the substrate temperature from 100°C to 480°C in 38 minutes, decreasing the temperature to 470°C in one minute, and immediately nucleating the InP buffer layer upon completion of the one minute temperature drop; all steps are performed in succession and without delays. The actual substrate temperature at nucleation is about 474°C (thermocouple-determined). The InP growth rate is ~0.35 μm/hr and the overpressure is ~1.8×10^{-5} Torr, resulting in a V/III ratio of ~13. For slower growth rates, the resident time of an In atom on the sample surface is larger, leading to a longer diffusion length for a given P flux. The disadvantage of a rapid growth rate, for the same P flux, is the increased probability of the generation of coalesced In islands, and thus the generation of crystallographic defects. Although the InP growth rate used is quite low (~0.35 μm/hr), the large V/III ratio will slightly negate the diffusion length increase achieved via a low growth rate. However, the excess supply of phosphorus will help minimize the formation of In islands. For calibration layers comprised of ~170 nm InP buffer layers and ~70 nm InGaAs layers, defect densities as low as ~1.2×10^{3} cm^{-2} have been observed [see Figure 2.6(b)]. For thick InP layers, ~2 μm, the defect density is typically significantly higher (on the order of 10^{-4} cm^{-2}), however the buffer layer is also nucleated at a much more rapid growth rate (~0.7-1.0 μm/hr). At the higher growth rate, the defect sizes vary, suggesting continued creation of defects and growth-induced enlargement of the defects. As seen in Figure 2.6(a), for a ~2 μm InP layer (lightly Si doped), the oval defect size ranges from ~12 x 20 μm^2 down to ~3.5 x 5 μm^2. Previous work by J.M. Milikow suggests that low temperature (~240°C) cleaning of the InP substrate using atomic hydrogen reduces the density of oval defects, but does not obviate the defects [26]. As the InP surface seems to be quite sensitive to exposure to elevated temperatures in the absence of material deposition, it is highly probable that a number of the oval defects are generated during both the oxide desorption process as well as growth interruptions. Cotta, *et al* have found via transmission electron microscopy (TEM) that the oval defects are generated as the result of In-rich clusters [28]. At temperatures typically used for the growth of InP, since In is highly mobile (i.e. measured surface diffusion lengths of ~25 μm at 520°C [29]) and phosphorus easily desorbs from the surface, the probability of two or more In atoms bonding to one another along the wafer surface is not unlikely; a similar scenario exists for growth interruptions at InP-containing layers or interfaces. All of these observations suggest a delicate balance between the exposure of the surface to elevated temperatures in the absence of material deposition, the desired P-overpressure to minimize In-clustering, and the growth rate required to allow In atoms to migrate to the 'best possible' incorporation location.

The presence of oval defects has also been observed in InP-containing materials deposited on GaAs substrates. Figure 2.7 depicts a Nomarksi microscopy image of ~0.25 μm of InP (containing 2 InGaAs quantum wells) deposited on a GaAs substrate, following deposition of a ~0.5 μm thick GaAs buffer layer. On GaAs substrates, the long side of the oval defect is aligned along $[01\bar{1}]$, which similar to deposition on InP substrates, corresponds to the crystallographic direction with the longer diffusion length [30]; recall that the defect alignment on InP substrates is such that the long side of the defect is also along the crystallographic direction having the longer diffusion length.

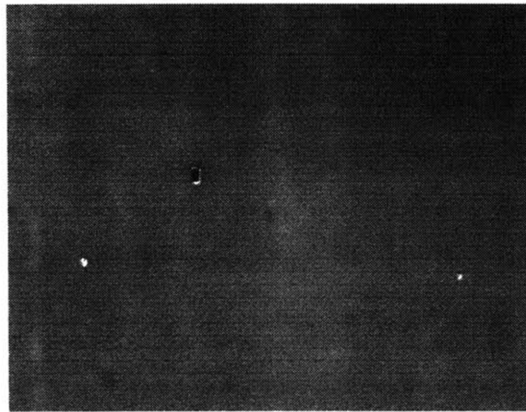

Figure 2.7 Nomarski microscopy image (200x magnification) of ~0.25 μm of InP (and 2 InGaAs quantum wells) deposited on a GaAs substrate. Growth conditions for InP: rate ~0.35 μm/hr, Tsub ~470°C, chamber pressure ~1.9×10^{-5} Torr, V/III ~ 13. Note: the surface is slightly rough, but not unexpected due to the large lattice-mismatch. Any visible vertical and horizontal striations are caused by the printer.

2.2.4 GaAs Materials Growth

MBE-based deposition of GaAs is a well developed technique. For the work reported in this thesis, the growth of GaAs-based materials was not investigated, but rather was utilized. Like all semiconductor growth, the amorphous native oxide must first be removed in order to expose the underlying crystallographic structure of the substrate. Thermal oxide desorption for GaAs takes place at ~580°C. Subsequent growth of GaAs materials is typically performed at roughly 600°C, with exceptions being Al-containing materials (typically deposited at substrate temperatures greater than 600°C due to Al's short diffusion length at 600°C) and In- and P-containing materials (see Section 2.2.3 for substrate temperature restrictions). As MBE growth of GaAs-based materials has been in existence since the late 1960s, both growth parameters and material development (i.e. substrate manufacturing) have been studied in much detail [31]; partly for this reason, the number of growth-generated defects in GaAs-based structures is less

than that seen in InP-based structures. Figure 2.8 depicts a Nomarski microscopy image of a typical $Al_{(1-x)}Ga_xAs$ /GaAs ($x \sim 0.85$) surface.

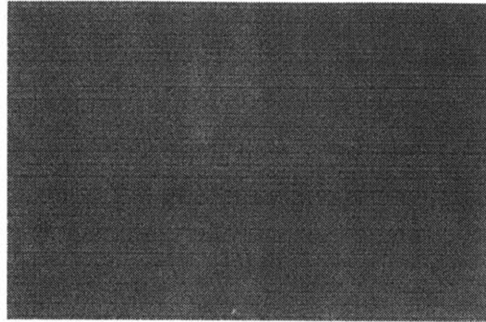

Figure 2.8 Nomarski microscopy image (200x magnification) a typical AlGaAs/ GaAs surface grown by GSMBE. 500 nm of $Al_{(1-x)}Ga_xAs$ ($x \sim 0.85$) deposited on GaAs. Any visible vertical and horizontal striations are caused by the printer.

Similar to growth of InP, GaAs layers of high quality are achieved with the group V species (As) provided in excess, e.g. V/III > 1. The typical growth procedures followed at MIT for deposition of GaAs are: temperature ramp of the substrate from 100°C to 640°C (temperatures as determined via a thermocouple) in 54 minutes followed by a pause (on the order of a few minutes) for observation of the RHEED pattern and confirmation of oxide desorption. The typical RHEED pattern following thermal oxide desorption is a bulk pattern or a slightly streaky (2x1) pattern, in which the 2-fold pattern is along [011]. The buffer layer is then nucleated, and the RHEED pattern transforms to (2x4) within 30 seconds to 1 minute, depending on the chosen growth rate.

Following deposition of the buffer layer, the substrate is ramped to the appropriate temperature for the next layer to be deposited. Al-containing layers are typically deposited with a substrate temperature of 640°C or higher. In- and P-containing materials are typically deposited at a substrate temperature of 480°C. Typical V/III ratios used are ~3 or higher.

2.2.5 InGaAsP Materials Growth

(In,Ga)(As,P) is an extremely flexible material system. It can be lattice-matched to both InP and GaAs over a wide range of bandgaps. Figure 2.1 depicts the (In,Ga)(As,P) system in terms of lattice constant and bandgap. InGaAsP is the most flexible system lattice-matched to InP, with bandgaps between 0.74eV ($In_{0.53}Ga_{0.47}As$) to 1.35eV (InP), and is the primary material component of 1.1 μm, 1.3 μm, and 1.55 μm optical devices. As the communication market continues to expand, the need for deposition of high quality InGaAsP materials is required.

The GSMBE growth of (In,Ga)(As,P) materials on InP utilizes approximately the same parameter space as GSMBE growth of InP. All materials from the (In,Ga)(As,P) compound semiconductor family are grown at a substrate temperature of approximately 480°C. The GSMBE system used for this thesis was equipped with two In effusion cells and one Ga effusion cell. Therefore, material deposition was designed around a common Ga cell temperature for ease of integration; this proved to be problematic in instances in which adjacent layers were of drastically different compositions, i.e. between cladding layers and active layers, and required either a compromise in growth rates or a growth interruption at an interface. Even slight compositional changes between layers can take five or more minutes due to changes in cell temperatures and the accompanying stabilization time. Excessive time interruption between layers in structures such as superlattices and multiple quantum wells can result in severe compositional grading. During the time taken to change cell temperatures, As-P exchange is likely to take place, resulting in a compositional change on the surface of the last grown layer [i.e. 16,33,34].

The RHEED patterns of InP-based materials are similar to those of InP. For lattice-matched InGaAsP, a high quality layer will exhibit a (2x4) RHEED pattern. In addition, RHEED oscillations are quite easy to obtain from InGaAsP layers due to the overall decrease in the mobility of the group III atoms resulting from the addition of As. From RHEED oscillations, an approximate value for the growth rate of the material can be obtained. Based on the bandgap and lattice-matching requirements, specific compositions of $In_xGa_{1-x}As_yP_{1-y}$ can be chosen. Given x and y, it is possible to determine the growth conditions, namely the effusion cell temperatures and hydride flow rates, necessary to obtain the desired quaternary. This is done by considering binary growth rates. The total growth rate of InGaAsP during GSMBE is the sum of the growth rates of InP and GaAs (on InP), which can be readily obtained from growths of InP on an InP substrate and GaAs on a GaAs substrate. However, since the GaAs growth rate is observed on a GaAs substrate, the growth rate must be scaled to an InP lattice, which is larger than a GaAs lattice. To scale the GaAs growth rate, it is multiplied by the square of the ratio of the InP lattice constant to the GaAs lattice constant, resulting in a conversion factor of approximately 1.07. Since the total growth rate of the quaternary is a sum of the growth rates of the group III elements, the fraction of In (Ga) in the quaternary can be determined from the ratio of the InP (GaAs * 1.07) growth rate over the total InGaAsP growth rate.

Ternary materials are much easier to deposit than their quaternary counterparts simply due to the presence of one less variable. If the ternary is of the form $III_xIII_{1-x}V$, the materials growth is fairly simple. RHEED oscillations are sufficient for close approximation of the molar compositions.

The growth of $IIIV_yV_{1-y}$ type ternaries, although none were performed, face the same complications as do quaternary materials: how to accurately determine the group V ratio. There have been various publications that discuss methods of calculating group V ratios or detecting incorrect ratios via slight

RHEED pattern changes [i.e. 35,36]. However, it is still quite difficult to determine how to adjust the group V flow rates to more accurately obtain the desired composition.

From the study of the ternaries InAsP and GaAsP, Hou, *et al* determined that virtually 100% of the supplied As bonds with In and that the incorporation of As with Ga is dependent on the amount of P present [32]. Therefore, in general, for InGaAsP, As has a higher incorporation rate than does P when P is supplied in excess [37]. This incorporation difference suggests that the phosphine flux can be kept relatively constant during the growth of all InP and InGaAsP layers; this holds true for InGaAsP layers with Ga concentrations less than ~0.3. For InGaAsP with higher concentrations of Ga, the relative sticking coefficient of P and As will begin to equalize due to the increased amount of Ga in the layer [38]. However, also of significance in determining the incorporation of As versus P in a quaternary film is the substrate temperature, the growth rate, and any strain in the InGaAsP layer; the parameter space created by considering the above mentioned points is quite large and thus makes the growth of InGaAsP materials quite complex.

Compositional Modulation

Also of concern for growth of InGaAsP is the miscibility gap; a region mainly dependent on substrate temperature, that comes about due to bond length differences of the binary end-components, and can occur in materials composed of three or more elements [39,40,41]. With the increasing demands placed on material quality the existence of compositional modulation within optoelectronic devices will significantly affect the device performance. Specifically for InGaAsP, the low energy end-components are InAs and GaP; thus compositions of InGaAsP that lie within the miscibility gap will exhibit regions rich in InAs and GaP [16]. (For InGaAs materials, lateral composition modulation occurs in the form of GaAs- and InAs-rich regions [13].) The existence of a miscibility gap was first observed in InGaAsP layers deposited by Liquid Phase Epitaxy (LPE) [12,42], and more recently has been investigated for GSMBE [43,44]. The miscibility gap of InGaAsP is speculated to be a minor factor in GSMBE growth since it is expected that the lowest energy state of a deposited material is lattice-matched to the substrate and not strained (with InAs- and GaP-rich regions) [16]. Furthermore, the growth temperatures used in GSMBE of InGaAsP are relatively low (i.e. as compared to LPE). However, for compositions that lie within the miscibility gap, the tendency for the material composition to modulate does still exist [16]. Investigations by LaPierre, *et al* have shown experimentally that the severity of the miscibility gap is also dependent on the group V overpressure and the type of strain within the layer [44,45]. Specifically, tensile-strained layers exhibit more severe compositional modulation. An increase in the group V overpressure has been shown to reduce

the severity of compositional modulation by decreasing the diffusion length of the group III species (thus reducing the possibility of In preferentially bonding to As and Ga to P).

Figure 2.9 is the resulting calculation of the miscibility gap (using the regular solution approximation

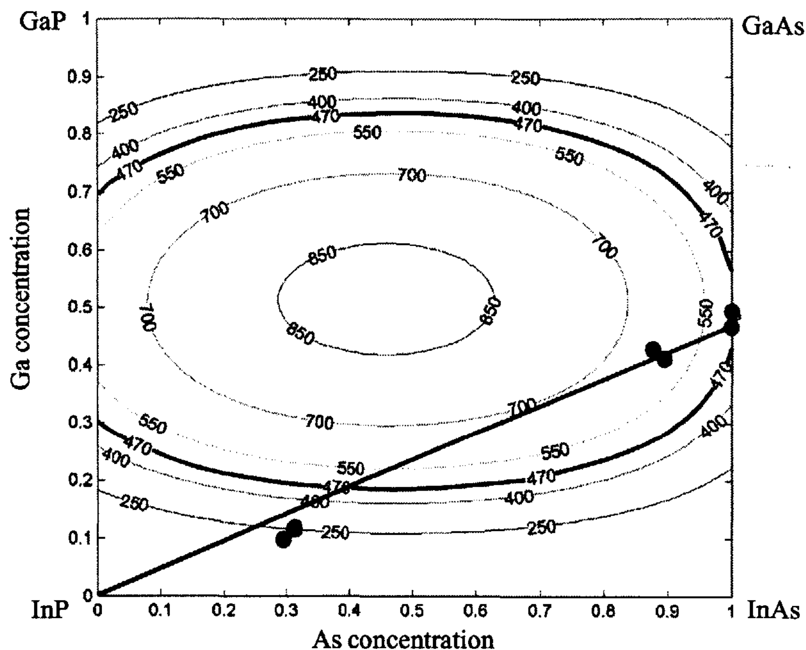

Figure 2.9 Calculation of the miscibility gap for InGaAsP materials, using the regular solution approximation for the solid solution (after [40]). The area within each ring designates the miscibility gap for a given substrate temperature. The diagonal line represents the compositions of InGaAsP lattice-matched to InP [following Eq. (2.4)]. The filled-in circles are compositions that have been deposited in the GSMBE system at MIT. 470°C is the approximate substrate temperature used for layers and structures presented in this thesis.

for the solid solution, following Onabe [40]) for the growth conditions typically used in the GSMBE system at MIT. The area inside the rings designates the miscibility gap for a given substrate temperature. Also graphed in Figure 2.9 is the composition of numerous InGaAs(P) epilayers with respect to the miscibility gap. The growth of InGaAs and InGaAsP having large concentrations of Ga has proved to be the most difficult materials to deposit in the system at MIT; comparison of the compositions and the miscibility gap calculation suggest that the materials of concern lie within the miscibility gap. Recall, the typical substrate temperature used for InP-based materials was ~470°C (see thick black contour line in Figure 2.9).

Shown in Figure 2.10 is a series of PL measurements of an $In_{1-x}Ga_xAs_yP_{1-y}$ ($x \sim 0.12$, $y \sim 0.3$) layer (total thickness ~280 nm), 0.3% compressive-strained, that resides outside of the calculated miscibility gap

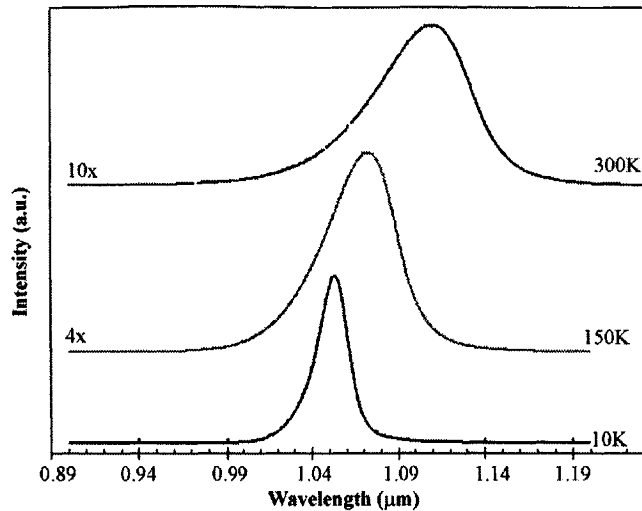

Figure 2.10 PL at various temperatures for ~280 nm of $In_{1-x}Ga_xAs_yP_{1-y}$ (x ~ 0.12, y ~ 0.3), slightly compressive-strained. Graphs are offset for clarity.

(see Figure 2.9). The PL feature at room temperature is broad yet typical of an InGaAsP epilayer, and narrows as the sample temperature is decreased. Furthermore, a bandgap shift of ~68 nm is expected between 300K and 10K, and is observed.

Depicted in Figure 2.11 are PL measurements performed by La Pierre, *et al* [13] on GSMBE grown material that illustrates the variation of the PL spectrum with temperature for layers in which compositional modulation has been observed. Peaks labeled "1" correspond to a PL signal from InAs-rich regions. Peaks labeled "2" correspond to the expected composition, and peaks labeled "3" correspond to the PL signal from GaP-rich regions. For sample (*h*), in which the epilayer is both tensile-strained and resides well within the calculated miscibility gap, the PL spectrum appears to be relatively temperature independent. For samples (*e*) and (*i*), that do not lie as deeply within the calculated miscibility gap, the PL spectrum varies significantly with sample temperature; the features corresponding to the compositionally modulated regions are labeled in Figure 2.11. At room temperature, it is anticipated that the PL signal from the GaP-rich regions, which are tensile-strained and thus the bandgap transition is between the light-hole valence and conduction band, will be apparent. (The carrier recombination time in light-hole band transitions is shorter than heavy-hole transitions [13 and reference within].) As the temperature is decreased, it is speculated that the excited carriers become trapped in the InAs-rich, lower bandgap regions, increasing the PL signal from the InAs-rich material.

Following LaPeirre, *et al* [44], the temperature dependence of the PL spectrum for InGaAs(P) materials has also been investigated. In the range of samples deposited at MIT, the general trend observed

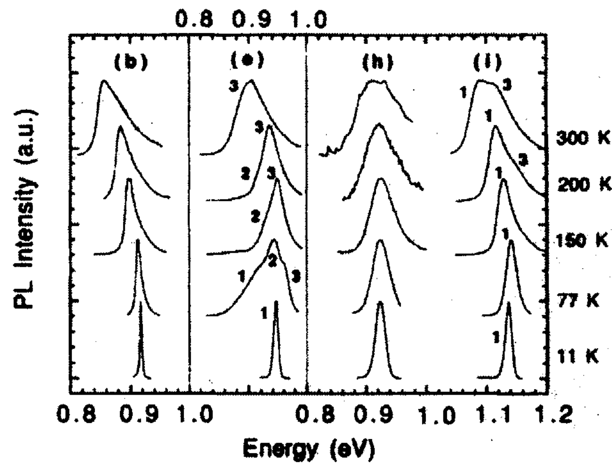

Figure 2.11 PL measurements at multiple temperatures illuminating the spectral dependence of compositional modulation. Sample (b) is a compressive-strained InGaAsP (x~0.25, y~0.7) layer just inside the calculated miscibility gap. Sample (e) is a lattice-matched InGaAsP (x~0.33, y~0.7) layer within the calculated miscibility gap. Sample (h) is a tensile-strained InGaAsP (x~0.4, y~0.7) layer within the miscibility gap. Sample (i) is a tensile-strained InGaAsP (x~0.25, y~0.37) layer just inside the calculated miscibility gap. Figure from [13].

in PL measurements of quaternaries having large concentrations of Ga and As, as well as InGaAs layers, is the presence of a feature at λ~1.55 μm, that appears to be independent of temperature. Shown in Figure 2.12 is an example of a typical series of PL measurements observed for InGaAs epilayers. (Note: the

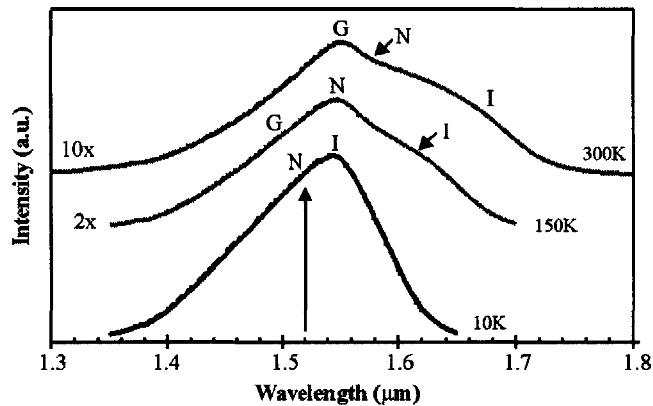

Figure 2.12 PL at various temperatures for ~ 470 nm of $In_{1-x}Ga_xAs$ (x ~ 0.494), slightly tensile-strained. Graphs are offset for clarity. Peaks labeled "G" correspond to GaAs-rich features, peaks labeled "N" correspond to the expected InGaAs features, and peaks labeled "I" correspond to InAs-rich features.

~1.55 μm feature observed can not be attributed to a harmonic of the 514.5 nm argon laser line since a highpass filter (> 550 nm) is used for all PL measurements.) The epilayer is slightly tensile-strained [x ~ 0.494 and total InGaAs thickness (comprised of 2 layers, ~400 nm and ~ 70 nm, with a ~50 nm InP spacer) ~470 nm]. The 300K feature labeled "N" is attributed to the average desired composition of the InGaAs material as determined by HRDAXD. Compositionally modulated InGaAs segregates into GaAs- and InAs-rich regions (see vertical axis in Figure 2.9). The GaAs-rich material is expected to be apparent at shorter wavelengths, and most likely gives rise to the feature located at ~1.55 μm in the 300K spectrum. Furthermore, the long wavelength feature is quite broad, and it would not be surprising that a portion of the measured intensity is due to the InAs-rich regions. As the temperature is decreased, the PL feature due to the InGaAs composition is expected to shift to shorter wavelengths by ~40 nm at 150K (comparing to that observed in Figure 2.10), and by ~60-70 nm at 10K. The peaks labeled "N" in both the 150K and 10K spectra correspond to the anticipated shift. The peaks labeled "I" are attributed to InAs-rich material and, as would be expected, become more dominant at low sample temperatures.

The PL spectra depicted in Figure 2.13 are taken from a ~200 nm InGaAs (x ~ 0.47) layer, lattice-matched to InP. The shifting of the PL features is more severe, and thus more difficult to decipher. This type of PL signature has been observed for InGaAs layers deposited on both InP and GaAs substrates. According to HRDAXD measurement, the broad long wavelength feature is due to the average InGaAs composition. Although the 300K feature at ~1.55 μm may be attributed to GaAs-rich material, it is difficult to correlate the observed PL features to expected material parameters due to the large difference between the 300K and 150K spectra.

In order to more fully characterize the InGaAsP and InGaAs materials, a more detailed study of the GSMBE growth conditions and resulting layer quality needs to be undertaken. Although the presence of the miscibility gap is attributed to the multiple features observed via PL, measurement techniques such as transmission electron microscopy (TEM) would definitively determine the existence of compositional modulation. Methods demonstrated by La Pierre, *et al* for reduction of compositional modulation in GSMBE growth include, a reduction in surface diffusion lengths (via an increase in the group V overpressure or a decrease of the substrate temperature) [44] and the addition of atomic hydrogen during deposition for modulation reduction via the same mechanism [46]. The performance of broad-area lasers has confirmed an increase in material quality with the addition of atomic hydrogen [47].

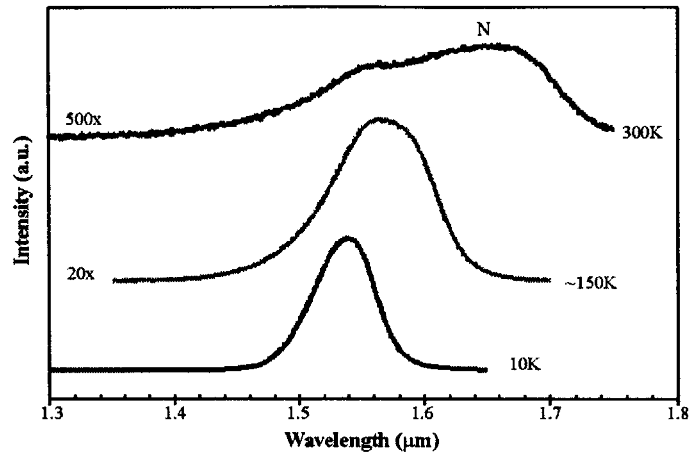

Figure 2.13 PL at various temperatures for ~200 nm of $In_{1-x}Ga_xAs$ ($x \sim 0.47$), deposited on InP. Graphs are offset for clarity. Peak labeled "N" is attributed to the average InGaAs composition.

3

GSMBE Deposition on Atomic Hydrogen-Cleaned Surfaces

3.1 Low Temperature Atomic Hydrogen-Assisted Oxide Removal

Prior to epitaxial growth, the amorphous native oxide must be removed from the surface of the semiconductor sample in order to expose the substrate, which provides the crystallographic template. Oxide desorption is typically performed thermally, however it is a process that is not rigorously controllable, and is dependent on variables such as substrate age, doping, sample preparation, and mounting. In order to more reliably remove the native oxide from a surface, a low temperature atomic hydrogen-assisted oxide removal process has been implemented. A high temperature cracking cell with a tungsten filament at ~2100°C (placed in a standard effusion cell position) is used to decompose H_2 prior to entry into the Riber 32P GSMBE reactor. The sample is placed in the typical growth position (in contrast to ECR-generated hydrogen-plasma cleaning, for which the hydrogen radicals must be incident on the sample at very shallow angles [52]) and is exposed to the hydrogen flux via the opening of shutters. The hydrogen-cleaning process is performed at a substrate temperature below that in which the group V species will desorb from the sample surface. For InP-based materials, the hydrogen cleaning is performed at a substrate temperature of ~200°C, with a chamber pressure of $\sim 1.5 \times 10^{-5}$ Torr. For GaAs-based materials, the hydrogen cleaning process is performed at a substrate temperature of ~480°C, with the same overpressure.

The use of an atomic hydrogen-assisted oxide removal process provides added flexibility for epitaxial deposition. Since the hydrogen cracker is located within the GSMBE reactor, once the oxide is removed, the sample need not be transferred or manipulated in any manner prior to growth, minimizing contamination of the cleaned surface. Additionally, material deposition is able to be nucleated at lower

temperatures, without the need to increase the substrate temperature to remove the oxide followed by a possible temperature decrease to begin deposition. Further advantages of utilizing atomic hydrogen for oxide removal is the passive nature of the process, unlike hydrogen-plasma cleaning in which the hydrogen atoms are ionized and damage to the semiconductor surface is dependent on the incident angle. Atomic hydrogen also cleans the semiconductor surface via removal of surface contaminants such as carbon; secondary ion mass spectrometry (SIMS) studies by J.M. Milikow revealed a decrease in the levels of carbon at the substrate-epilayer interface following atomic hydrogen cleaning of an InP substrate for 10 minutes at ~240°C [26]. Chun, *et al* found that atomic hydrogen cleaning of an InP surface for ~30 minutes at 350°C, with a tungsten filament temperature of ~1500°C, was required for complete removal of surface carbon contamination; in contrast, thermal removal of carbon was accomplished by heating the InP sample to ~530°C under an arsenic flux [53]. For the atomic hydrogen-cleaned procedure developed for this thesis (~5 minutes at ~200°C), probing of the substrate-epilayer interface via AES reveals no detectable carbon.

Atomic hydrogen cleaning of both InP- and GaAs-based materials prior to epitaxy has been performed. The use of the hydrogen cleaning technique for regrowth of InP on GaAs will be discussed in Section 3.2. The use of atomic hydrogen cleaning to prepare rectangular-patterned surfaces for GSMBE deposition will be addressed in Section 3.3.

3.2 Regrowth of InP/InGaAs Heterostructures and Quantum Wells on GaAs-Terminated Distributed Bragg Reflectors

For the fabrication of semiconductor saturable absorber mirrors, GSMBE deposition of InP-based materials on GaAs has been investigated. Semiconductor saturable absorber mirrors are comprised of a distributed Bragg reflector (DBR) and an absorber region, as seen in Figure 3.1. The current devices are designed for fiber-based and solid-state laser cavities with emission wavelengths near 1.55 μm. Thus, use of an InP-based DBR having > 99% reflectivity, that is not absorptive at 1.55 μm, requires ~ 40 pairs due to the small difference in index of refraction between the available materials; the associated deposition time for such a structure via GSMBE is on the order of 24 hours. A DBR in the GaAs materials system, e.g. GaAs/AlAs, has a much larger refractive index difference between the chosen materials (Δn ~ 0.46) and thus requires nearly half the number of layers for the same reflectivity. Further details of the absorber mirror structures will be discussed in Section 5.2.

Of concern when mating two material systems, e.g. InP and GaAs, is the induced strain (on the order of ~3.8%) and the generation of defects. As will be addressed in more detail in Section 5.2.1, defects in the InP absorber region are not detrimental to the performance of the device; in fact, the presence of growth-

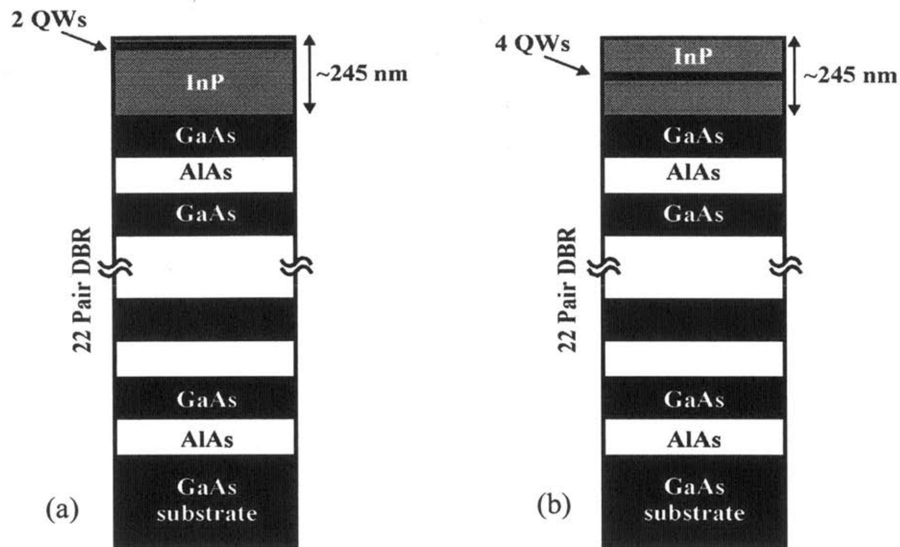

Figure 3.1 (a) ~245 nm of InP, containing two InGaAs quantum wells centered ~220 nm from the GaAs, deposited on a GaAs/AlAs DBR. (b) ~245 nm of InP, containing four quantum wells centered within the InP layer, deposited on a GaAs/AlAs DBR.

generated defects decreases the carrier lifetime and is beneficial to the absorber mirror performance in laser cavities.

InP has been deposited on both GaAs substrates as well as regrown on GaAs-terminated GaAs/AlAs DBRs. Deposition on the substrates is performed without breaking vacuum; the oxide is desorbed thermally and the GaAs buffer layer is deposited at ~640°C (as measured by a thermocouple), then the substrate is decreased to ~480°C for deposition of the InP/InGaAs material. In the case of regrowth on DBRs, the oxide is completely removed via the atomic hydrogen-assisted oxide removal technique. The hydrogen cleaning is performed at a sample temperature of ~480°C for ~10 minutes, with an overpressure of ~$1.5x10^{-5}$ Torr. The oxide removal is verified via observation of a (2x4) RHEED pattern a few minutes after introducing the atomic hydrogen. Following confirmation of oxide removal, AsH_3 is introduced into the chamber in order to create an arsenic-stabilized surface, and the RHEED pattern changes to (1x1). Prior to deposition of InP (at the sample temperature of ~480°C), the GaAs layer is flooded with phosphorus for 10-30 seconds, and then the InP layer is nucleated. As the critical thickness of InP on GaAs is on the order of a few angstroms, the InP overlayer relaxes immediately and the RHEED changes to (2x4), suggesting a fully relaxed InP layer. The InP growth rate is roughly 0.5 μm/hr, and the V/III ratio is roughly 8.5.

The resulting surfaces of the InP regrowth are slightly rough, but not unexpected given the large lattice-mismatch; shown in Figure 3.2 is a typical Nomarski microscopy image of the surface of InP

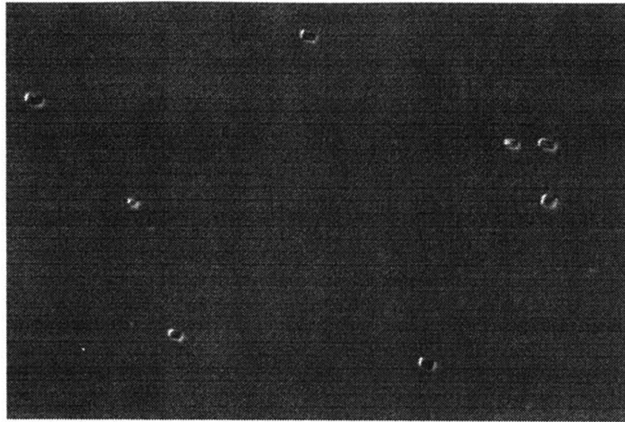

Figure 3.2 Nomarski contrast microscopy image of ~ 250 nm of InP (containing two InGaAs quantum wells) deposited on a GaAs-terminated DBR. Magnification is 200x. Any visible vertical and horizontal striations are caused by the printer.

regrown on a GaAs-terminated DBR. Advantages of this hydrogen-cleaning technique are the lack of elevated substrate temperatures (i.e. 640°C), and the associated time required to ramp the temperature.

For InP/InGaAs layers deposited on a hydrogen-cleaned GaAs/AlAs DBR at a substrate temperature of ~480°C, the carrier lifetime within the InGaAs material, as determined by dynamic differential reflectivity measurements, ranges between 40 and 100 ps. The lifetime variation is dependent on the location of the InGaAs material with respect to the InP/GaAs interface. Cunningham, *et al* use a thermal annealing technique to deposit a "strain relief layer" (via GSMBE) having a defect density that results in significantly shorter InGaAs carrier lifetimes, on the order of ~ 14 ps (for two InGaAs quantum wells centered ~220 nm from the InP/GaAs interface) [126]. The growth procedure followed to obtain a "strain relief layer" is essentially intentional creation of additional dislocations so as to reduce the lifetime of the carriers [54]. A thin layer of InP (~18 nm) is first deposited at a low substrate temperature (~ 400°C), with continued deposition of InP while increasing the substrate temperature to 520°C (total InP thickness of ~ 30 nm). The sample is then annealed at 650°C in the presence of an excessive phosphorus flux for 5 minutes, and then returned to 500°C for deposition of the InP/InGaAs absorber region. Increasing the substrate temperature to 650°C effectively evaporates both the P and In from the surface, as the desorption temperature for P is ~356°C and In evaporation becomes significant at temperatures above ~500°C. The large phosphorus flux most likely causes phosphorus to replace the arsenic on the surface, as the arsenic is also desorbed from the sample surface at such high temperatures (desorption temperature near 550°C). Since the sample temperature is decreased to that used for deposition of InP in a phosphorus overpressure, a GaP-like surface is created. Thus, one may speculate that the reason for such short carrier lifetimes in the

InGaAs material observed by Cunningham, *et al* is the near ~7.6% lattice-mismatch between a GaP-like surface and InP.

As is expected from the InP-GaAs lattice-mismatch, photoluminescence measurements of the quantum wells suggest that the material is slightly degraded. Shown in Figure 3.3 is a typical 300K PL spectrum of an InP-absorber region, containing two InGaAs quantum wells (~ 6 nm) centered ~220 nm from the GaAs interface; the full-width at half-maximum (FWHM) of the quantum well feature is ~60 meV, suggesting slightly degraded material.

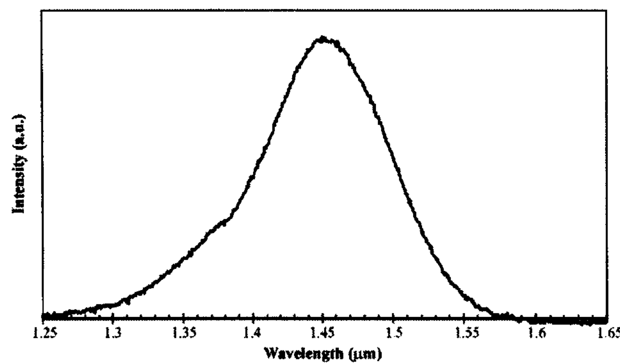

Figure 3.3 300K PL spectrum of ~250 nm of InP containing two InGaAs quantum wells (centered ~ 220 nm from the GaAs-InP interface) deposited on GaAs.

An HRDAXD measurement of the same two quantum well absorber structure discussed above, deposited on a 22-pair GaAs/AlAs DBR, is shown in Figure 3.4. Two significant features are readily

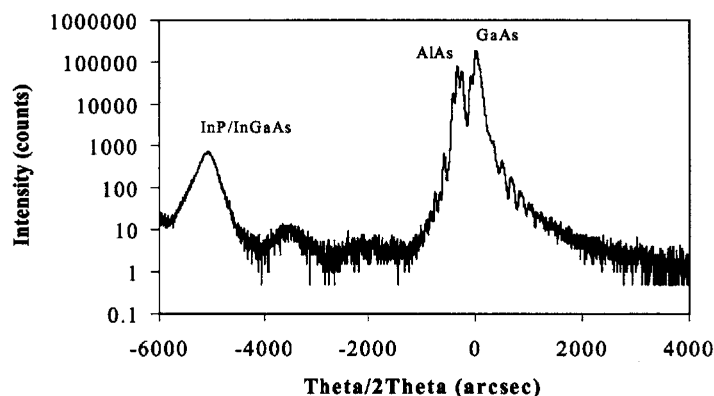

Figure 3.4 HRDAXD scan of a ~250 nm InP/InGaAs region deposited on a GaAs/ AlAs DBR.

apparent: numerous features near $\theta/2\theta \sim 0$ and a single feature located at $\theta/2\theta \sim -5300$ arcsec. The two distinct peaks near $\theta/2\theta \sim 0$ are due to the GaAs (substrate and epilayer) and the AlAs, with the numerous

fringes in the vicinity due to the periodicity of the DBR. From the 3.8% compressive strain exerted on the InP when deposited on GaAs, the InP relaxes nearly instantaneously (as evidenced by RHEED). From dynamical x-ray diffraction simulations, the InP is ~95% relaxed and gives rise to the feature located at $\theta/2\theta$ ~ -5300 arcsec. The near full relaxation is further confirmed as the angular spacing between the 95% relaxed feature and the GaAs substrate is similar to the expected spacing between the (400) GaAs and InP Bragg angles. The InGaAs quantum wells are deposited on the 95% relaxed InP, and will thus attempt to form to that template. As the InGaAs layers are thin (~6 nm) the lattice will elastically adjust to conform to the relaxed InP lattice, and will thus exhibit almost no relaxation. InGaAs and InP deposited on the 95% relaxed InP layer, experiencing nearly no relaxation, will satisfy the same Bragg condition as the 95% relaxed InP layer.

The defects generated as a result of the material relaxation are typically misfit dislocations and act as non-radiative recombination centers. In many applications, e.g. lasers, these defects are undesirable and result in degraded device performance (i.e. increased threshold currents). In the case of semiconductor saturable absorber mirrors, generation of non-radiative recombination centers significantly reduces the carrier lifetime and thus the absorber will recover from bleaching more rapidly (see Chapter 5 for more details on device operation). Since the defects are generated at the InP-GaAs interface, the carrier lifetime of InGaAs quantum wells is expected to vary with distance from the lattice-mismatched interface. Lattice-matched layers deposited on InP typically display a carrier lifetime of ~ 1 ns [55]. For two quantum wells centered ~220 nm from the defect-generating interface, the observed average carrier lifetime is ~100 ps. For four quantum wells centered ~110 nm from the GaAs-InP interface, the observed average carrier lifetime is ~50 ps.

Preliminary studies of the PL intensity and FWHM as a function of the InGaAs quantum well distance from the GaAs-InP interface have also been carried out. The structures investigated are depicted in Figure 3.1. For the structures containing two quantum wells, centered ~220 nm from the GaAs/InP interface, the FWHM of the 300K PL feature is ~ 60 meV. A FWHM of 60 meV is rather large for quantum wells, however, for the same structure deposited on an InP substrate, the FWHM of the room temperature PL feature is also on the order of 60 meV. Thus, the generation of defects does not significantly broaden the PL feature, but rather may have a contribution that is undetectable since the quantum well signal is inherently broadened. (The cause for the 60 meV FWHM from quantum wells structures on InP substrates is unknown; speculations are variation in quantum well thicknesses, miscibility gap-induced broadening, or interfacial layers.) The most significant difference between the PL features of quantum wells deposited on InP and GaAs is the ~20x decrease in intensity observed for the GaAs-based structures. This reduction

in intensity is not surprising due to the generation of non-radiative recombination sites caused by the large lattice mismatch between GaAs and InP.

For structures containing four quantum wells, centered ~110 nm from the GaAs/InP interface, the observed FWHM of the PL feature is also ~ 60 meV. The resulting signal intensity, however, is reduced by ~200x with respect to the InP-based structure. The intensity reduction is commensurate with the location of the quantum wells being closer to the GaAs/InP interface. For structures containing six quantum wells, centered ~110 nm from the GaAs/InP interface, the resulting PL signals are extremely weak, ~1000x less intense than the InP-based structures. The significant decrease in the PL intensity observed for the six quantum well structure is attributed to the increase in Ga- and As-containing material located in closer proximity to the InP/GaAs interface. Since Ga and As have shorter migration lengths than In and P at the chosen growth temperature (~480°C), the likelihood of defects and non-radiative recombination centers propagating through the quantum well region is high. Comparison of the lifetimes measured via pump-probe analysis and the observed PL signal intensities corroborate the increase in non-radiative recombination centers in the quantum wells located closer to the InP/GaAs interface.

3.3 Low Temperature Atomic Hydrogen-Assisted Oxide Removal from Rectangular-Patterned Surfaces

The ability to preserve a patterned surface prior to material deposition is contingent upon minimization of exposure to elevated temperatures. For overgrowth of InP patterned surfaces, reduction of exposure of the surface to temperatures required for both oxide desorption and GSMBE growth (~480°C) must be minimized, otherwise In atoms will easily migrate and minimize any existing surface curvature [56]. The patterned surfaces investigated are rectangular-shaped gratings patterned in both InP substrates as well as in InGaAsP epitaxial layers. The gratings were fabricated via x-ray lithography and reactive ion etching (RIE). Following the etching, the samples are cleaned via a standard degrease process (warm Trichloroethylene, Acetone and Methanol). Prior to introduction into the GSMBE system, the patterned surface is lightly etched via wet chemical etchants to simultaneously remove contaminants not removed via the degrease process and also to remove a portion of the RIE-incurred crystallographic damage. As indicated by Auger Electron Spectroscopy (AES), following the degrease and wet etch procedures the surface of the patterned samples is equivalent to that of an epi-ready wafer, as seen in Figure 3.5.

In order to more reliably remove the native oxide from the grating surface, a low temperature atomic hydrogen-assisted oxide removal technique has been utilized. The hydrogen-cleaning process is performed at a substrate temperature of ~200°C for five minutes, with a background pressure of ~1.5×10^{-5} Torr. 200°C is significantly below the temperature at which phosphorus will desorb from the sample surface

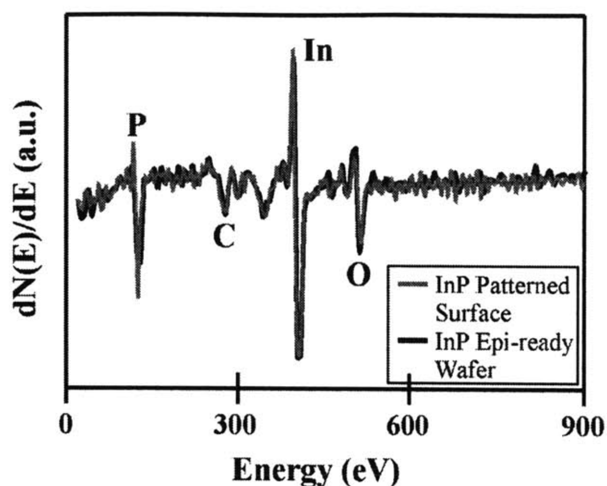

Figure 3.5 Auger Electron Spectroscopy scans of a patterned InP surface and the surface of an InP epi-ready wafer. The relative magnitude of elements on the surface of both samples is nearly identical.

(~365°C), thereby minimizing the movement of In atoms and leaving the grating pattern unaltered. Figure 3.6 depicts (a) a Scanning Electron Microscopy (SEM) image and (b) a (400) Reciprocal Space Map (RSM), generated via Triple Axis x-ray Diffractometry (TAD), of a hydrogen-cleaned InP grating. (Details

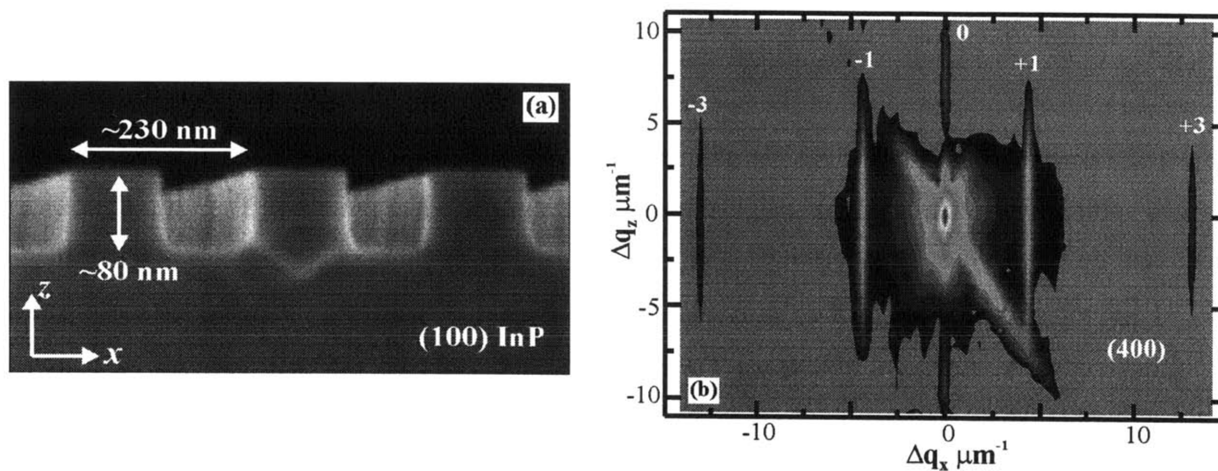

Figure 3.6 (a) Scanning electron micrograph of an InP rectangular-patterned grating. (b) (400) reciprocal space map of the grating shown in (a).

of TAD and RSM generation may be found in Appendix A.) From the SEM image, the grating profile is verified to be rectangular in shape having a toothwidth of ~115 nm and a grating depth of ~80 nm, with the

y-direction [see Figure 3.6(a)] close to $[0\bar{1}\bar{1}]$. Also observable in the SEM image are modulations along the vertical sidewalls due to the RIE-transfer of an etch mask having rough edges. The RSM [Figure 3.6(b)] is generated perpendicular to the grating profile [x-rays incident along the x-direction, Figure 3.6(a)], therefore satellite fringes from the in-plane periodic surface corrugation are visible. (The diagonal feature apparent in Figure 3.6(b) is the 'analyzer streak' and is an artifact of the TAD measurement [57].) The uniformity in intensity of the satellite fringes along Δq_z indicates that the grating profile contains straight sidewalls [58]. The maximum intensity of the satellite fringes is shifted slightly towards compression ($\Delta q_z < 0$) with respect to the InP Bragg peak, and is most likely due to slight RIE-incurred crystalline damage of the grating teeth [57]. The intensity of the mth order satellite reflection is proportional to the mth Fourier coefficient of the grating profile [59], thus the absence of the even order satellite reflections is characteristic of a profile having a linewidth:period ratio of 1:2. Additionally, the separation of the satellite reflections corresponds to the period of the analyzed grating [59]; the RSM determined grating period is ~230 nm, and agrees with the as-fabricated grating period. {422} RSMs were also generated for hydrogen cleaned gratings (see Figure 3.7) and analysis confirms the results attained

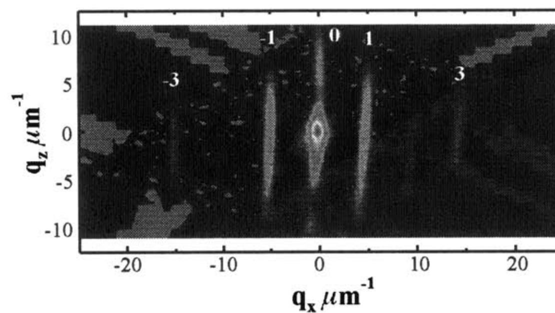

Figure 3.7 {422} reciprocal space map of the corrugated InP surface shown in Figure 3.6(b).

from Figure 3.6(b). SEM images and RSMs of as-fabricated gratings and hydrogen-cleaned gratings are essentially identical, verifying the lack of hydrogen-cleaning-induced damage, as well as preservation of the profile following the wet chemical cleaning step.

Following the hydrogen-cleaning, the sample is ramped to the deposition temperature (~480°C) in an ambient group V flux that corresponds to the composition of the exposed material (P_2 for InP corrugations and an As_2/P_2 mixture for InGaAsP corrugations). The temperature ramp, in combination with the hydrogen-cleaning step, provides an oxide-free surface on which epitaxial growth may be immediately initiated; this process is highly repeatable.

In addition to the use of atomic hydrogen for oxide removal prior to overgrowth, rectangular-patterned InP gratings were exposed to either a P_2 flux or a mixture of As_2 and P_2 during the initial ramp to the growth temperature in an effort to further preserve the grating profile. Work reported on the fabrication of DFB lasers incorporating grating overgrowth indicates that for a sawtooth-patterned InP profile thermal oxide desorption results in significant mass transport-induced degradation of the profile; however, less degradation (less than 50%) is observed if oxide desorption occurs in an As_2/P_2 overpressure [60,25,61,62,63,64,65]. To examine the effect of the group V flux, Figure 3.8 shows $\Delta\omega$ traces [obtained

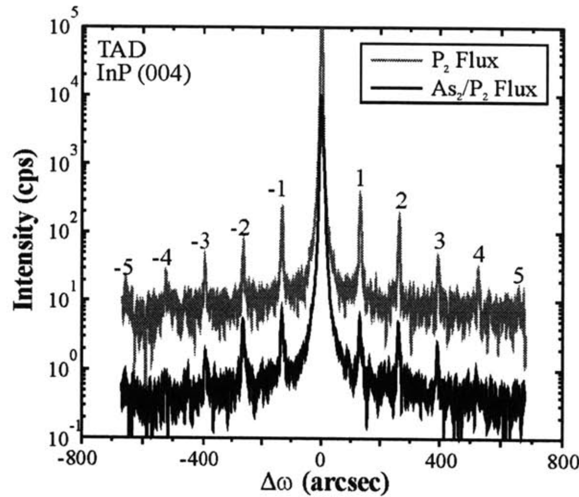

Figure 3.8 TAD (400) $\Delta\omega$ scan for InGaAsP grown on a rectangular-patterned InP grating. The grey line is data obtained from a sample exposed to a P_2 flux prior to nucleation, whereas the black line is data obtained from a sample exposed to an As_2/P_2 flux mixture.

from a (400) RSM] of two nearly identical samples (~200 nm of $In_{1-x}Ga_xAs_yP_{1-y}$ (x ~ 0.12, y ~ 0.3) on a ~230 nm period InP grating with a tooth width:period ratio of 1:2 and ~80 nm trench depths). The grey line is data obtained from the sample exposed to a P_2 flux prior to growth, and the black line is data obtained from the sample exposed to an As_2/P_2 flux. The As_2/P_2 flux ratio was the same as that required for the quaternary epilayer growth with a V/III ratio of ~4. Slight variations in the relative intensities of the satellite reflections are the only apparent differences observed between the two samples and are most likely the result of strain. For each sample, the separations of the satellite reflections indicate a period of ~230 nm, as expected. The presence of the $\pm 2^{nd}$ order satellite reflections in both ω scans is attributed to the presence of strain in the grating teeth since these features are not expected due to the fact that the tooth width:period ratio is 1:2 (this topic will be discussed in more detail in Chapter 4). Furthermore, data obtained from double axis x-ray diffraction and PL appear to be very similar indicating that no significant

differences are apparent due to the type of group V flux used. These observations suggest that regardless of group V overpressure, the hydrogen cleaning process, in conjunction with the use of rectangular-patterned gratings, provides less total profile degradation and considerably more control of the degree of mass transport that will occur prior to overgrowth. Thus, the addition of As for InP profile preservation is not required since the need for extended exposure to elevated temperatures (i.e. for thermal oxide desorption) is eliminated via low temperature hydrogen cleaning.

In order to further investigate the significance of the low temperature atomic hydrogen-cleaning technique, InGaAs, nominally lattice-matched to planar InP, was deposited on both a hydrogen-cleaned and a thermally-cleaned rectangular-patterned grating. Following the growth, the samples were cleaved, stain-etched (using H_3PO_4:HCl (4:1), for 30s at ~20°C to etch the InP), and viewed via SEM. The thermally-cleaned grating, seen in Figure 3.9(a), was exposed to the growth temperature (~480°C) for

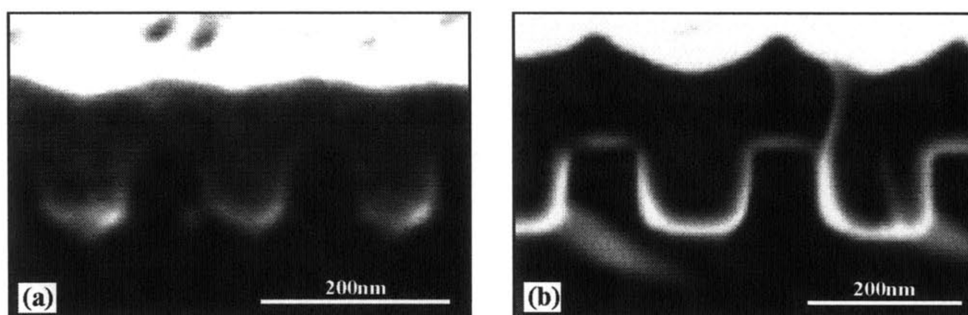

Figure 3.9 (a) SEM of a thermally cleaned InP grating. (b) SEM of a low temperature atomic hydrogen-cleaned InP grating. On both samples, the overlayer is InGaAs nominally lattice matched to InP.

approximately five minutes prior to nucleation of the InGaAs overlayer in order to verify desorption of the oxide (via RHEED). During the additional time at the elevated temperature prior to material deposition, the rectangular grating experienced rounding of the grating teeth and filling of the grating trenches, similar to mass transport effects observed by Izrael, *et al* for InP gratings also oriented (*y*-direction) along $[0\bar{1}\bar{1}]$ [66]. In contrast, the hydrogen-cleaned sample [see Figure 3.9(b)] did not experience observable alteration of the grating profile. Thus, the low temperature atomic hydrogen-assisted oxide removal technique is crucial to the preservation of the as-fabricated rectangular-patterned gratings.

Probing of the patterned surface-overlayer interface via AES does not reveal the presence of any detectable contaminants (i.e. C, O, etc.). (Note: the interface is accessed via ion sputtering; the sputtering capability is resident within the AES-equipped UHV system.) Figure 3.10 depicts a typical scan of the interfacial region of an InP rectangular-patterned grating with a ~200 nm InGaAs overlayer [similar to the

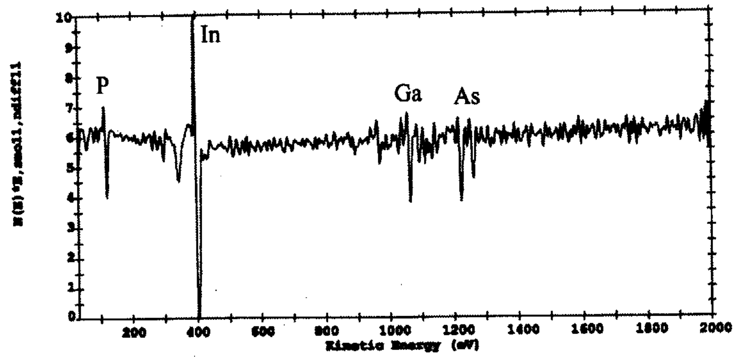

Figure 3.10 Sputtering Auger electron spectroscopy scan of an InGaAs/ patterned-InP-surface interface. The absence of both C and O suggests a very clean patterned InP surface prior to overgrowth.

structure shown in Figure 3.9(b)]. Thus, the use of the low temperature atomic hydrogen-assisted oxide removal process sufficiently prepares the semiconductor surface for overgrowth. Shown for contrast in Figure 3.11 is an AES measurement of the surface of an InP grating, prior to any pre-epitaxy cleaning; the concentration of C and O on the surface are roughly 58% and 12%, respectively.

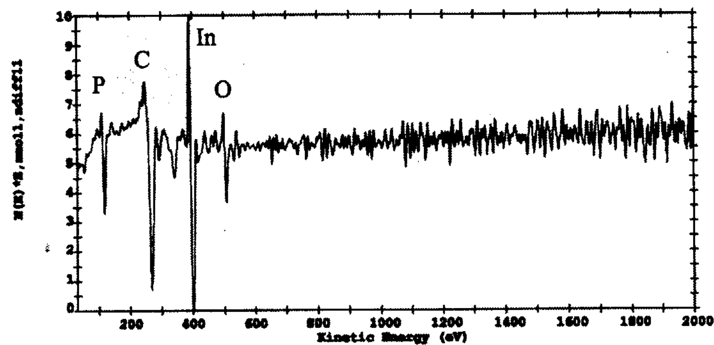

Figure 3.11 Auger electron spectroscopy scan of the surface of an InP grating prior to any pre-epitaxy cleaning. Surface concentrations of C and O are ~58% and ~12%, respectively.

4

Overgrowth of Submicron-Patterned Surfaces for Buried Index Contrast Devices

The ability to epitaxially deposit material on patterned surfaces is a key fabrication step for the realization of many optical sources, optoelectronic integrated circuits, and optical filters. In all cases, the optimum resultant overlayer is of a desired uniform composition with high crystalline quality and devoid of defects. A substantial effort investigating the overgrowth of patterned surfaces has been put forth and spans the range of available epitaxial growth techniques. The deposition of high crystalline quality material on non-planar surfaces is not only necessary for loss reduction (i.e. non-radiative recombination center reduction), but also for increased design and integration flexibility. Although a variety of the overgrowth issues for selective-area epitaxy, optoelectronic integrated circuits, buried heterostructure lasers, etc., are similar, overgrowth of shallow, periodic submicron-dimensioned corrugations will be highlighted here. The material systems to be discussed include (In,Ga)(As,P)/InP and (In,Ga)As/GaAs.

InP-based communication-oriented devices, as well as reduced-dimensionality heterostructures such as quantum wires and quantum boxes, rely on the successful overgrowth of periodic-patterned corrugations. The primary motivation for overgrowth on corrugated surfaces stems from the requirement of creating a variation in the refractive index for photonic or optoelectronic devices such as distributed feedback (DFB) lasers, Bragg-resonant filters [67,68], and resonant grating waveguides [69]. Mastery of the overgrowth process, specifically minimization of overgrowth-generated defects, increases design flexibility by allowing placement of the corrugation anywhere within the device, and also furthers the realization of quantum wire-based devices. Although the grating overgrowth process typically results in a device containing a weak index contrast, burial of a grated material having a large amount of aluminum may offer the potential for high index contrasts via subsequent post-growth oxidation of the aluminum-

containing layer [70]. In general, two types of corrugations have been investigated, namely sawtooth- or V-groove-patterned surfaces and rectangular-patterned surfaces, with the vast majority of previously published research focused on the sawtooth-patterned variety.

For DFB lasers, there are a number of critical fabrication steps that determine the optical characteristics of the device, such as threshold current, operating wavelength, modal selectivity, and spectral linewidth. For example, the single lasing wavelength is dependent on the composition of the active layer, the period (and repeatability) of the grating, the effective refractive index between the active and guiding layers, and the cavity length for devices without $\lambda/4$-shifted gratings. The coupling coefficient is affected by both the depth of the corrugation and the composition of the corrugated material. Additionally, the perfection (or lack of perfection) of the grating affects the degree of light scattering within the laser cavity [71]. Furthermore, for $\lambda/4$-shifted DFB lasers, variations in the grating due to fabrication errors (lithographic- or material deposition-induced) are predicted to significantly affect both the variation in lasing wavelength as well as the single-mode stability of the laser [72]. For the aforementioned reasons, the overgrowth process has a number of very stringent demands that are intimately coupled to the condition of the grating at the onset of growth. The primary surface corrugation that has been implemented in DFB lasers is the sawtooth-pattern. The foremost issue in the overgrowth process is the deposition on various atomic planes [i.e. (100) versus $\{h11\}$] that are typically exposed during grating fabrication. The choice of growth technique, growth parameters, and degree of mass transport-induced grating degradation affects laser performance and ultimately device reliability. A review of the overgrowth of sawtooth-patterned substrates is discussed in Section 4.1.

Waveguide-coupled Bragg-resonant structures provide a means of achieving narrow bandwidth filtering as required by dense wavelength division multiplexing (DWDM) [67]. The overgrowth process is crucial to the successful fabrication of the waveguide-coupled Bragg-resonant channel dropping filter [67,68,73] so as to guarantee the necessary grating strength, and hence the resonator reflectivity, of the as-designed device. Furthermore, non-uniform grating degradation (i.e. via mass transport effects) results in phase-velocity-mismatched resonators, which hinders filter operation [68]. An optimized channel-dropping filter will 'drop' the power at the selected frequency from the main optical bus, evanescently coupling the power to the signal arm. However, mass transport-induced grating degradation during the overgrowth process dramatically affects filter performance by altering the Bragg-resonator reflectivity, thus transferring only a portion of the power in the frequency of interest to the signal arm. The calculated power in the dropped signal for resonators containing rectangular and sinusoidal index modulations (shown in Figure 4.1) illustrates of the severity of the grating profile alteration. The overgrowth process as applied to the fabrication of the channel dropping filter is particularly sensitive to the ability to preserve the

as-designed rectangular-patterned grating profile; in contrast, DFB lasers incorporating a sawtooth-patterned index contrast are tolerant of, and in fact require, some mass transport-induced grating degradation [74]. Overgrowth of rectangular-patterned surfaces with grating preservation will be highlighted in Section 4.2.

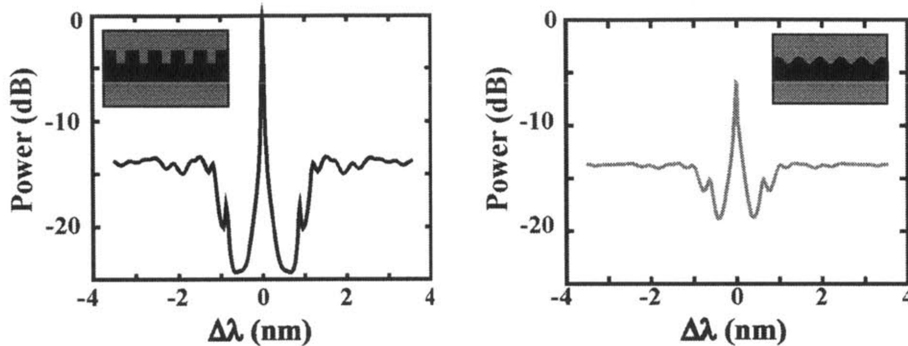

Figure 4.1 Calculated power in the dropped channel for a Bragg-resonant channel-dropping filter. (a) Calculated power for resonators with rectangular index modulations and (b) for resonators with sinusoidal index modulations. Calculation by J.N. Damask, MIT.

4.1 Overgrowth of Sawtooth-Patterned Surfaces: A Review

The deposition on various sawtooth-patterned surfaces (see Figure 4.2(a) for an example) has been the

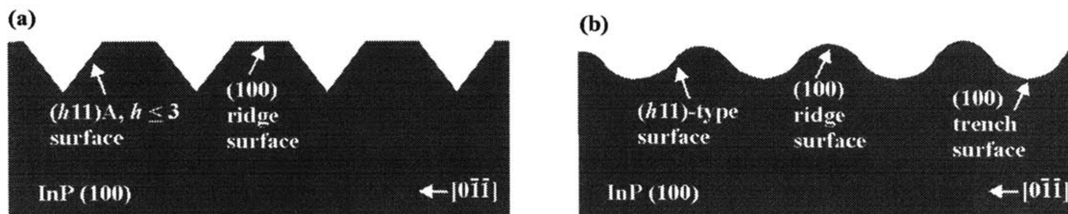

Figure 4.2 (a) Diagram of a sawtooth-patterned corrugation with (h11)A sidewalls. (b) Diagram of (a) following mass-transport alteration of the grating profile.

most studied type of corrugation overgrowth. The overgrown sawtooth profile has been widely implemented in both distributed feedback lasers, and more recently in the fabrication of quantum wires [i.e. 75,76]. Issues that must be addressed regarding sawtooth-patterned overgrowth are preservation of the grating amplitude prior to, and minimization of defects during, overgrowth. The grating profile, whether patterned in InP or InGaAsP, experiences less profile degradation when an As ambient is used during the

substrate temperature ramp to the growth temperature, in combination with limited exposure to elevated substrate temperatures (in the absence of material deposition). The occurrence of growth-induced defects has been minimized through "smoothing" of the exposed facets by utilizing mass transport prior to deposition of the overlayer; shown in Figure 4.2(b) is a diagram of a "smoothed" grating profile. The cross-sectional transmission electron micrograph (XTEM) images of Organometallic Vapor-Phase Epitaxy (OMVPE) grown structures in Figure 4.3 illustrate the need to subject sawtooth-patterned gratings to mass-transport prior to overgrowth. Preservation of the grating may result in severe defect formation due to merging of (h11) facets [74]. Although sawtooth-patterned overgrowth has been very successful, the

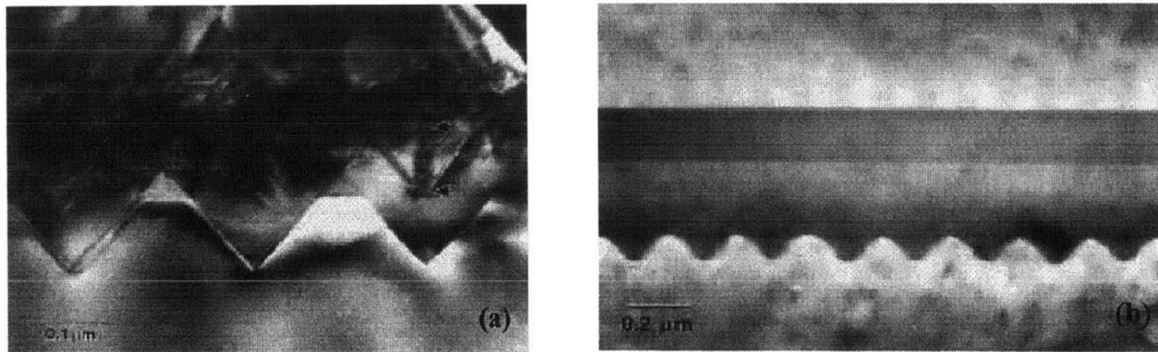

Figure 4.3 Cross-sectional transmission electron microscopy image of (a) InGaAsP deposited via OMVPE on a preserved sawtooth-patterned InP grating, and (b) a DFB laser structure deposited via OMVPE on a "smoothed" sawtooth-patterned InP grating. Images from [74].

aforementioned issues continue to plague the process as well as affect the yield and reliability of devices that incorporate the overgrown corrugations.

InP-based sawtooth-patterned gratings [i.e. see Figure 4.2(a)] are typically fabricated via holographic lithography and wet chemical etching to expose specific crystal planes. Roughness at the edges of the photoresist mask and misalignment to $[0\bar{1}1]$ or $[0\bar{1}\bar{1}]$ result in the exposure of multiple, undesired crystallographic planes; although fabrication optimization can minimize these effects [77], the epitaxial overgrowth is compromised. The exposure of various microfacets severely complicates the overgrowth since atoms diffuse and incorporate differently depending on the exposed crystallographic plane. Although some aspects of the overgrowth may be similar to deposition on substrates of other orientations (i.e. (111)A, (111)B, (110), etc.), (100) planes are typically present in patterned surfaces and therefore adatoms are able to migrate to those facets and more readily incorporate into the crystal structure of the overlayer. (Note, an A face corresponds to a group III surface and a B face to a group V surface.) Investigation of

GaAs substrates patterned with large scale V-grooves (ridge spacing > 1 μm), typically for quantum wire formation, illuminates the difficulties of overgrowth on multiple crystallographic facets. For example, at elevated temperatures (typical MBE growth temperatures) In and Ga adatoms migrate from (100) facets to (111)B facets, resulting in an effectively higher growth rate for the V-groove base; conversely, adatoms migrate from (111)A facets to (100) facets with the result being an enhanced growth rate for the (100) planes [78]. Additionally, the migration of adatoms from (311)A to (100) facets [79] and from (511)A to (100) facets [80] has been observed in GaAs. Although the previous results were determined for large scale GaAs V-grooves, the same type of behavior, although not clearly identified, has also been observed in GSMBE of InGaAs(P) overlayers on InP V-grooves [75,81].

The same adatom migration pattern is detectable in overlayers deposited on submicron-patterned sawtooth gratings. Mullan, *et al* [82] have analyzed the compositional uniformity of InGaAs and InGaAsP deposited by GSMBE on 200 nm period gratings with (311)A sidewalls (corrugation along $[0\bar{1}\bar{1}]$) and found that variations in the overlayer composition are related to the grating profile. Depicted in Figure 4.4

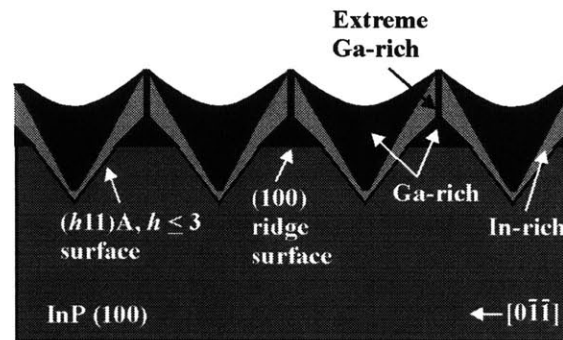

Figure 4.4 Schematic illustration of the proposed overgrowth of InGaAs(P) on submicron period sawtooth-patterned (100) InP substrates containing (*h*11)A sidewalls. The starting grating pattern in InP is outlined in black.

is a model, developed as a result of an extensive literature review, of the proposed compositional variations in the overlayer deposited on submicron-patterned sawtooth corrugations. (A similar model of the strain, due to compositional modulation, within an AlGaAs overlayer deposited on a GaAs sawtooth corrugation has been developed by Darowski, *et al* [91].) From analysis of InGaAs(P) overlayers deposited on InP sawtooth gratings, Mullan *et al* found that the material immediately above the grating teeth is Ga-rich and the material immediately above the grating trench is Ga-deficient [82]. For submicron-sized gratings, the Ga adatom migration length is on the order of the grating dimension. The Ga diffusion length is less than 1 μm for MBE substrate temperatures less than 500°C [88] (specifically along the [011] direction [80,84]).

Therefore, the migration of the adatoms to the preferred facets within the grating, e.g. from the (311)A to the (100) facet, will give rise to composition variation. (Although this type of behavior is also observed in mesa overgrowth [85] and V-groove overgrowth [86], the Ga surface diffusion length is typically smaller than the patterned dimensions.) The surface diffusion length of In is much larger (~25 μm at 520°C [79]) than the submicron grating features. Therefore the probability of nearly equal distribution of In atoms available for incorporation on the various surfaces, taking into account preferred migration from (311)A to (100) surfaces, is not unreasonable. (It is important to note that the adatom diffusion length is also dependent on both the V/III ratio [87,88] and the substrate temperature [80].) Migration of the Ga adatoms from the (311)A facet is clearly observed in the structures of Mullan, *et al* and is evidenced by a 'triangular-shaped region' of Ga-rich material on the (100) surface of the grating ridge [82]. Although the growth conditions and kinetics in OMVPE differ from those of MBE, the same 'triangular-shaped region' on top of the grating ridge is observed on intentionally-preserved InP grating structures having {111}A sidewalls [see Figure 4.3(a)] [74]. For the fabrication of GaAs/AlGaAs quantum wires, Biasiol and Kapon have developed an analytical model incorporating growth rate anisotropies that predicts a 'triangular-shaped region' similar to that observed in InGaAs(P)/InP sawtooth-patterned overgrowth [89].

In addition to the presence of the Ga-rich 'triangular-shaped region' on the grating ridge, Mullan, *et al* also observed a periodic variation in strain contrast across the InGaAs(P) overlayer [82]. Similar variations in strain were observed by Chu, *et al* on well-preserved InP sawtooth gratings [74]. The periodicity of the strain contrast, for all structures, appears to follow the periodicity of the grating profile. As mentioned previously, Mullan, *et al* determined that the material in the grating grooves is Ga-deficient. However, in a comparable structure exhibiting a similar strain contrast, energy dispersive x-ray analysis of material above the grating groove reveals that the material is Ga-rich [90]. At some point during the overgrowth, Ga atoms begin to incorporate within the grating groove, and not solely on the (100) ridge. As atoms incorporate on the (h11)A sidewalls, the groove profile most likely transforms through various higher index {h11} facets similar to that observed in (h11)A V-groove overgrowth [75,81]. As the groove growth front transforms to higher index facets that are more akin to (100) facets, Ga adatoms will begin to incorporate more readily. In addition to the Ga-rich 'triangular-shaped region' on the grating ridge observed by Mullan, *et al*, a thin column of extreme Ga-rich material is present from the top of the Ga-rich 'triangular-shaped region' to the surface of the overlayer; this column of material has a higher concentration of Ga atoms than the 'triangular-shaped region' [82]. The presence of the Ga-rich column is most likely the result of a remaining (h11)-type facet (or facets) along the growth front (with a profile similar to the cusped surface observed by Mullan, *et al* [82,90]). The non-(100) facets along the growth front will not be preferred bonding locations for the Ga adatoms compared to a (100) surface. Thus, the Ga will continue to migrate off the inclined

facets until the (100) growth front overtakes the other existing facets, and the surface planarizes. Therefore, the top of the triangular Ga-rich region must be either a narrow (100) facet or a joining of two $\{h11\}$ facets in a defect arrangement within which Ga atoms strongly prefer to incorporate. The severity of the surface cusping above the (100) ridge, in addition to the magnitude of compositional variation, is a function of both the Ga and As mole fractions in the overlayer. As the concentrations of Ga and As are decreased, both the In and Ga adatom mobilities are effectively increased due to a smaller number of As atoms (with sticking coefficient ~1) arriving at the surface. The combination of a decrease in the number of Ga atoms as well as an increase in the diffusion length of the Ga adatoms will lessen the compositional variations within the overlayer and reduce the overlayer thickness required to achieve a planar surface (this has been observed by Mullan, *et al* for InGaAsP overlayers compared to InGaAs overlayers [82]). Although compositional variations are attractive for the formation of quantum wires and quantum dots, minimization of the compositional modulation in the InGaAsP overlayer is crucial for application to DFB lasers. For typical InP-based laser cladding materials (InGaAsP with a bandgap of ~ 1.2 eV), the concentrations of Ga and As are quite low, thus minor amounts of compositional modulation should be expected and would have a minimal effect on the device.

For sawtooth-patterned gratings having (100) surfaces in the V-groove trenches and {211}-oriented sidewalls, Bhat, *et al* report that dislocation-free overlayers are obtainable [92]. Similarly, in order to minimize the formation of defects during overgrowth of sawtooth-patterned DFB gratings having (111)A sidewalls and sharp V-grooved trenches, Chu, *et al* have determined that a slight smoothing of the grating via mass transport is necessary [74]. The mass transport alteration of the grating reduces the sharp wet chemical etch-defined (111)A planes by effectively transforming the sidewalls to $\{h11\}$ planes with $h \geq 1$ and creating (100) surfaces in the grating grooves; the mass transport of the grating minimizes the generation of defects during overgrowth since the overlayer is nucleated on a (100) surface within the grating groove [see Figure 4.3(b)]. Also, compositional variations within the overlayer are expected to be reduced since all surfaces are either (100) or $\{h11\}$ varieties that contain an arrangement of dangling bonds similar to those on (100) surfaces, thereby reducing facet-directed adatom migration.

The use of mass transport for large-dimensioned structures in which the desired profile is obtained after extended periods of time at elevated temperatures is well documented; Liau, *et al* have found that the exponential decay of InP sinusoidal and rectangular profiles is proportional to the fourth power of the grating period and the fourth root of the decay time, respectively [93]. For much smaller corrugations, with a period on the order of a few hundred nanometers, Nagai, *et al* observed that the bulk of the amplitude degradation occurs within the first fifteen minutes of exposure to elevated temperatures [94]; thus, the amount of profile alteration is significantly less controllable during the initial heating stages and can lead

to significant profile deviations in submicron-patterned gratings. In an effort to counteract the rapid profile alteration and amplitude degradation, yet simultaneously preserve a "smoothed" sawtooth profile, InP and InGaAsP corrugated surfaces are typically exposed to an As/P ambient during the thermal desorption of the oxide [60,25,62,63,64,65]. The near absence of As desorption compared to P desorption at InP growth temperatures effectively reduces the mobility of the adatoms, thereby decreasing alteration of the corrugated surface profile. Although the profile degradation is reduced, it is not completely stifled during the thermal oxide desorption process; gratings typically experience more than 10% amplitude reduction [60,65,25]. The addition of As during thermal cleaning of an InP surface creates an InAsP layer, with the magnitude of As/P exchange not only dependent on the As/P ratio, but also dependent on the exposed crystallographic planes [95]. Although the presence of the InAsP layer has been beneficial for the fabrication of absorptive grating DFB lasers [64], the presence in devices such as Bragg-resonant filters is expected to be detrimental as a result of the grating alteration that occurs in the formation of the InAsP layer.

4.2 Overgrowth of Rectangular-Patterned Surfaces

The investigation into the overgrowth of rectangular-patterned gratings is motivated by the need to fully preserve the as-fabricated grating profile in order to realize devices such as Bragg-resonant channel dropping filters [68]. The strong rectangular-defined index contrast establishes the reflectivity of the Bragg resonators; alteration of the profile from a rectangular shape severely diminishes the filter performance, rendering it virtually useless for high-density WDM applications [73]. To date, the majority of rectangular-like profile overgrowth studies have been applied to larger-dimensioned structures, such as selective-area growth for device integration (e.g. [96,97]) or for buried heterostructure devices (e.g. [98,99,100,101,102]). In general, rectangular profiles are fabricated via reactive ion etching (RIE) which introduces the issue of crystallographic damage of the material in proximity to the etched surface [103,104,105]. The fabricated profiles typically contain vertical sidewall facets of either $(0\bar{1}\bar{1})$ or $(0\bar{1}1)$. The vertical sidewalls are different from the $\{h11\}$ variety of sawtooth-patterned gratings in that both group III and group V atoms are present on the surface and only single dangling bonds are exposed; thus, the incorporation of adatoms and associated migration lengths on the sidewalls are expected to be different than previously discussed for overgrowth of sawtooth-patterned gratings.

Rectangular-patterned gratings, having a ~230 nm grating period, have been fabricated in both InP substrates and $In_{(1-x)}Ga_xAs_yP_{(1-y)}$ ($x \sim 0.23$, $y \sim 0.43$) epitaxial layers deposited on InP substrates. The grating is transferred to polymethly-methacrylate (PMMA) via x-ray lithography and then to SiO_2 via RIE

using a CHF_3 plasma. The grating pattern is etched into the InP (or the quaternary epilayer) to a depth of 80-100 nm using RIE with an $O_2/CH_4/H_2$ gas combination. After removing the SiO_2 mask via a buffered HF dip, the samples are cleaned using a standard solvent degrease process and then briefly etched. The wet chemical etchants (H_2SO_4:H_2O_2:H_2O (1:1:10) for InP and HCl:H_3PO_4 (1:4) for InGaAsP, 30 sec. at room temperature) are utilized to remove a portion of the residual RIE damage without altering the grating profile, as confirmed by scanning electron microscopy (SEM) and triple axis x-ray diffraction (TAD). (Note, details of the TAD measurement technique may be found in Appendix A.) The SEM and TAD measurements of a hydrogen-cleaned InP grating (see Figure 3.6) are essentially identical to those obtained from the gratings both prior to and following the wet chemical etch step. Additionally, Auger electron spectroscopy measurements reveal the presence of In, P, C, and O on the wet chemically-etched gratings in concentrations similar to a planar epi-ready InP substrate (see Figure 3.5). Shown in Figure 4.5 is a

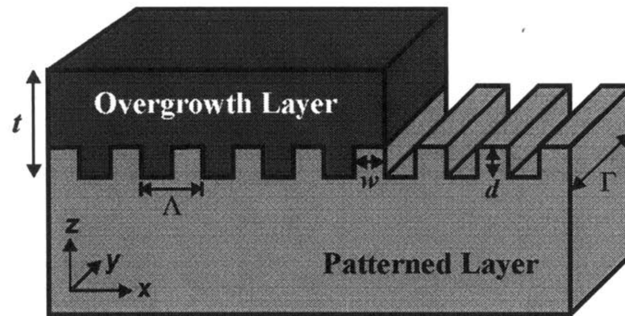

Figure 4.5 Schematic diagram of a generic overgrown structure on a rectangular-patterned surface. (*w*: tooth width at the tooth midpoint, *d*: tooth depth, *Γ*: grating width, *Λ*: grating period, *t*: overgrown layer thickness).

schematic of a typical overgrown rectangular-patterned grating sample. For all samples studied thus far, *Λ*, the grating period, is ~230 nm and *Γ*, the grating width, is typically on the order of millimeters. The other dimensions (*t*, the overlayer thickness, *d*, the grating tooth depth) are sample dependent, and *w*, the grating tooth width at the tooth midpoint is ~115 nm unless otherwise indicated.

The effect of RIE damage on the optical quality of the overgrown structures has been analyzed via photoluminescence (PL). Both patterned and unpatterned $In_{(1-x)}Ga_xAs_yP_{(1-y)}$ ($x \sim 0.23$, $y \sim 0.43$) epilayers were reactive ion etched under the same conditions and to the same depth (~100 nm). Approximately 1 μm of InP was then simultaneously deposited on the etched samples as well as on unetched samples. The only significant difference between the 10K PL spectra, as seen in Figure 4.6, of the etched and unetched or untreated samples was a 10-20X decrease in the luminescence intensity and a slight increase (~3-6 meV)

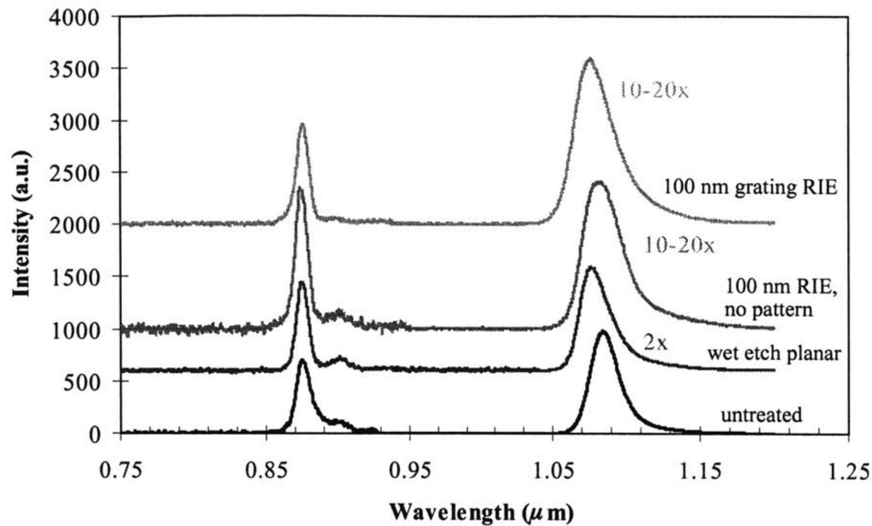

Figure 4.6 10K PL spectra of InP deposited on: untreated InGaAsP epilayer (black line), 30 sec. wet chemically etched InGaAsP epilayer (dark gray line), InGaAsP epilayer with ~100 nm removed via RIE (gray line), and ~100 nm-deep InGaAsP gratings (light gray line). Data is offset for clarity.

of the InGaAsP epilayer full-width-at-half-maximum (FWHM) for the etched samples. The decrease in luminescence is attributed to damage incurred during the reactive ion etching of the grating [103,104,105].

4.2.1 InP Overgrowth of Submicron InGaAsP Rectangular-Patterned Gratings

Structures similar to those required for grating-resonant devices [68,69] have been investigated in which the overgrowth of InP is carried out on a quaternary (QT) grating. Rectangular-patterned gratings have been fabricated in a ~500 nm $In_{(1-x)}Ga_xAs_yP_{(1-y)}$ ($x \sim 0.23, y \sim 0.43$) epilayer (having a tensile strain of $\varepsilon_z \sim -4.5 \times 10^{-3}$) on an InP substrate, with a tooth depth, d, of ~100 nm. As observed via SEM, the grating profile is slightly trapezoidal in shape [$w \sim 100$ nm, see Figure 4.7(a)] and at the bottom of the trench the width is slightly less than 115 nm. Fourier series simulations of the aforementioned trapezoidal grating profile suggest that the $\pm 2^{nd}$ and $\pm 3^{rd}$ order satellite reflections should be of similar magnitude. Intensity in the $\pm 2^{nd}$ order satellite fringes in (400) RSMs of the bare QT grating, due to both alteration of the $w{:}\Lambda$ ratio from 1:2 and the trapezoidal shape, is therefore expected and observed [see Figure 4.7(b)]. The period, as evidenced by the separation of the satellite fringes, is confirmed to be ~230 nm.

Although the grating profile is not perfectly rectangular in shape, the overgrown structure is rather simple, since a binary material is deposited on the QT grating, and hence provides insight into devices containing buried refractive index modulations. Utilizing the low temperature atomic hydrogen cleaning technique discussed in Section 3.3, ~1 μm of InP is deposited on the $In_{(1-x)}Ga_xAs_yP_{(1-y)}$ ($x \sim 0.23$, $y \sim 0.43$) gratings via GSMBE. No compositional modulation is expected within the InP overlayer, thus all additional features present in RSMs are due solely to strain accommodation within the buried grating region. A glancing exit {422} RSM of the overgrown structure is shown in Figure 4.7(c) ($\Delta q_z > 0$

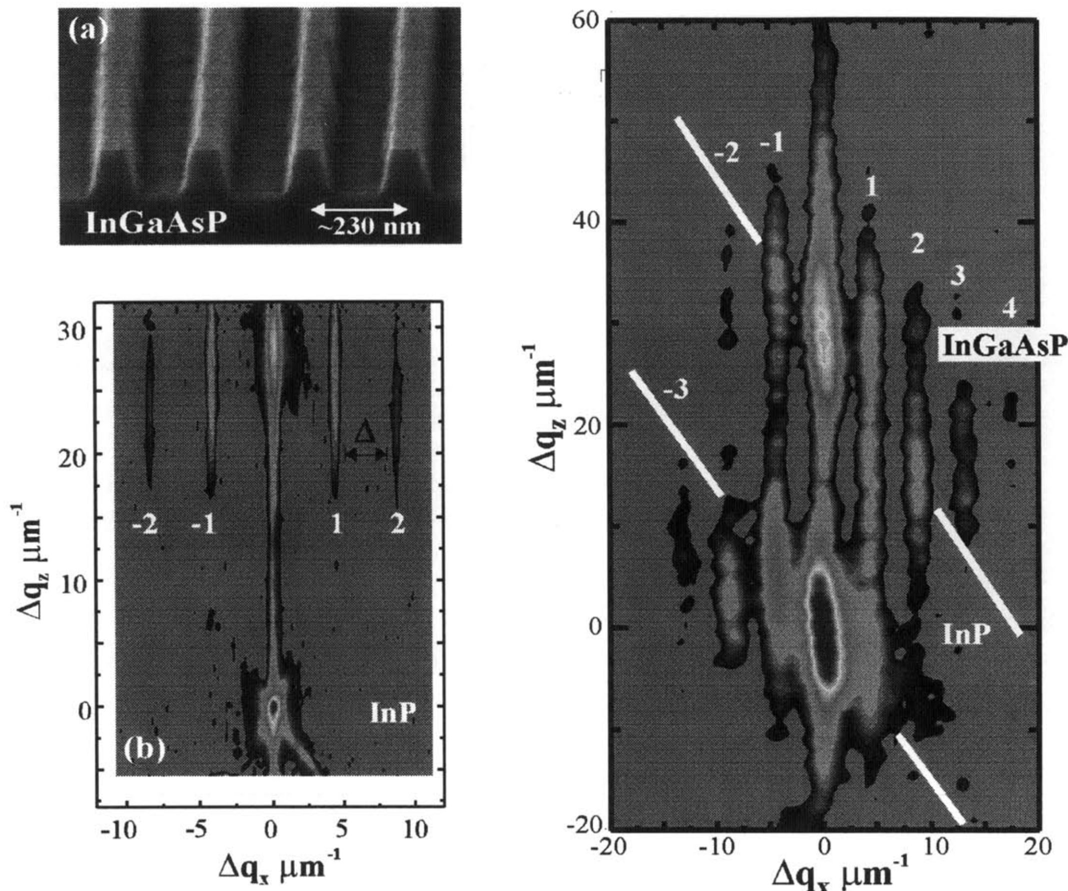

Figure 4.7 (a) SEM image of gratings fabricated in an InGaAsP epilayer. (b) (400) RSM of the gratings depicted in (a). (c) {422} glancing exit RSM of ~1 μm of InP deposited on the InGaAsP gratings depicted in (a). Intensity scale for (b) and (c) is $1\text{-}1 \times 10^4$.

corresponds to a decrease in a_x). In Figure 4.7(c), the satellite reflections originating from the grating are apparent about both the InP ($\Delta q_x = 0$ μm^{-1}, $\Delta q_z = 0$ μm^{-1}) and InGaAsP ($\Delta q_x = 0$ μm^{-1}, $\Delta q_z = 30$ μm^{-1}) Bragg diffraction peaks, as expected. The even order satellite fringes are visible as a result of the QT

grating profile, as previously mentioned. However, the resulting intensity relationship following overgrowth of the grating is such that the $\pm 2^{nd}$ order reflections are of greater intensity than the $\pm 3^{rd}$ order. The additional intensity present in the $\pm 2^{nd}$ order reflections is attributed to the presence of strain within the grating region, and not alteration of the grating profile since preliminary cross-sectional Atomic Force Microscopy (AFM) measurements indicate preservation of the grating profile following overgrowth (see Figure 4.8).

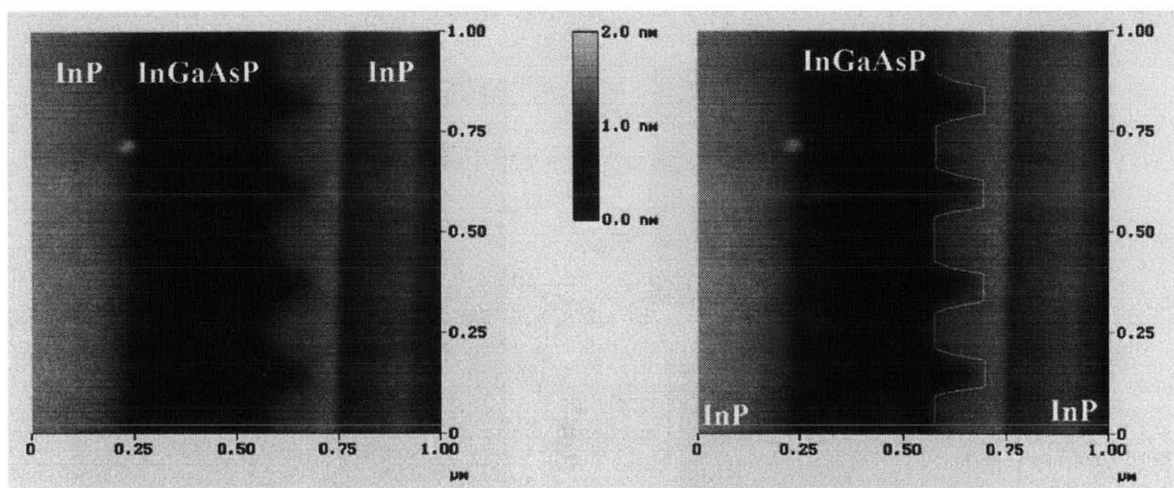

Figure 4.8 AFM images of ~1 μm of InP deposited on the InGaAsP gratings shown in Figure 4.7(a). The white line in the image to the right is the profile of the gratings traced from Figure 4.7(a).

The samples for cross-sectional AFM were cleaved and exposed to air in a clean, vented hood for ~24 hours to allow the materials to oxidize. Differences in height detected by the Si tip are due to differing oxide thicknesses between the materials [106]. The two images in Figure 4.8 are identical; the white line is a profile of the gratings traced from the SEM image [Figure 4.7(a)] and placed on the AFM image. The cause of the height difference observed in the InP overlayer (a decrease of ~7 Å located roughly 150 nm from the grating trench) is unclear. Since the overlayer is a binary material, the atomic hydrogen cleaning process has been used, and the gratings contain both Ga and As (reducing mass transport), the height difference is not expected to be due to the presence of an InGaAsP alloy. Furthermore, the transition is quite abrupt and the region is uniform in height. Were the height difference due to the creation of an InGaAsP alloy during the overgrowth, the composition would likely not be uniform. Thus, the resulting oxide layer would also not be as unvarying as that measured by AFM. A possible explanation for the abrupt height difference is contamination of the cleaved facet.

Similar to glancing exit {422} RSMs of the bare QT gratings, the satellite fringes are no longer symmetric about the InGaAsP Bragg peak, with more severe asymmetry present in the overgrown structure. Upon close inspection of Figure 4.7(c), a number of local maxima of intensity are noticeable in the satellite reflections. The presence of these pockets of intensity suggests a shifting of diffraction envelopes with respect to the Bragg peaks. (The existence of various maxima within the satellite fringes can not be attributed to modulation of the data via the 'analyzer streak', since the 'analyzer streak' does not physically overlap the observed satellite reflections and is of minimal intensity for the four bounce analyzer used for all RSMs depicted.) The diffraction envelopes of both the InP and InGaAsP materials appear to be shifted in an approximately equal and opposite manner and are indicated by the white lines in Figure 4.7(c); features such as these have also been observed by Leprince *et al* for similar structures [107]. As there should be no variation in composition occurring within the InP overlayer or the InGaAsP grating, the source of the diffraction envelope shift is attributed to strain accommodation within the buried grating region. Thus, the strain accommodation is restricted to an alteration of the lattice parameters, a_x, a_y, and a_z (see Figure 4.5 for coordinate reference). The diffraction envelope shift of the tensile-strained InGaAsP grating teeth corresponds to an average decrease in a_x and an average increase in a_z with respect to the QT Bragg peak. The envelope shift of the InP within the grating trenches corresponds to an average increase in a_x and an average decrease in a_z with respect to the InP Bragg peak. A decrease in a_z of InP and an increase in a_z of the InGaAsP within the grating region is necessary to balance the strain of the two materials in the growth direction; in tandem with an increase in a_x of InP and a decrease in a_x of InGaAsP, the strain is accommodated in the appropriate manner. (Note: the strain accommodation within the grating region is not necessarily expected to be uniform throughout the entire 100 nm grating region depth, but the two materials are expected to experience an average equal and opposite change in strain, as is seen in the RSMs.) The parallel nature of both diffraction envelope shifts [white lines to guide the eye in Figure 4.7(c)] supports the occurrence of equal and opposite strain accommodation within the grating region. The exact position of the diffraction envelope shift maxima in Figure 4.7(c) are difficult to determine as a result of the grating-induced modulation of the diffraction pattern, however (400) RSMs provide additional information. The (400) RSMs indicate that the maxima corresponding to the average strain shifts are concentrated near the $\pm1^{st}$ order satellite reflections and are roughly midway between the InP and the InGaAsP Bragg peaks. The average change in strain can be calculated using

$$\Delta\varepsilon_z \sim -\Delta\theta_z \cot\theta_B \qquad \text{Eq. (4.1)}$$

where θ_B is the Bragg angle and $\Delta\theta_z$ is the angular distance of the shift with respect to the Bragg angle along Δq_z. (Details of the calculations may be found in Appendix A.) The strain modification caused by the

shift of the perpendicular lattice parameter (a_z) in the QT grating teeth is calculated from the (400) RSM and corresponds to $\Delta\varepsilon_z \sim 1.8\mathrm{x}10^{-3}$ for the InGaAsP (with respect to the InGaAsP epilayer Bragg peak); similarly, $\Delta\varepsilon_z \sim -2.5\mathrm{x}10^{-3}$ (with respect to the InP Bragg peak) for the InP material within the grating trenches. Using

$$\Delta\varepsilon_x \sim -\Delta\theta_x \cot\theta_B \qquad \text{Eq. (4.2)}$$

the approximate center of the InP diffraction envelope shift in Figure 4.7(c), located near the -1st satellite fringe, corresponds to a change in strain of $\Delta\varepsilon_x \sim 9.5\mathrm{x}10^{-4}$ (with respect to the InP Bragg peak) for the InP within the grating trenches. ($\Delta\theta_x$ is the angular separation of the diffraction envelope shift along Δq_x with respect to the Bragg peak.) A similar strain determination for the QT cannot be accomplished with the {422} RSM as the location of the envelope shift maximum is not as evident. However, from the parallel nature of the diffraction envelope shifts, $\Delta\varepsilon_x$ of the QT grating teeth will be close to $-9.5\mathrm{x}10^{-4}$. The equal and opposite accommodation of strain within the grating region, in both the x- and z-directions, strongly suggests the absence of any shift in a_y. {422} glancing exit RSMs, measured parallel to the rectangular gratings (x-rays incident along the y-direction), confirm no change in a_y with respect to the InP substrate, such that $\Delta\varepsilon_y \sim 0$. Thus, the material within the grating region, both InGaAsP and InP, experience an orthorhombic lattice distortion [108].

4.2.2 InGaAs(P) Overgrowth of InP Gratings

In addition to overgrowth of InGaAsP gratings, overgrowth of rectangular-patterned InP gratings ($d \sim 80$ nm, $w \sim 115$ nm) has also been investigated. Thin InGaAsP overlayers have been deposited on low temperature atomic hydrogen-cleaned InP gratings fabricated in (100) epi-ready InP wafers, with the y-direction oriented along $[0\overline{1}\overline{1}]$. Shown in Figure 4.9(a) is a (400) RSM of a ~ 210 nm $In_{(1-x)}Ga_xAs_yP_{(1-y)}$ ($x \sim 0.1, y \sim 0.29$) epi-layer grown on an unpatterned InP substrate. This sample was simultaneously grown alongside a patterned surface overgrowth to provide an experimental control, and therefore the surface was also low temperature atomic hydrogen-cleaned. The RSM depicts a high quality InGaAsP overlayer in which the position of the overlayer peak (position ~[0,-30] μm^{-1}) corresponds to a distance of 600 arcseconds from the InP substrate peak (position ~[0,0] μm^{-1}). Additionally, the presence of Pendellösung fringes between the InP and the InGaAsP peaks and minimal diffuse scattering in the vicinity of both the InP and InGaAsP peaks indicate the high structural quality of the material.

The (400) TAD measurement of a low temperature atomic hydrogen-cleaned patterned surface overgrowth is shown in Figure 4.9(b) [a SEM of grating is shown in Figure 3.6(a)]. Both the ~210 nm $In_{(1-x)}Ga_xAs_yP_{(1-y)}$ ($x \sim 0.1, y \sim 0.29$) epilayer and the InP peaks are of similar intensity to those in Figure

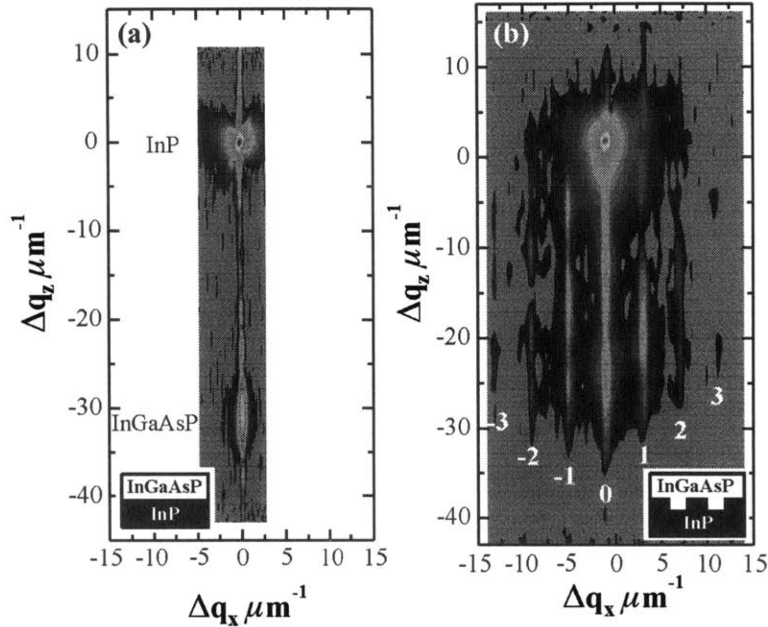

Figure 4.9 (a) (400) RSM of ~210 nm of InGaAsP deposited on a planar InP substrate. (b) (400) RSM of ~210 nm of InGaAsP deposited on rectangular-patterned InP gratings. Intensity scale is $1\text{-}1\times10^4$.

4.9(a). Satellite reflections are visible around the InGaAsP peak (position ~[0,-25] μm^{-1}) due to the InGaAsP residing within the grating trenches. Of particular interest is the fact that the $\pm 2^{nd}$ order satellite reflections are present around both the InGaAsP and InP (position ~[0,0] μm^{-1}) peaks. Although the grating is fabricated with a $w{:}L$ ratio of 1:2, the even order satellite fringes are apparent for the overgrown structure [they are not apparent in (400) RSMs of the bare InP grating (see Figure 3.6(b) and Figure 3.7)]. The presence of the $\pm 2^{nd}$ order satellite reflections from the rectangular grating (also present in {422} RSMs) suggests that, due to strain effects, the intensity of the 2nd order satellite reflection is no longer directly proportional to the 2nd Fourier coefficient of the grating profile. One speculation is that the InGaAsP within the grating trenches is slightly strained by the presence of the InP grating teeth, and the InP grating teeth are slightly strained by the presence of the InGaAsP in the grating trenches. Furthermore, evidence for strain within the grating region is apparent along $\Delta q_x = 0$ in Figure 4.9(b). Compared to the simultaneously grown planar structure, the grating overgrowth structure exhibits additional intensity roughly midway between the substrate and epilayer peaks, as seen in Figure 4.10.

One possible explanation for the additional intensity at roughly -230 arcsec in Figure 4.10 is distortion of the perpendicular lattice parameters, a_z, of both the InP grating teeth and the InGaAsP material in the grating trenches. The grating teeth and epitaxially filled-in trenches are of the same width, and would be

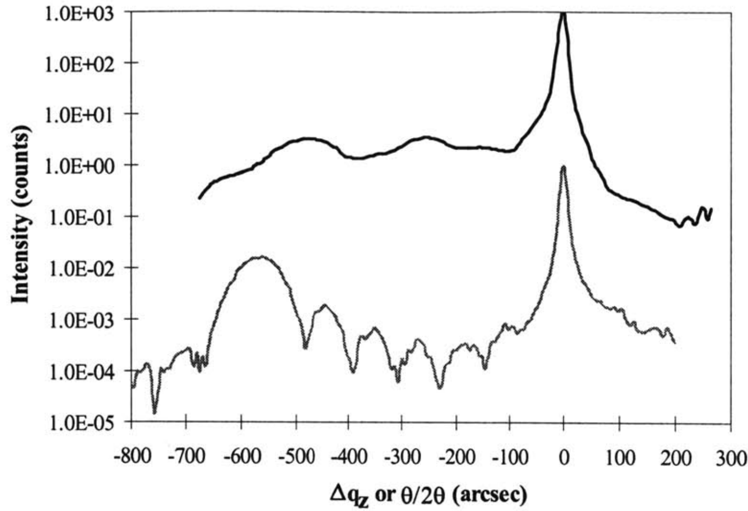

Figure 4.10 $\Delta q_x = 0$ scans (θ/2θ scans) of the planar sample (from Figure 4.9(a), gray line) and of the grating overgrowth sample (from Figure 4.9(b), black line). Data is offset for clarity.

expected to distort each other by a similar amount (if the elastic properties of the two component are similar, as is the case here) and produce a layer whose average strain is intermediate between the substrate and biaxially strained InGaAsP. (400) dynamical diffraction simulations have been performed using a simple three-layer model, including the substrate, a distorted ~80 nm layer (simulating the grating region), and a ~100 nm InGaAsP layer. The simple model is not an exact match to the real system, but the similarity between the calculated spectra and the experimental data support the speculation that the grating region exhibits a strain consistent with an in-plane compliance between InP and InGaAsP in the *z*-direction.

Similar to the (400) RSM of a hydrogen-cleaned InP grating in [Figure 3.6(b)], the separation of the satellite reflections in Figure 4.9(b) correspond to ~131 arcsec, and translates to a grating period of ~230 nm. Additionally, there is no evidence of horizontal splitting of the satellite reflections that would indicate degradation, or tapering, of the grating profile [58].

Figure 4.11 depicts a {422} glancing exit RSM of the same ~210 nm $In_{(1-x)}Ga_xAs_yP_{(1-y)}$ ($x \sim 0.1$, $y \sim 0.29$) overlayer on an InP rectangular-patterned grating; $\Delta q_x > 0$ corresponds to an increase in a_x. Due to the in-plane periodicity of the InGaAsP material deposited in the grating trenches, satellite reflections are observable about both the InP ($\Delta q_x \sim 0\ \mu m^{-1}$, $\Delta q_z \sim 0\ \mu m^{-1}$) and InGaAsP ($\Delta q_x \sim 0\ \mu m^{-1}$, $\Delta q_z \sim -25\ \mu m^{-1}$) Bragg diffraction peaks. Simulations of rectangular-shaped gratings indicate that the even order satellite reflections will appear with slight alteration of the toothwidth, however they will be less intense than the odd order reflections. In Figure 4.11, the $\pm 2^{nd}$ order satellite reflections are more intense

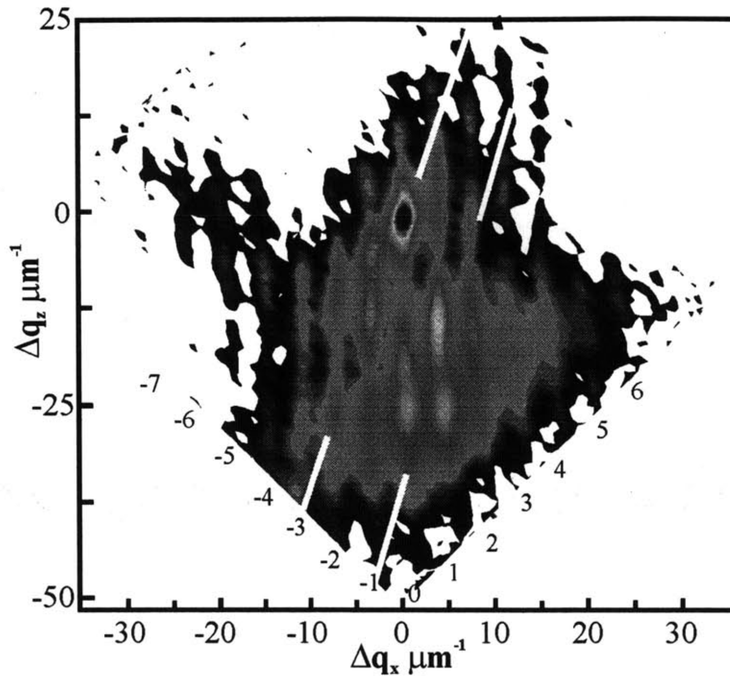

Figure 4.11 {422} RSM of ~210 nm of InGaAsP deposited on rectangular-patterned InP gratings. The white lines indicate diffraction envelope shifts. The intensity scale is 1-1x10^4.

than the ±3rd order reflections. The additional intensity is attributed to the presence of strain within the overgrown structure since the continuity of the satellite reflections about the Bragg peaks [more clearly seen in Figure 4.9(b)] indicates that the grating profile retains the rectangular shape. Similar to that observed in Figure 4.7(c), the diffraction envelopes (see white lines in Figure 4.11) of both materials shift in order to accommodate the strain within the grating region, as is evidenced by significant intensity within the ±1st order satellite fringes. However, in Figure 4.11, the features are broader and traverse multiple satellite reflections since the InGaAsP overlayer is much thinner (~210 nm) [thus the grating region is a larger percentage of the overall structure] than the sample discussed in Section 4.2.1 (InP overlayer thickness ~1 µm). As expected, the average of the InP diffraction envelope shift ($\Delta q_x \sim -3.5$ µm^{-1}, $\Delta q_z \sim -12.5$ µm^{-1}) corresponds to an average decrease in a_x and an average increase in a_z in order to accommodate the compressively strained InGaAsP. The associated average change in strain of the InP grating teeth, calculated from the RSM using Eq. (4.1) and Eq. (4.2), are $\Delta\varepsilon_x \sim -7.3\text{x}10^{-4}$ and $\Delta\varepsilon_z \sim 2.0\text{x}10^{-3}$, with respect to the InP Bragg peak. Similarly, the average InGaAsP diffraction envelope shift ($\Delta q_x \sim 5$ µm^{-1}, $\Delta q_z \sim -14$ µm^{-1}, Δq_x slightly larger than the location of the +1st order fringe) corresponds to an average increase in a_x and an average decrease in a_z; the calculated average change in

strain of the trench material is $\Delta\varepsilon_x \sim 5.7\text{x}10^{-4}$ and $\Delta\varepsilon_z \sim -1.6\text{x}10^{-3}$ with respect to the InGaAsP overlayer Bragg peak. The approximately parallel nature of both envelope shifts (white lines in Figure 4.11) further suggests an equal and opposite strain accommodation between the InP and InGaAsP within the grating region. A TAD-generated {422} glancing incidence RSM of the same sample is depicted in Figure 4.12,

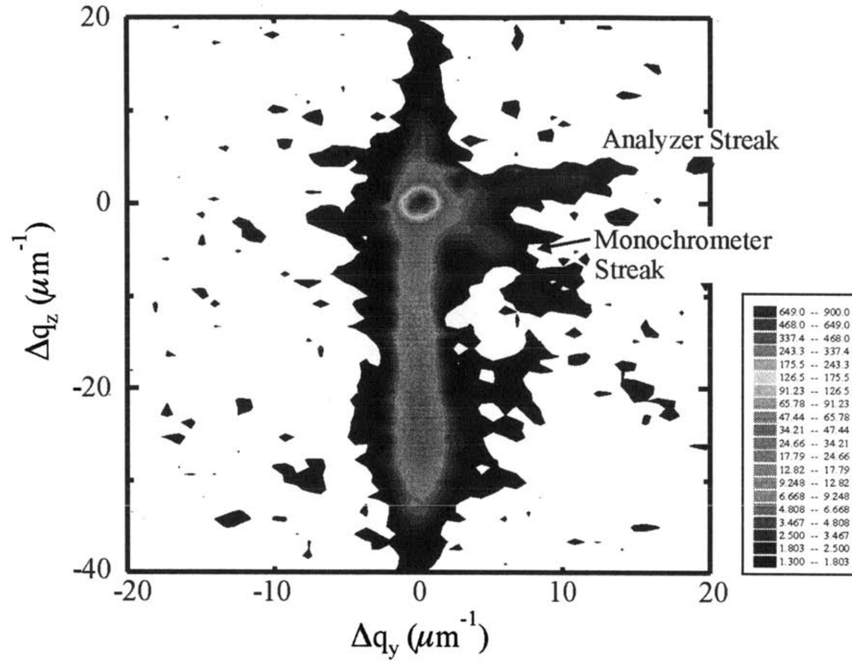

Figure 4.12 Glancing incidence {422} RSM of ~210 nm of InGaAsP deposited on an InP rectangular-patterned grating. The x-rays are incident parallel to the surface corrugation. The analyzer and monochrometer streaks are a function of the TAD measurement setup [57]. Both streaks are apparent due to the dispersive arrangement of the TAD system during this measurement.

with the x-rays incident parallel to the surface corrugation (x-rays along the *y*-direction, see Figure 4.5). No variation in a_y of the InGaAsP overlayer from that of InP is revealed, and thus the strain in the *y*-direction is the same as that of the planar epilayer, $\Delta\varepsilon_y \sim 0$. Hence, the strain accommodation within the grating region is exhibited as equal and opposite orthorhombic distortions of the crystal lattice [108]. As the QT material is initially deposited, the a_x and a_y lattice parameters are primarily influenced by the bulk InP substrate. As layer growth proceeds, a variation in a_z is expected, with an accompanying variation in a_x, since the QT is not perfectly lattice-matched to InP. Additionally, because the InP and the QT are mechanically similar materials, it is expected that they will accommodate the lattice mismatch elastically. The variation in a_z for the strained InP grating teeth ($-3.6\ \mu\text{m}^{-1} < \Delta q_x < -14\ \mu\text{m}^{-1}$) is observed in the -1st order satellite fringe, whereas the variation in a_x is not observable due to modulation of the intensity along

Δq_x originating from the grating; similar variations in a_z are also apparent in Figure 4.11 for the QT overlayer. Although the analysis of the RSMs suggests that manipulation of the QT overlayer is strictly due to strain, the QT material is deposited on a corrugated surface making compositional modulation possible.

4.2.3 Compositional Modulation in InGaAs(P) Overlayers

InGaAs Overlayers

To examine the possibility of compositional modulation, InGaAs deposited on rectangular-patterned InP substrates is investigated as these overlayers are more likely to exhibit compositional modulation due to the large concentrations of Ga and As [16]. As is apparent in SEM images of InGaAs deposited on InP rectangular-patterned gratings [see Figure 3.9(b)], the surface of ~200 nm of $In_{(1-x)}Ga_xAs$ ($x \sim 0.47$) is cusped, similar to that observed by Mullan, *et al* [82] for $In_{(1-x)}Ga_xAs$ ($x \sim 0.47$) overlayers deposited on (100) InP sawtooth-patterned substrates with (311)A facets (in which composition modulation was present). Figure 4.13(a) shows the (400) High Resolution Double Axis X-ray Diffraction (HRDAXD) analysis of ~200 nm of InGaAs ($x \sim 0.47$) on preserved rectangular-patterned InP gratings. Data from the simultaneously grown planar monitor sample is displayed in gray for comparison, and confirms the $In_{(1-x)}Ga_xAs$ composition of $x \sim 0.47$. The data from the InGaAs overlayer on the rectangular-patterned grating [black curve in Figure 4.13(a)] exhibits additional features, namely a distinct peak at $\theta/2\theta \sim$ -600 arcsec and an extremely broad tensile-strained peak. At first glance, the rather strong compressive-strained feature at -600 arcsec may appear to originate from an $In_{(1-x)}Ga_xAs$ layer with $x \neq 0.47$ deposited on the rectangular-patterned substrate; from x-ray simulations this would correspond to an average Ga composition of 43%. However, photoluminescence (PL) measurements do not confirm the presence of a Ga-deficient $In_{(1-x)}Ga_xAs$ ($x \sim 0.43$) overlayer which is expected to luminesce at $\lambda \sim 1.57$ μm (at 10K). The PL spectrum shown in Figure 4.14 exhibits two features; a symmetric narrow peak at $\lambda \sim 1.55$ μm (FWHM ~ 17 meV) and a broad peak centered at $\lambda \sim 1.74$ μm (FWHM ~ 52 meV). Furthermore, assuming the Ga composition obtained from the planar monitor sample (Ga ~ 47%) and a compressive strain equivalent to ~ -600 arcsec, a PL emission of $\lambda \sim 1.49$ μm is expected, but also not observed. (Note: the PL feature at $\lambda \sim 1.55$ μm is not speculated to be due to spinodal-like compositional modulation. The FWHM of the ~1.55 μm signal is narrower than a similar feature present in the planar monitor sample (~28 meV). Furthermore, compositional modulation due to the surface corrugation is expected to dominate miscibility gap-induced compositional modulation.) Since the PL features do not readily correlate to that predicted via x-ray diffraction, the possibility of compositional modulation must be considered.

Similar to the model proposed for sawtooth-patterned overgrowth (Figure 4.4), a model for the overgrowth of rectangular-patterned surfaces was developed and is depicted in Figure 4.15. From marker

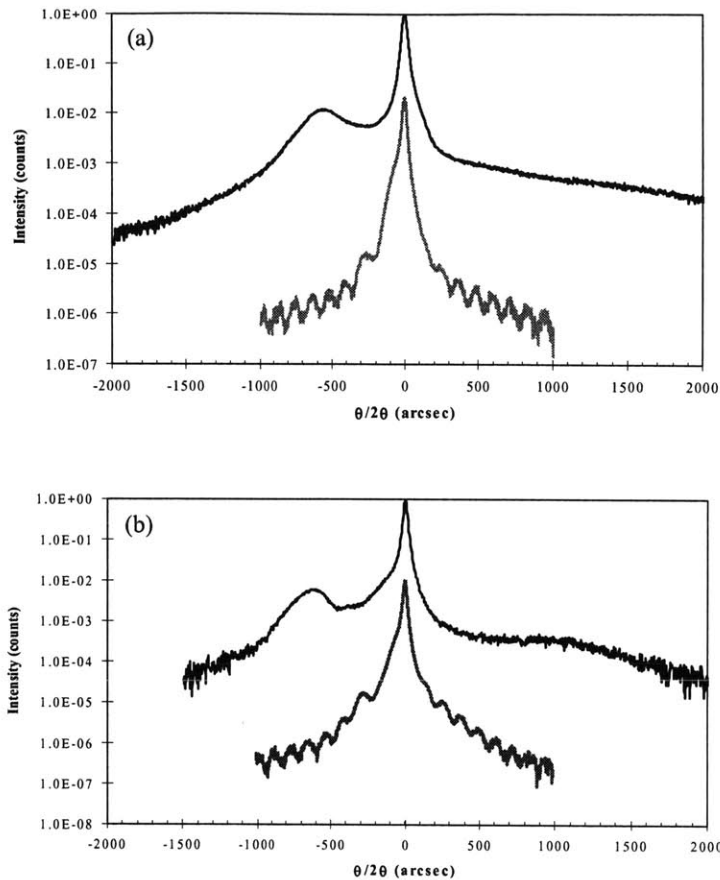

Figure 4.13 (a) HRDAXD of ~200 nm of InGaAs deposited on a preserved rectangular-patterned InP grating (black curve). The gray curve is data obtained from the simultaneously grown planar monitor sample. A SEM of the sample is depicted in Figure 3.9(b). (b) HRDAXD data from ~200 nm of InGaAs deposited on a slightly altered rectangular-patterned InP surface. A SEM of the sample is depicted in Figure 3.9(a). The gray curve is data obtained from the simultaneously grown planar monitor sample.

layer overgrowth studies by Izrael, *et al* of InP rectangular-patterned surfaces [66], as the overlayer material is deposited in the trenches, facets begin to develop between the (100) growth front (dictated by the trench base) and the (110) grating tooth sidewalls; these facets appear to be similar to $\{h11\}$ facets, and will most likely not be preferred incorporation sites for Ga adatoms. Thus the Ga adatoms will tend to migrate towards the center of the trench or the top of the grating teeth. (Note, the model in Figure 4.15 assumes preservation of the rectangular grating profile and (100) trench and tooth surfaces.) Although in reference to GaAs/AlGaAs quantum wire formation in sawtooth-type corrugations, the analytical model developed by Biasiol and Kapon also predicts the formation of $\{h11\}$-type facets within (100) grating

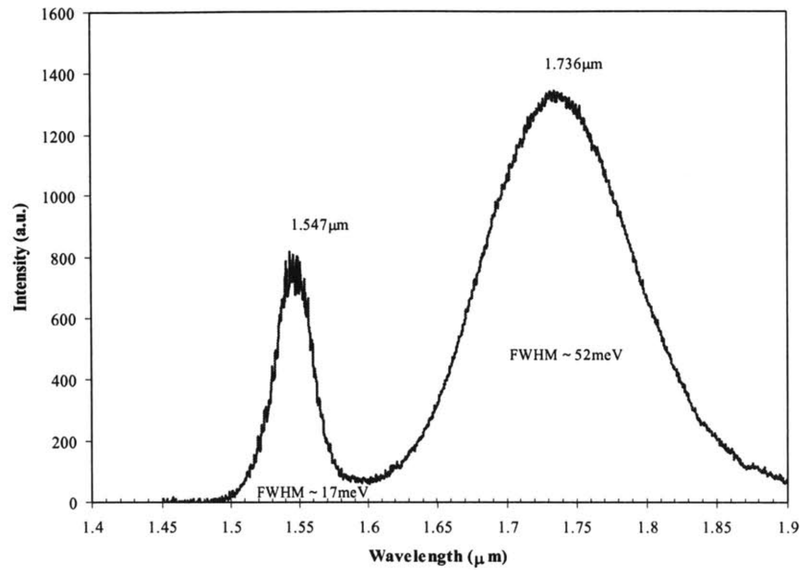

Figure 4.14 10K PL spectrum of ~200 nm InGaAs deposited on a preserved InP rectangular-patterned grating. See Figure 3.6(b) for a cross-sectional SEM of the sample.

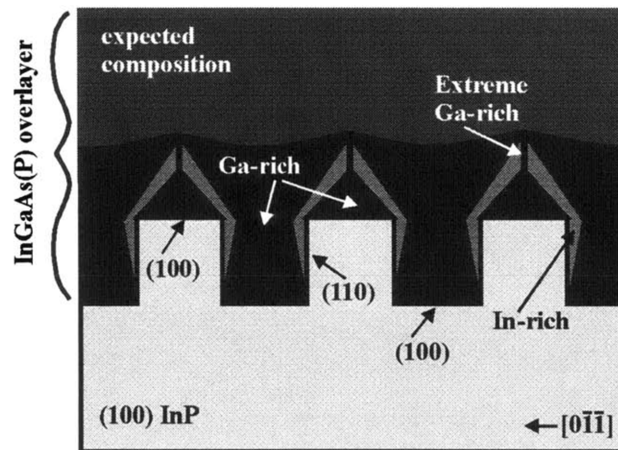

Figure 4.15 Schematic illustration of the overgrowth process of InGaAs(P) on rectangular-patterned (100) InP surfaces.

grooves [89]. Similar to the sawtooth-patterned overgrowth, a 'triangular-shaped region' of Ga-rich material is also expected on top of the grating teeth (as a result of deposition on a mesa-like profile). The localization of Ga adatoms will result in Ga-deficient regions that correspond to the non-(100) growth fronts. The occurrence of an extremely Ga-rich column above the 'triangular-shaped region' would also not

be unexpected, and the thickness would depend on the planarization rate of the Ga-rich region within the grating trenches. As the surface of the overlayer begins to planarize, the Ga adatoms will incorporate more readily on surfaces that approach a (100) orientation, and the overlayer composition will become the same as that of a planar epilayer. As with sawtooth-patterned overgrowth, the thickness required to achieve a planar overlayer will decrease as the concentration of Ga and As is decreased; this is evident from the cusped surface of a ~200 nm InGaAs overlayer [Figure 3.9(b)] compared to a planar surface of a ~210 nm $In_{(1-x)}Ga_xAs_yP_{(1-y)}$ ($x \sim 0.1$, $y \sim 0.29$) overlayer, both deposited on preserved rectangular-patterned InP substrates.

From the analysis of strain accommodation in the grating region of InP overlayers on InGaAsP gratings, and from an expectation of compositional modulation, the x-ray peak at ~ -600 arcsec in Figure 4.13(a) is thought to be due to strain present within the InP teeth, such that a_z is increased relative to bulk InP ($\Delta\varepsilon_z \sim 4.6\text{x}10^{-3}$). Assuming an equal and opposite strain behavior in the adjacent $In_{(1-x)}Ga_xAs$ ($x \sim 0.47$) trench, such that InGaAs is tensile-strained to ~ 600 arcsec, a PL feature at $\lambda \sim 1.62$ μm (at 10K) is expected, but not observed. Therefore, the dominant PL feature observed at $\lambda \sim 1.74$ μm is attributed to an InGaAs composition that varies from the planar monitor sample (Ga ~ 47%) and is also shifted due to strain. The PL feature at $\lambda \sim 1.55$ μm is attributed to either the In-rich material adjacent to the grating teeth or the average InGaAs composition deposited beyond the location of the grating. For deposition of InGaAs on preserved InP gratings, the following overgrowth scenario is proposed: a Ga-deficient InGaAs layer is deposited adjacent to the InP grating teeth, while within the center of the trench and on top of the grating teeth Ga-rich InGaAs material is deposited. As growth proceeds, volumetric variations of the Ga-rich region (due to non-(100) growth fronts adjacent to the InP teeth) will most likely occur in conjunction with differing stress interactions between the InP grating teeth and the InGaAs material within the trenches. Additionally, as the volume of the Ga-rich region is varied, the composition may likewise be altered. Thus, a modulation of both the strain and composition of the Ga-rich material would give rise to the weak, broad tensile x-ray feature seen in Figure 4.13(a), and similarly the broad PL feature observed at $\lambda \sim 1.74$ μm. Dynamical diffraction simulations of Ga-rich InGaAs, at varying strains and compositions, support the reasoning for the broad x-ray feature.

The proposed Ga-rich and Ga-deficient regions are clearly dependent on the starting grating profile. In the case of Figure 3.9(a), in which the grating profile was modified via mass transport, the grating trench is no longer solely (100)-oriented. Thus, the InGaAs(P) overlayer might be expected to fill in the trenches in a manner similar to that seen in sawtooth-patterned overgrowth since the mass transport-altered trench contains inclined facets. The presence of pre-growth-defined non-(100) facets are speculated to result in a narrower and more uniform Ga-rich region coupled with a larger Ga-deficient region. The narrowness of

the Ga-rich region may effectively increase the growth rate in the grating trench (along the (100) growth front), thus the expectation of a more planar surface is not unreasonable, and is seen from the comparison of Figure 3.9(a) and (b). Although the mass transport-modified profile may seem preferable in terms of planarity, the anticipated increase in severity of composition modulation (as compared to the fully-preserved rectangular profile) would be more destructive to the resulting overlayer. (400) HRDAXD measurements shown in Figure 4.13(b) reveal a more clearly defined and narrower x-ray feature [compared to that depicted in Figure 4.13(a)] originating from the Ga-rich InGaAs material. Consequently, from the model in Figure 4.15 and knowledge of inclined facet overgrowth, more severe compositional modulation is expected within altered rectangular profile overgrowth.

InGaAsP Overlayers

Given the submicron rectangular-patterned overgrowth model in Figure 4.15, the existence of compositional modulation within a ~210 nm InGaAsP overlayer (i.e. Figure 4.11) is probable. Room temperature PL measurements disclose a difference in the InGaAsP emission wavelength between the planar monitor sample ($\lambda \sim 1.095$ μm) and the grating overgrowth sample ($\lambda \sim 1.083$ μm). Furthermore, the large range of Δq_x (-11 μm^{-1} $< \Delta q_x <$ 8 μm^{-1}) as well as the range of Δq_z (~ -34 μm^{-1} $< \Delta q_z <$ ~ -20 μm^{-1}) in Figure 4.11 of the InGaAsP overlayer may be suggestive of compositional modulation and/ or variation in a_x and a_z. However, from work reported for sawtooth-patterned overgrowth, the small amount of Ga and As within the InGaAsP ($x \sim 0.1, y \sim 0.29$) overlayer would result in minor compositional modulation. Also, with such a thin overlayer (~ 210 nm) the grating region (~80 nm) occupies roughly half the total overlayer thickness. Thus, any variation in lattice parameters (not necessarily expected to be constant throughout the grating region), due to strain accommodation in the grating region, would comprise a large portion of the overlayer and be detectable via asymmetric x-ray diffraction measurements.

Initial analysis of the PL and TAD data suggests a difference in the InGaAsP overlayer composition with respect to that measured from the planar monitor sample. Using the observed PL emission wavelength for the InGaAsP bandgap, (400) HRDAXD dynamical diffraction simulations indicate a decrease in mole fraction of both Ga and As for the overlayer. However, a decrease in the Ga mole fraction is not expected if the overgrowth model in Figure 4.15 is assumed since the Ga-deficient region should be small due to the small concentration of Ga and As in the overlayer. Consequently, the difference in strain observed in the overgrowth sample ($\varepsilon_z \sim 3.6\text{x}10^{-3}$) relative to the planar monitor ($\varepsilon_z \sim 4.5\text{x}10^{-3}$), albeit small, can not be overlooked. From the {422} RSM in Figure 4.11, the changes in strain of the overlayer, with respect to the planar $In_{(1-x)}Ga_xAs_yP_{(1-y)}$ ($x \sim 0.1$, $y \sim 0.29$) epilayer, are calculated to be $\Delta\varepsilon_x \sim 5.2\text{x}10^{-4}$ and $\Delta\varepsilon_z \sim -9.0\text{x}10^{-4}$ (recall that a_y is equal to the in-plane lattice constant of InP, so $\Delta\varepsilon_y \sim 0$). Thus, the

overlayer material above the grating region also experiences an orthorhombic lattice distortion. Taking into account the reduced strain in both a_z and a_x, the following equation is used to calculate the expected modification to the bandgap,

$$\Delta E_g = a(\Delta\varepsilon_x\sqrt{2} + \Delta\varepsilon_z) - b\sqrt{\left(\frac{\Delta\varepsilon_x}{2} - \Delta\varepsilon_z\right)^2 + d^2\left(\frac{\Delta\varepsilon_x}{\sqrt{2}}\right)^2} \qquad \text{Eq. (4.3)}$$

where a is the hydrostatic deformation potential and b and d are the shear deformation potentials [109,108]. For a strained $In_{(1-x)}Ga_xAs_yP_{(1-y)}$ ($x \sim 0.1$, $y \sim 0.29$) overlayer, Eq. (4.3) predicts a room temperature PL emission of $\lambda \sim 1.092$ μm. Considering the average change in strain (with respect to the planar epilayer) of the QT material within the grating trenches, bandgap calculations suggest a 300K PL emission of $\lambda \sim 1.083$ μm. Shown in Figure 4.16 are 300K PL spectra from both the planar monitor sample

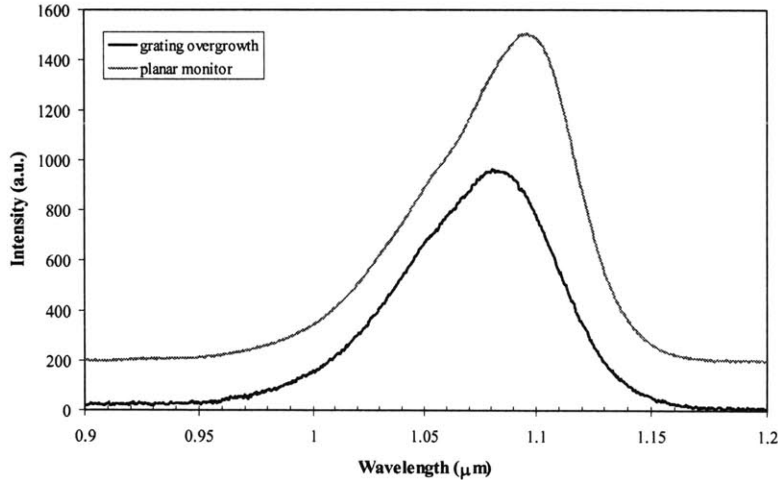

Figure 4.16 300K PL spectra of ~210 nm of InGaAsP deposited on a preserved InP grating (black line) and the simultaneously grown monitor sample (gray line).

(gray line) and the grating overgrowth sample (black line). The PL spectrum from the grating overgrowth sample exhibits a single broad feature peaked at $\lambda \sim 1.083$ μm, and clearly encompasses emission originating from the QT in both the grating trenches and beyond the grating region. (Similar modifications to the bandgap of InGaAs/GaAs buried quantum wires have also been observed [108].) Therefore, the orthorhombic lattice distortion and change in bandgap of the QT material may be attributed to strain in the overlayer caused by the InP grating, rather than to compositional modulation. Stress exerted on the overlayer above the grating region is not surprising since the overlayer is only roughly twice the thickness

of the grating region. As the overlayer thickness is increased, such that the grating region is only a fraction of the overlayer thickness, the orthorhombic distortion of the overlayer will decrease; e.g. no strain modification of the overlayer above the grating region is observed in structures with ~1 μm of InP deposited on InGaAsP gratings (Section 4.2.1). Strain variation on the order of 10^{-3} and less and bandgap modifications on the order of 10 meV and lower (with respect to the planar sample) due to the orthorhombic strain of the QT overlayer are minor alterations and will most likely not have a pronounced effect on devices incorporating buried rectangular-patterned gratings.

Additional analysis of the overgrown grating structure, via x-ray topography, reveals no sign of misfit dislocations. Shown in Figure 4.17 is (a) an x-ray topograph of ~210 nm of InGaAsP deposited on a planar

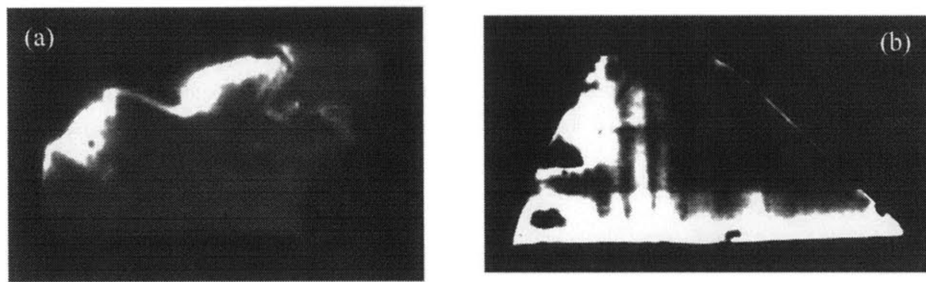

Figure 4.17 (a) X-ray topography measurement of ~210 nm of InGaAsP deposited on an InP rectangular-patterned grating. The absence of distinct features suggests material of good quality having a low defect density. (b) X-ray topography measurement of InGaAs deposited on an InP substrate. The distinctive lines indicate the presence of misfit dislocations.

InP grating (sample analyzed in Figure 4.11), and (b) an x-ray topograph of InGaAs deposited on an InP substrate. The sample in Figure 4.17(b) reveals the presence of misfit dislocations at the substrate-epitaxial layer interface. An additional indication of the quality of the ~210 nm InGaAsP overlayer is provided via Scanning Transmission Electron Microscopy (STEM) measurements of the simultaneously grown planar sample, shown in Figure 4.18. The InGaAsP-InP interface appears to be devoid of defects and of high quality.

Depicted in Figure 4.19 is a TAD-generated {311} glancing exit RSM of ~200 nm of $In_{(1-x)}Ga_xAs_yP_{(1-y)}$ ($x \sim 0.12$, $y \sim 0.3$) deposited on a rectangular-patterned InP substrate. The planar epilayer exhibits a strain of $\varepsilon_z \sim 2.5\text{x}10^{-3}$, whereas the InGaAsP overlayer exhibits a strain of $\varepsilon_z \sim 1.9\text{x}10^{-3}$. As the strain is roughly half that of the sample in Figure 4.11, the features apparent in the {311} RSM strongly overlap, complicating the investigation of the overgrown structure. (400) RSMs reveal information about the perpendicular strain present in the overlayer, however specific information

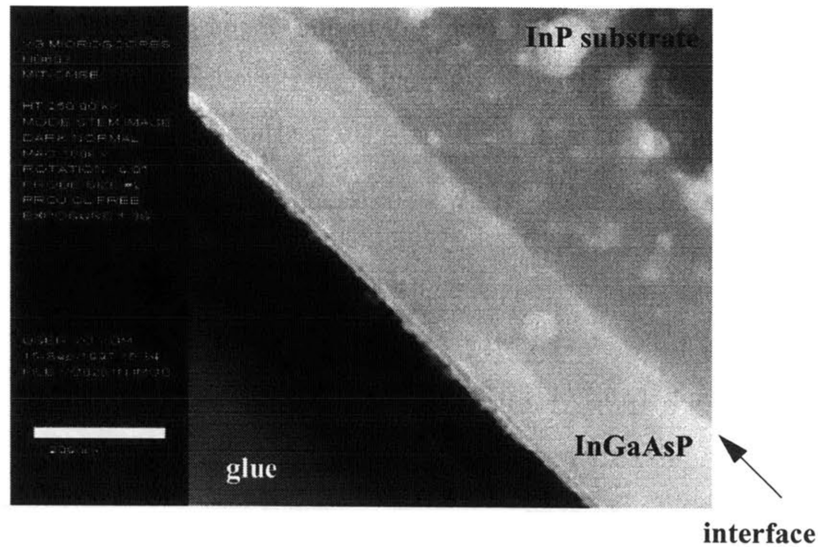

Figure 4.18 Scanning transmission electron microscopy measurement of the sample analyzed in Figure 4.9(a); ~210 nm of InGaAsP deposited on an InP substrate.

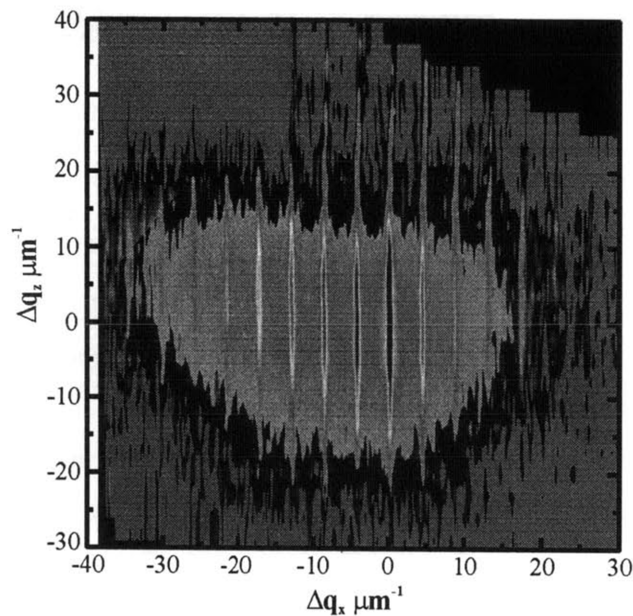

Figure 4.19 TAD-generated {311} glancing exit RSM of $In_{(1-x)}Ga_xAs_yP_{(1-y)}$ ($x \sim 0.12$, $y \sim 0.3$) overlayer on a rectangular-patterned InP grating. RSM intensity scale is 1-2.5x10^3.

concerning the envelope shifts is not attainable. The (400) RSM shown in Figure 4.20 contains an average strain feature located roughly midway between the InP (~[0,0] μm^{-1}) and InGaAsP (~ [0,-13] μm^{-1}) Bragg peaks suggesting compliant behavior within the grating region. Additionally, the uniformity of the

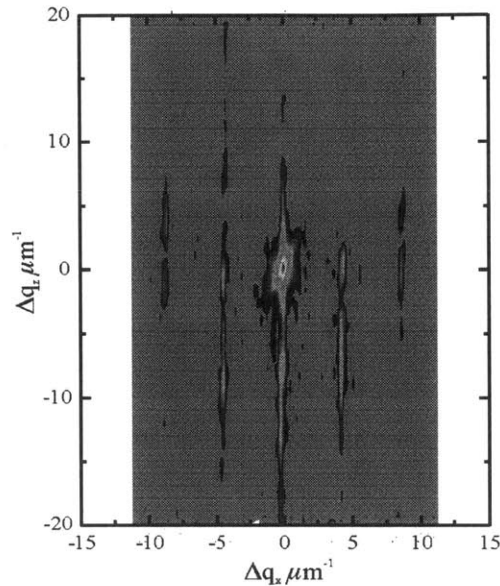

Figure 4.20 TAD-generated (400) RSM of $In_{(1-x)}Ga_xAs_yP_{(1-y)}$ ($x \sim 0.12$, $y \sim 0.3$) overlayer on a rectangular-patterned InP grating. RSM intensity scale is 1-1x10^4.

satellite reflections reveals the presence of vertical sidewall gratings, confirming the preservation of the rectangular grating profile. PL measurements of both the simultaneously-grown planar monitor sample and the grating overgrowth sample reveal a slight increase in bandgap of the grating overlayer. The bandgap alteration is comparable to that observed in the grating sample of Figure 4.11, and is also attributed to minor orthorhombic lattice distortion of the thin InGaAsP material as a result of the buried InP grating.

4.2.4 Grating Fabrication Issues and the Effects on Overlayer Quality

Although the overgrowth of rectangular-patterned corrugations appears to be better suited for buried index contrasts in which a specific index modulation is required, the overgrowth process is not without problems. Realization of smooth (100) facets in the grating trenches has proven to be a very difficult task. As the etch rates attained in an RIE process are dependent on the state of the plasma, so is the quality of the etched surface. For the surface corrugations fabricated (both InP and InGaAsP), an etch-stop layer was not utilized to rigorously define the corrugation depth; as a result, the surface of the trenches was more likely to be rough rather than smooth. Shown in Figure 4.21 is an extreme example of trench roughness observed in H_2:CH_4 RIE definition of rectangular-patterned gratings in InP. Furthermore, as a result of the shallow depths required for typical buried index contrasts (~100 nm), the quality of the resulting etched surface is a strong function of the initial stability of the plasma in the RIE chamber.

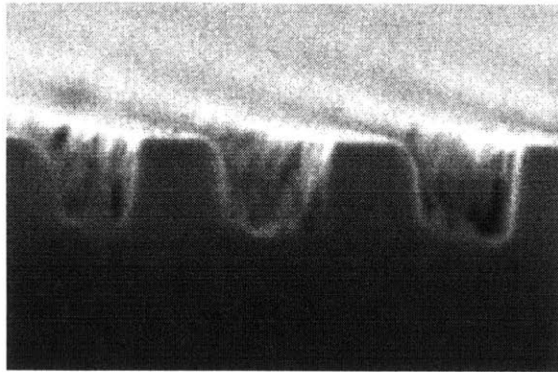

Figure 4.21 An extreme example of roughness in the grating trenches of ~230 nm period InP gratings fabricated via RIE.

Shown in Figure 4.22 is an example of an etched InGaAsP corrugation in which the resulting grating trenches are visibly rough. Akin to issues regarding sawtooth-patterned surface overgrowth, the quality of

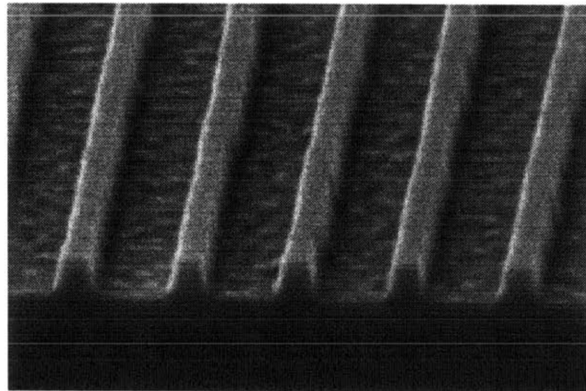

Figure 4.22 ~230 nm period gratings fabricated in an InGaAsP epilayer; gratings have been wet chemically etched for entry into the GSMBE system. The roughness apparent in the grating trenches detrimentally affects the quality of an InP overlayer.

the grating trenches strongly affects the quality of an overlayer. In fabrication of sawtooth corrugations, microfacets resulting from roughness at the edges of the masking material significantly degrades the quality of an overlayer [74]. The exposure of various microfacets severely complicates the overgrowth since atoms diffuse and incorporate differently depending on the exposed crystallographic plane. The existence of randomly oriented regions, or microfacets, as seen in the trenches of Figure 4.22 likewise detrimentally affects the quality of an overlayer. Depicted in Figure 4.23 is a (400) RSM of a ~275 nm InP overlayer deposited on the rectangular-patterned gratings shown in Figure 4.22. The diffuse scatter located

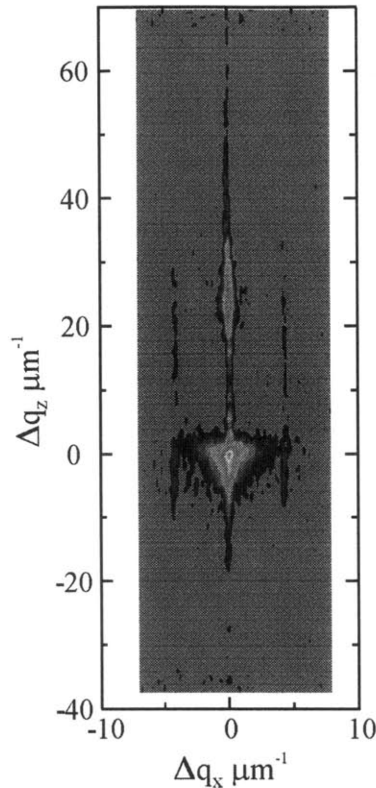

Figure 4.23 (400) RSM of ~275 nm InP deposited on the InGaAsP grating shown in Figure 4.22. Intensity scale is 1-1x10^4.

about the InP Bragg diffraction peak (~[0,0] µm^{-1}), and the resulting extension to the ±1st order fringes, suggests the degraded quality of the InP overlayer. Furthermore, the inability to resolve more than the ±1st order satellite reflections suggests the existence of destructive interference of the x-ray beam as it traverses the InP overlayer. Shown for comparison in Figure 4.24 is a SEM image of the InP gratings used for the InGaAsP overgrowth results reported in Section 4.2.2.

Proper removal of the etch mask following RIE is also crucial to realization of high quality overlayers. For the gratings fabricated at MIT, both SiO_2 and Ti were used as etch masks. In general, for gratings fabricated using a SiO_2 etch mask, the mask was easily removed following RIE via a buffered oxide etch (BOE). The use of Ti as an etch mask, however, proved to be more troublesome. As Ti is commonly used as an adherent for metallization layers in fabrication of many III-V devices (i.e. Ti-Pt-Au alloyed electrical contacts), it is rather difficult to completely remove from an InP surface. Shown in Figure 4.25 is a SEM of an InGaAsP grating with a thin layer of Ti remaining on top of the grating teeth. Figure 4.26 is a Nomarski interference contrast photograph of the surface of ~3.5 µm of InP deposited on a Ti-contaminated surface.

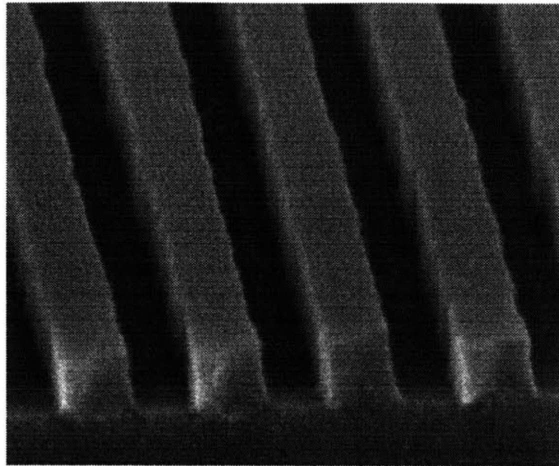

Figure 4.24 SEM image of the ~230 nm period InP gratings discussed in Section 4.2.2. The gratings have been degreased and wet chemically etched following RIE. Note the smoothness of the grating trenches.

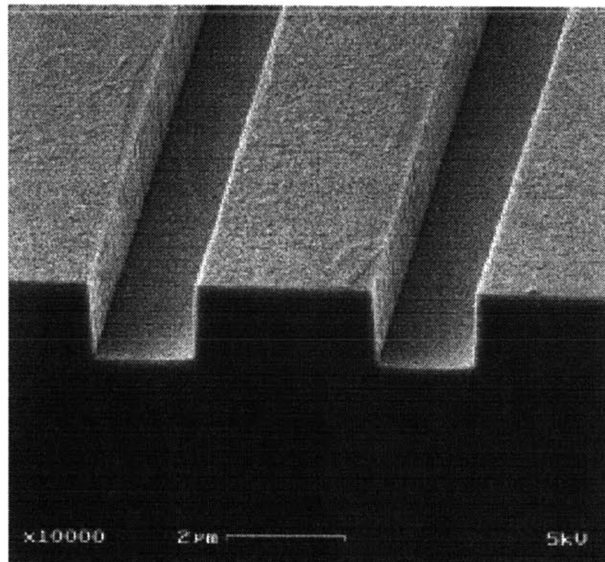

Figure 4.25 Scanning electron micrograph of InGaAsP gratings with a thin layer of the Ti etch mask remaining on the grating teeth.

Gratings similar to those depicted in Figure 4.25 were incorporated into a multiple quantum well DFB laser. Although the laser was functional, the threshold currents were quite high due to the both the presence of a thin Ti layer and the poor quality of subsequently deposited layers.

From the analysis of deposition on submicron rectangular-patterned surfaces, it is anticipated that rectangular profiles are better suited for realization of devices containing a buried index contrast. Although

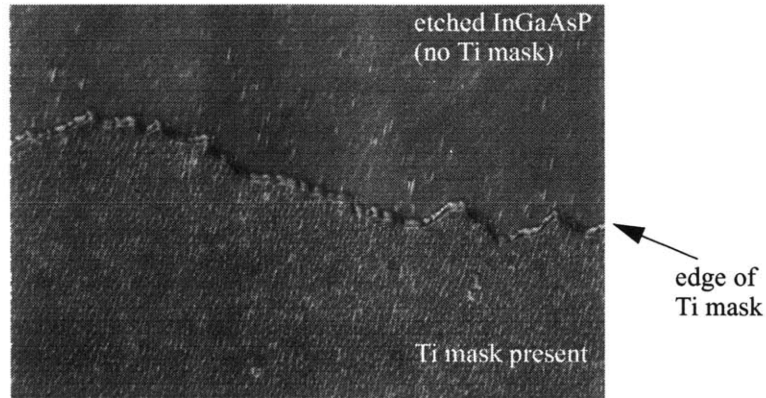

Figure 4.26 Normarski interference contrast microscopy image of ~3.5 μm of InP deposited on InGaAsP having a thin layer of the Ti etch mask on the InGaAsP surface (200x magnification). The rough edge apparent in the photo is the edge of the Ti mask. Vertical and horizontal striations are due to the printer.

compositional modulation is expected in layers with high concentrations of Ga and As, the magnitude of the modulation is believed to be less severe than deposition on sawtooth-patterned surfaces. Furthermore, even though fabrication of rectangular-patterned surfaces is not without problems, fabrication of sawtooth-patterned gratings is likewise difficult. However, unlike sawtooth corrugations, following successful fabrication of rectangular-patterned gratings no further modification of the profile is required for realization of high quality overlayers.

4.3 Patterned Surface Overgrowth Models

Various analytical models have been developed for the overgrowth of submicron patterned surfaces [i.e. 89, 110], stemming in large part from the analysis of mass transport effects. The models encompass gradients of the surface energy, or chemical potential, due to the patterned surface. For the model developed by Biasol and Kapon [89], the growth rate variation is attributed to "capillarity", or diffusion of atoms from convex surfaces to concave surfaces. Specifically, derivation of growth rates on each facet (grating trench facet, grating tooth facet, and grating sidewall facet) result in

$$r_t = r_t^0 - \frac{C}{l_t^3} \qquad \text{Eq. (4.4)}$$

$$r_s = r_s^0 \qquad \text{Eq. (4.5)}$$

$$r_b = r_b^{\ 0} + \frac{C}{l_b^{\ 3}} \qquad \text{Eq. (4.6)}$$

where r is the growth rate, r_0 is the growth rate in the absence of capillarity, l is the lateral width of the grating tooth (t) and grating trench (b), and

$$C = \frac{2\Omega_0 L_s^2 \gamma}{k_B T} \qquad \text{Eq. (4.7)}$$

in which L_s is the diffusion length, Ω_0 is the atomic volume, γ is the surface energy, k_B is Boltzman's constant, and T is the sample temperature [89]. The surface energy is a function of the surface curvature, and is defined as $\gamma = 2(\gamma_s \csc\theta - \gamma_{b,t} \cot\theta)$, where s, b, and t signify the sidewall, grating base, and grating tooth top, respectively, and θ is the sidewall angle with respect to horizontal. The addition of the constant C to the growth rate accounts for the diffusion of atoms from the top of the grating tooth to the base of the grating trench. Also inherent in this parameter is the sample temperature dependence of the diffusion length. Using this model, Biasol and Kapon have predicted a "self-limiting" profile for layer deposition on both rectangular and trapezoidal surface features (see Figure 4.27 for schematic of overlayer deposited on

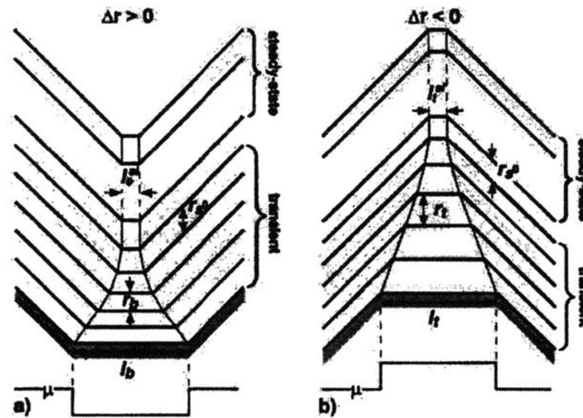

Figure 4.27 Schematic of deposition in rectangular trenches and on mesas as determined via the numerical model developed by Biasol and Kapon. Figure from [89]. The *sl* superscripts represent the self-limiting widths; $\Delta r = r_s - r_b$.

a rectangular surface). The "self-limiting" growth occurs for a grating sidewall growth rate, r_s, less than the growth rate on either the grating tooth, r_t, or in the grating base, r_b. Realization of a self-limited growth

regime is beneficial for the fabrication of quantum wire devices. With respect to overgrowth of rectangular-patterned gratings, although Biasol and Kapon deal with independent features (i.e. either a trench or a groove), the initial prediction that a triangular-type region is formed on a rectangular-shaped mesa is similar both to that observed in sawtooth-patterned overgrowth and predicted by the model presented in Section 4.2.3.

Although Biasol and Kapon predict the resulting overgrowth profiles and self-limited regions, the equations presented in [89] [Eq. (4.2)-Eq. (4.4)] are not completely accurate. Calculation of the diffusion-enhanced growth rate, $\Delta r = C/l^3$, generates a unitless number. Furthermore, the model assumes the diffusion length (or capillarity) is the only variable, and does not take into account desorption of the group III atoms. Because desorption is not included in the model, and the growth rate along the sidewall is fixed [Eq. (4.3)], all incident group III atoms must incorporate into the growing layer. Hence, as described by Eq. (4.2) and Eq. (4.4), to satisfy conservation of mass, $l_t = l_b$; if the grating tooth width and trench width are not equal, Eq. (4.2) and Eq. (4.4) are invalid.

Investigation of the surface energy equation presented in [89], $\gamma = 2(\gamma_s \csc\theta - \gamma_{b,t} \cot\theta)$, reveals that the surface energy, and subsequently C, near infinity as the grating profile approaches a planar surface (i.e. θ approaches 0). Thus, according to the model, for shallow-angled gratings, material deposition is dominated by growth within the grating trench, and the growth rates of the trench and tooth are predicted to be drastically different. Recall, the model assumes a constant growth rate on the grating sidewalls [Eq. (4.3)]. From experimental observations of submicron sawtooth-patterned overgrowth, the rate of deposition along grating sidewalls for single overlayers is not constant throughout the layer deposition [74]. The growth rate on $\{h11\}$-type surfaces is dependent on the type of growth front present in the grating trench; e.g. a (100) growth front will dominate $\{h11\}$-type growth fronts [74]. Thus, the model presented by Biasol and Kapon will not accurately predict the progression of thick overlayers deposited on submicron patterned surfaces, or deposition on 'smoothed' grating profiles.

The basis of the analytical model developed by Ohtsuka [110] for patterned surface overgrowth is the resident lifetime of a group III atom on the growing surface. The resident time of an atom is crystal orientation-dependent, and is thus an alternate way of describing "capillarity". Specifically, the resident lifetime of an atom increases as the crystal plane is transformed from a (100)-type surface to a (011)-type surface. Calculations of the Ga diffusion length by Ohtsuka are shown in Figure 4.28.

Like Biasol and Kapon, Ohtsuka performed calculations for independent features (i.e. either a ridge or a groove). For a 0.5 μm wide mesa with (011) sidewalls, calculations show a 'triangular-shaped region' on the mesa top, and a narrow, much slower growing $\{h11\}$ region adjacent to the mesa sidewalls and the

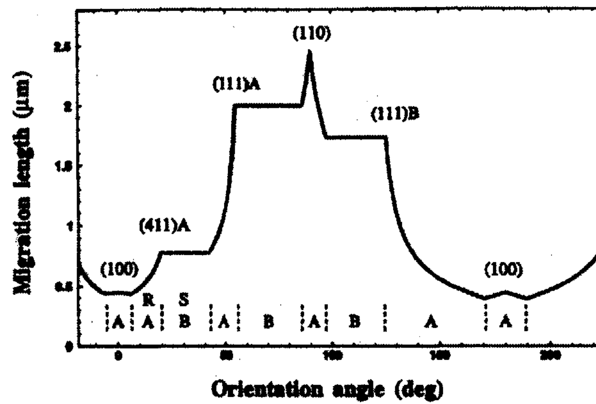

Figure 4.28 Calculation of the variation in the Ga diffusion length for different surface orientations. Figure from [110].

edges of the 'triangular-shaped region' (see Figure 4.29) [110]. For GaAs growth on GaAs-patterned

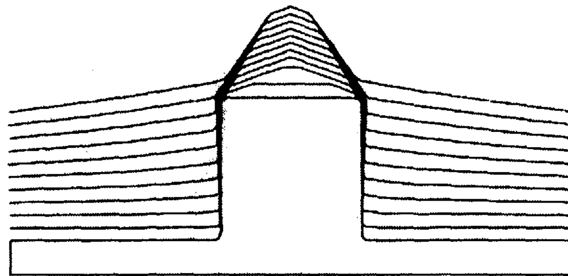

Figure 4.29 Schematic of GaAs deposition on a 0.5 μm GaAs rectangular mesa as determined via the numerical model developed by Ohtsuka. Figure from [110].

substrates, as modeled by Ohtsuka, the narrow $\{h11\}$-type regions will be comprised of uniform GaAs material. However, with the addition of a group III atom having a shorter diffusion length, e.g. aluminum, the composition of the $\{h11\}$-type regions will be altered.

The parameters varied by Ohtsuka for calculation of the resulting overlayer profile were the resident time and sticking coefficient "for each faceted surface orientation such that the simulated growth evolutions agree to the observed features of GaAs growth" [110]. Thus, similar to the model developed by Biasol and Kapon, the mathematical parameters are varied until the result is similar to that which is observed experimentally.

The model presented in Section 4.2.3 for InGaAsP overgrowth of submicron rectangular-patterned InP gratings takes into account the same parameters manipulated by both Biasol and Kapon, and Ohtsuka. The

rectangular grating overgrowth model is based on numerous experimental observations (via an extensive literature review) of the migration behavior of the group III atoms. Experimental observations of the diffusion lengths encompasses the group III residence time as well as the probability of incorporation in the growing layer. In reference to rectangular profiles, the pictorial model of Figure 4.15 goes one step further than that presented by Biasol and Kapon and Ohtsuka; not only must deposition within the grating trenches be considered alongside deposition on the grating teeth, but the relationship between adjacent teeth and trenches must be addressed. Although, unlike the numerical models discussed, the pictorial model developed in this thesis has not yet been confirmed experimentally. A series of structures containing marker-layers will reveal the manner in which material deposition proceeds in submicron rectangular-patterned gratings.

5

Development of Semiconductor Saturable Absorber Mirrors for Mode-Locked Lasers

Semiconductor saturable absorber mirrors, also termed saturable Bragg reflectors, have recently become a widely used means of passively generating ultrashort pulses in a variety of laser cavities. Passive generation of ultrashort pulses is directly applicable not only to optical communication networks, but also to the investigation of ultrafast nonlinear processes [111] and the optical imaging of biological tissue (e.g. optical coherence tomography [112]). A variety of semiconductor saturable absorber mirrors have been fabricated for implementation in both fiber-based lasers as well as solid-state-based lasers; the resulting device designs, characterization, and implementation will be discussed.

5.1 Mode-Locking, Q-Switching, and Q-Switched-Mode-Locking: A Brief Overview

Mode-locking of lasers is attractive as the result is the generation of pulse trains. Unless forced to operate in a single temporal mode, a laser cavity will typically support multiple temporal modes since the gain bandwidth is usually wider than the fundamental cavity-defined longitudinal mode spacing. The relative phase of the many modes will in general be random, as each mode is independent of the other modes supported by the laser cavity; in this instance, the laser is said to be operating continuous wave (CW). If the lasing modes are in some way forced to propagate with a constant relative phase difference, the temporal modes become phase-locked, and the result is a stream of pulses. If all generated pulses have roughly the same peak intensity, the laser is said to be CW-mode-locked. For a relatively uniform pulse peak intensity, the average power within the cavity will be approximately constant and similar to the

average power found in CW lasers. The period of the generated pulses is proportional to the time required to traverse a round trip of the laser cavity. The resulting pulsewidth is generally a function of the gain medium, and is inversely proportional to the gain bandwidth (assuming the cavity-mirrors support the entire gain spectrum) [113,117]. Mode-locking can be generated by both active and passive means. Examples of active mode-locking mechanisms schemes include using (acousto- or electro-optic) or cross-phase modulation (i.e. induced via modulated external pump sources in fiber lasers) [113] to modulate the gain profile in time. Passive mode-locking techniques involve the use of a medium with intensity dependent characteristics (e.g. at low intensities the medium absorbs and at high intensities the medium is transparent). Examples of passive mode-locking techniques are bleaching of dyes, saturation of absorbers, self-phase modulation in fiber lasers, and the optical Kerr effect [114,113]. Currently, the shortest pulses obtained from mode-locked lasers are ~5 fs in width from a Ti:sapphire laser utilizing Kerr-Lens mode-locking and dispersion compensating mirrors (demonstrated both with and without a saturable absorber mirror) [115,116].

Q-switching is a form of cyclical laser cavity dumping from which ultrahigh peak output powers are obtainable. The Q of a cavity is related to the amount of energy stored within the cavity; the larger the reflectivity of the end mirrors, the larger the cavity Q and the lower the required population inversion to instigate stimulated emission. For a laser cavity in a steady state CW operating condition, the population inversion participating in stimulated inversion is maintained at a steady state level. If one of the cavity mirrors is removed, and the gain medium is still pumped, the population inversion will increase above the lasing threshold value. Placing the cavity end-mirror back in position results in rapid depletion of the large population inversion and a large peak output power. If the end-mirror is cyclically removed, the laser is said to be Q-switched. Q-switching can be generated via mechanisms such as a shutter to block an end-mirror [117], or intensity-dependent loss that requires a large amount of energy to saturate [114]. Typical Q-switched repetition rates are on the nanosecond time scale, with peak output powers demonstrated in the megawatt regime [114].

Q-switched-mode-locking is a combination of Q-switching and mode-locking. A Q-switched-mode-locked laser is mode-locked with the pulse repetition rate proportional to the cavity round trip time; however, the mode-locked pulse intensity is modified by a Q-switching envelope. Thus, the intensity of adjacent mode-locked pulses varies and follows that permitted by the Q-switched envelope. Q-switched mode-locking is a common component of the starting dynamics in saturable absorber-mode-locked laser cavities [118,119]. Additionally, a CW-mode-locked laser cavity can be driven into a Q-switched-mode-locked state by a simple perturbation of the cavity (i.e. noise or jarring of the laser cavity). The ability to minimize, or stabilize against, Q-switched-mode-locking is highly attractive.

5.2 Passive Mode-Locking via Semiconductor Saturable Absorber Mirrors

Passive mode-locking devices may be preferred over active mode-locking devices due to their ease of use and lack of external controls. The use of semiconductor saturable absorber mirrors to passively mode-lock various laser cavities is steadily increasing. The basic structure of a semiconductor saturable absorber mirror consists of a highly reflective mirror with an integrated absorbing region. The semiconductor saturable absorber mirror can be used in place of a high reflector within the laser cavity, effectively maintaining the number of components in the laser cavity. The use of normal incidence structures, as opposed to longitudinal structures (i.e. waveguides) is in many cases preferred as normal incidence structures are inherently polarization independent. Additionally, these devices are attractive for a wide range of laser cavities since they may be incorporated either in free-space or butt-coupled to fiber ends and waveguide structures.

One of the more recent passive mode-locking mechanisms is a monolithically integrated device comprised of a distributed Bragg reflector (DBR) and an absorber (comprised of a heterostructure or quantum well structure). The monolithic structure is typically preferred over structures requiring the integration of multiple platforms (i.e. metallization for the high reflector and epitaxy for the absorber) as the monolithic approach requires less post-epitaxial fabrication. For comparison, the use of a metal layer for the high reflector requires deposition of the metal following epitaxy, and removal of the semiconductor substrate. In general, controlled removal of an entire substrate without causing damage to the epitaxial layers can be quite difficult. Furthermore, epitaxial deposition is highly accurate in terms of thickness control, and affords considerable flexibility in device design.

The basic mode-locking mechanism generated via semiconductor saturable absorber mirrors is intensity-dependent saturation of the absorber. In general, for incident light with a wavelength approximately equal to the characteristic bandgap of the absorbing semiconductor material, at low intensities the light will be absorbed by the semiconductor medium via the generation of carriers in the conduction and valence bands, effectively removing the energy from the laser cavity. At high incident intensities, the conduction band will become fully populated (i.e. the absorber will be bleached). Once the absorber is bleached, any additional light will not be absorbed but will instigate stimulated emission (and subsequently amplification) and propagate through the absorber with little or no absorption. Light passing through the absorber will reach the DBR and be reflected back in to the laser cavity. As a result of the absorber behavior, the supported cavity modes are forced to operate with the same phase condition in an effort to minimize intracavity loss, with the result being the generation of pulses.

Because the minimum attainable pulsewidth of a mode-locked laser is inversely proportional to the bandwidth of the gain medium, in order to achieve the shortest possible pulses the saturable absorber mirror must support a bandwidth equal to or greater than the gain bandwidth. If the bandwidth of the DBR is narrower than the gain bandwidth, the shortest attainable pulsewidth may be a function of the DBR and not the gain medium. (Note: these statements assume that the other cavity mirrors have a bandwidth larger than that of the gain medium.)

Other variations of semiconductor saturable absorber mirror structures are p-i-n (and subsequently biased) designs [120], and anti-resonant absorber structures [121]. Absorber mirror structures may be further modified via the addition of dielectric coatings. The optimum design of a semiconductor saturable absorber mirror is dependent on the laser cavity for which it is designated. The need to tailor the absorber mirror structure to each laser cavity is important, as lasers operate with differing amounts of loss, intracavity powers, etc.

5.2.1 Semiconductor Saturable Absorber Mirror Design

Although semiconductor saturable absorber mirrors have been employed for mode-locking a wide variety of laser cavities [i.e. 121,122,123,124,125], it is crucial to design a saturable absorber mirror for each specific application. The differing loss, gain spectrum, internal cavity power, etc., of each laser necessitates slightly different absorber characteristics. The laser cavities for which the saturable absorber mirrors presented in this thesis are currently being designed are fiber-based laser cavities (with Er/Yb codoped fiber amplifiers and waveguide amplifiers) and Cr^{4+}:YAG solid-state laser cavities.

The basic semiconductor saturable absorber mirror chosen consists of a 22-pair GaAs/AlAs DBR (with > 99% reflectivity at the center wavelength) and a $\lambda/2$ InP-based absorber deposited directly on the DBR. The GaAs-based DBR was chosen over an InP-based equivalent since in order to achieve ~99 % reflectivity in an InP/InGaAsP DBR approximately twice as many pairs are required as compared to a GaAs/AlAs DBR. InP-based materials were chosen for the absorber region so as to span the gain spectrum of both Er-doped fiber and Er/Yb-doped phosphate glass (bandwidths ~1.53-1.58 μm), as well as that of a Cr^{4+}:YAG crystal (gain bandwidth ~ 1.4-1.6 μm).

The center wavelength of the DBR, as well as the bandgap of the absorber, are chosen based on the specific laser. In most cases, the DBR is centered at 1.55 μm, has a reflectivity of ~99.9 %, and a bandwidth of over 100 nm, as determined via transmission measurements. Shown in Figure 5.1 is the measured transmission spectrum of the DBR used for most of the structures developed at MIT. Both single layers of InGaAs as well as InGaAs quantum wells (clad by InP), were chosen for the absorbing material. Saturable absorber mirror structures with quantum well absorber regions having bandgaps ranging from

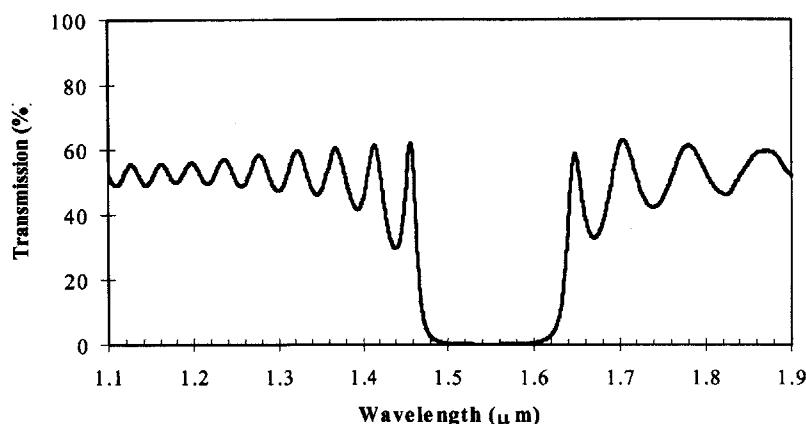

Figure 5.1 Measured transmission spectrum of a 22-pair GaAs/AlAs DBR.

~1.45 μm to ~1.58 μm have been fabricated. Structures containing single ~110 nm thick InGaAs (λ ~ 1.57 μm) absorbers have also been fabricated.

The bulk of the analysis of the semiconductor saturable absorber mirror structures was accomplished via photoluminescence (PL) [both room and low temperature], high resolution double axis x-ray diffraction (HRDAXD), and pump-probe and saturation fluence measurements. The materials analysis and quality of the InP/InGaAs absorber region has been addressed in detail in Section 3.2. As is evident from the material analysis techniques, the InP/InGaAs material in the absorbing region contains a large number of defects generated at the InP-GaAs interface. For a saturable absorber application, the more rapidly the absorber recovers from bleaching, the more closely spaced pulses are able to reside; in other words, a rapidly recovering absorber is desired for high repetition rate mode-locked lasers (with application to time division multiplexed (TDM) communication network sources, for example). Although the presence of non-radiative recombination centers located at defect sites is detrimental to the majority of optoelectronic devices (i.e. lasers, detectors, etc.), the reduced carrier lifetime afforded via non-radiative recombination centers in saturable absorbers designed for laser mode-locking is beneficial. Cunningham, *et al* have developed a technique to intentionally generate a large number of dislocations during the GSMBE deposition of InP-based absorbers on GaAs/AlAs DBRs [54] resulting in carrier lifetimes of ~14 ps [126]; this technique is described in more detail in Section 3.2. The use of ion implantation [127,128] and bombardment schemes have also been used to reduce the carrier lifetime in saturable absorber structures. Proton bombardment studies of the structures presented in this thesis are presently being carried out by J. Gopinath at MIT. Lifetimes as short as ~1 ps have been achieved using a proton bombardment dose of 10^{15} protons/cm^2.

In regards to the possibility of compositional modulation within the InGaAs layers due to the miscibility gap in the InGaAsP materials system, the effect on the performance of a saturable absorber is as of yet unknown. Initial speculations are that the compositional modulation, since it causes a broader PL feature (due to the varying range of bandgaps within the modulated material) likewise smears out the absorption edge. As the lasers of interest are typically mode-locked at wavelengths above the bandedge of the absorber, a slight smearing of the absorption spectrum should not significantly affect the device performance.

An additional design parameter inherent in the absorber mirrors with $\lambda/2$ absorber regions is the number of quantum wells (or thickness of the single layer) and the respective location within the InP $\lambda/2$ layer. Placement of the absorbing material near the null of the standing-wave electric field present in the absorber mirror structure (see Figure 5.2) significantly increases the energy density required to fully bleach

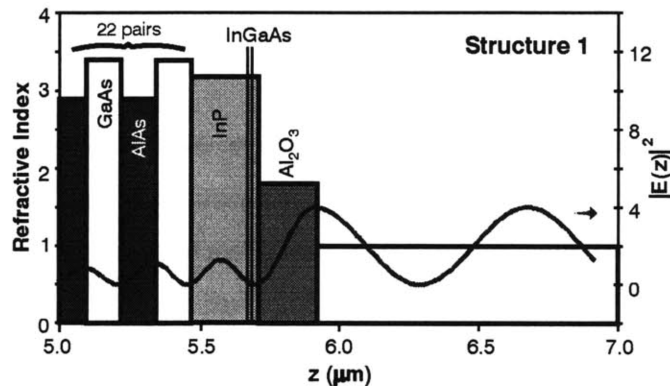

Figure 5.2 Saturable absorber design in which the absorbing quantum wells are located near the null of the electric field (at $\lambda \sim 1.54$ μm) within the structure. The electric field is calculated as a function of position from the GaAs substrate; in order to obtain the intensity within the structure the electric field should be multiplied by the refractive index. A dielectric antireflection coating is also present on this structure.

the absorber; this type of design is applicable to solid-state lasers for which the intracavity losses are quite low and the intracavity powers are quite high. For low loss cavities, only a small absorber-induced loss is required to instigate mode-locking; large absorber losses may prevent lasing. For lasers with low intracavity powers and large intracavity losses, such as many fiber lasers, requirements of the absorber are quite different. To induce mode-locking, the absorber must be bleachable with small incident powers, thus placement of the absorbing material near the maximum of the standing-wave electric field in the absorber

mirror structure is required. Figure 5.3 is an example of a semiconductor saturable absorber mirror designed for high-loss fiber laser cavities.

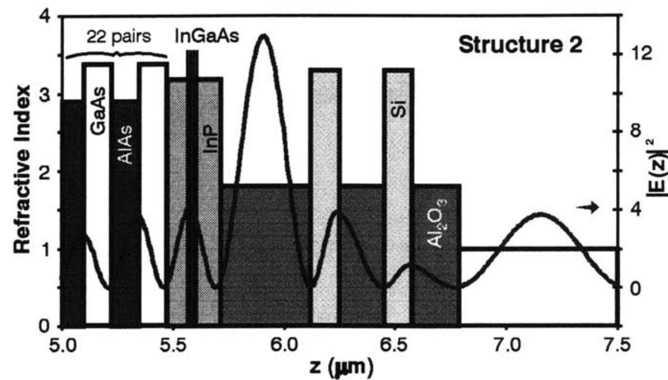

Figure 5.3 Saturable absorber design in which the absorbing quantum wells are located near the maximum of the electric field (at $\lambda \sim 1.54$ μm) within the structure. The electric field is calculated as a function of position from the GaAs substrate; in order to obtain the intensity within the structure the electric field should be multiplied by the refractive index. A 5-layer dielectric resonant coating is also present on this structure.

To further adjust the saturation characteristics of the fabricated saturable absorber mirror structures, dielectric coatings have been added. Specifically, antireflection coatings and coatings designed to create a resonant cavity about the half-wave absorber layer have been designed. The antireflection coatings consist of either a quarter-wave Al_2O_3 layer, having ~2% reflectivity at 1.53μm (see Figure 5.2), or a series of $TiO_2/Si/Al_2O_3$ layers resulting in ~95% reflectivity at 980 nm and ~5% reflectivity at 1.53 μm (see Figure 5.3). The resonant coatings consist of a 5 layer Si/Al_2O_3 with a reflectivity of ~70%.

5.2.2 Optical Characterization of Semiconductor Saturable Absorber Mirrors

For device characterization under conditions attainable in mode-locked lasers, i.e. large energy densities and short pulses, dynamic differential reflectivity (pump-probe) measurements and saturation fluence measurements were performed. Saturation fluence measurements reveal the nonsaturable loss inherent in the absorber mirror structure and the energy density required to fully saturate the absorber. Further discussion of the ultrafast optical characterization of the semiconductor saturable absorber mirrors can be found in [131].

The saturation fluence measurements were performed at 1.54 μm using 150 fs pulses from a synchronously-pumped optical parametric oscillator (OPO) with a repetition rate of 82 MHz. The

reflectivity was measured over a wide range of incident energy densities which was varied by changing the spot size on the absorber mirror. Figure 5.4 and Figure 5.5 depict the reflectivity as a function of energy

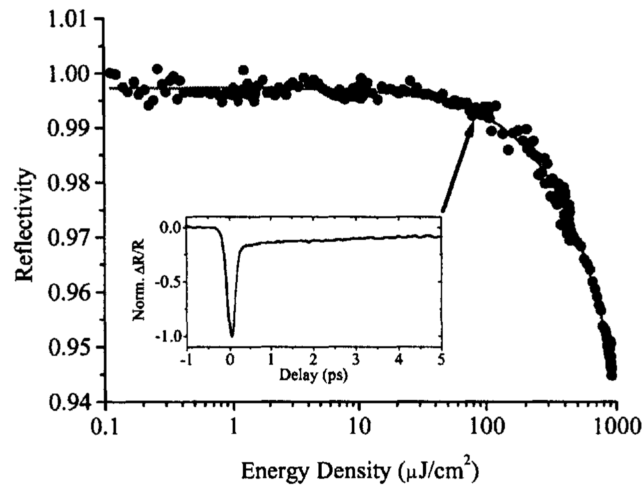

Figure 5.4 Saturation fluence measurement of the structure shown in Figure 5.2. The inset depicts the pump-probe measurement at ~80 $\mu J/cm^2$.

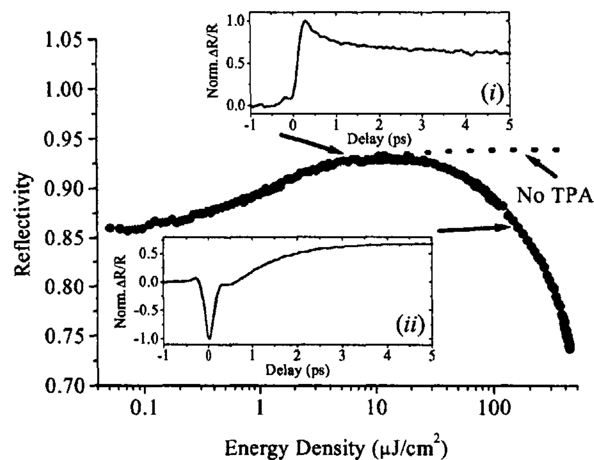

Figure 5.5 Saturation fluence measurements of the structure depicted in Figure 5.3. Inset (i) is a pump-probe measurement at ~10 $\mu J/cm^2$; inset (ii) is a pump probe measurement at ~200 $\mu J/cm^2$.

density for Structures 1 and 2, respectively. The significant feature in Figure 5.4 is the rapid roll-off in reflectivity starting at ~150 $\mu J/cm^2$. The quantum wells are positioned near a null of the electric field and the measurements were performed ~90 nm below the bandedge of the quantum wells (λ ~ 1.45 μm), hence

the resulting saturable absorption was negligible. Measurements were performed at energy densities up to 1000 $\mu J/cm^2$ without observable damage to the sample. For Structure 2, in which the quantum wells are centered within the InP region, Figure 5.5 reveals saturable absorption at a saturation fluence of ~1 $\mu J/cm^2$, in addition to a rapid roll-off in reflectivity, which begins at ~20 $\mu J/cm^2$. In contrast to Structure 1, the quantum wells are located near a peak of the electric field resulting in significant absorption. Visible damage to both the semiconductor material and the resonant coating was observed for pulse energy densities greater than 400 $\mu J/cm^2$, which is outside of the measurement range shown in Figure 5.5. The fluence at which the reflectivity roll-off occurs is roughly 8 times lower for Structure 2 than for Structure 1, and is consistent with the calculated internal enhancement produced by the resonant dielectric coating. A GaAs/AlAs DBR, identical to those on which the saturable absorbers were deposited, was also measured up to energy densities of 1000 $\mu J/cm^2$ and did not exhibit any noticeable change in reflectivity. For a similar DBR structure, the calculations of Obeidat, *et al.* predict no reflectivity change over the same range of energy densities [132].

Pump-probe reflectivity measurements were performed to clarify the cause of the reflectivity drop observed in the saturation fluence measurements; 150 fs pulses at 1.54 μm from an OPO were used in a cross-polarized, colinear arrangement. The inset of Figure 5.4 shows the resulting pump-probe trace at an energy density of ~80 $\mu J/cm^2$; the dominant dynamic is the pump pulse-induced two-photon absorption (TPA) observed by the probe pulse when the two pulses overlap. Also present, on a longer time scale, is free carrier absorption of the probe pulse as a result of carriers produced by TPA of the pump pulse. Insets (*i*) and (*ii*) of Figure 5.5 depict the dynamic differential reflectivity for the resonantly enhanced structure (Figure 5.3). Inset (*i*), comprised of both rapid and longer-lived components, is the normalized change in reflectivity at an energy fluence near saturation, ~10 $\mu J/cm^2$, where absorption bleaching occurs. (Inset (*i*) is qualitatively similar to pump-probe measurements on other saturable absorber structures.) The pump-probe response at ~200 $\mu J/cm^2$ [see inset (*ii*)] is well within the high fluence regime (energy densities > ~20 $\mu J/cm^2$) and is considerably different from a typical absorption bleaching response. Near zero delay, the absorption bleaching is saturated and the TPA component dominates. Transient hot electron-assisted absorption is also apparent on a 1 ps time scale. Following TPA and hot electron-assisted absorption, the quantum well bleaching recovers with a time constant comparable to that observed in inset (*i*).

Further pump-probe analysis, performed by P. Langlois and M. Joschko reveals the presence of free carrier absorption (FCA) at high energy densities [129]. FCA is a process that typically involves an electron, a photon and a phonon [130]. Given a conduction band filled with electrons, absorption of an additional photon can result in the newly arrived electron knocking an existing electron out of the conduction band and into a higher energy band. Relaxation of the electron back to the conduction band

energy level will typically involve emission of a phonon. FCA can also be induced via TPA, which also injects an electron into an energy band of greater energy than the conduction bandedge. The existence of FCA within saturable absorber mirrors further contributes to the observed nonlinear-induced loss (the decrease in reflectivity apparent in saturation fluence measurements).

With pump-probe measurement confirmation that TPA is the dominant cause of the reflectivity drop observed in the saturation energy measurements, a fitting function for the observed saturation response was generated. (Although Structure 2 exhibits both fast and slow recovery dynamics, only a fast absorber model is used for illustration.) The addition of a term to account for TPA in the standard fast absorber model produces a reasonable fit, as seen by the solid lines in Figure 5.4 and Figure 5.5. (In contrast, the dashed line in Figure 5.5 is the calculated reflectivity using the fast absorber model if TPA is not present.) In fitting the data of both structures, the TPA coefficient of InP, $\beta = 90$ cm/GW, was used.

TPA modification of the typical fast saturable absorber expression and the impact on mode-locking stability using the standard stability analysis has been investigated. The stability conditions derived in [133] for CW mode-locking against Q-switched mode-locking were used, with the effect of TPA in the saturable absorber added to the model. Fast saturable absorption, TPA, loss, and gain saturation are included in the stability analysis of the CW mode-locked state against perturbations. Figure 5.6 illustrates

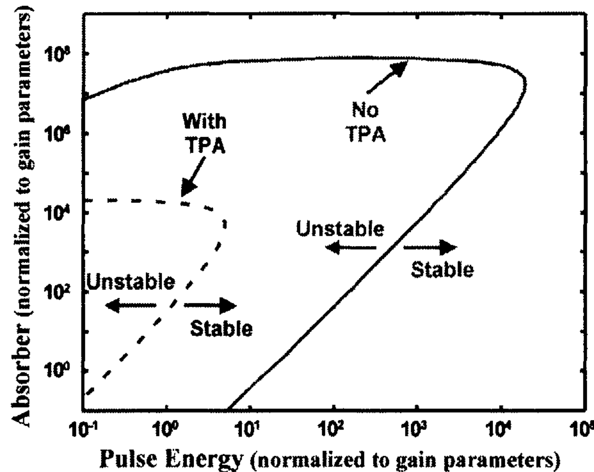

Figure 5.6 Calculated stability contours for a fast saturable absorber mode-locked laser. Q-switched mode-locking is present in regions labeled "Unstable". The area within the dotted line is the unstable region with TPA included in the model.

the calculated stability regions in a logarithmic plot of the absorber saturation power versus pulse energy,

both normalized to the gain saturation. The solid line in Figure 5.6 indicates the instability boundary when TPA is not included; the inclusion of TPA reduces the instability boundary to the dashed line. The region of stability is greatly increased in terms of both pulse energy and absorber saturation when TPA is present in the absorber structure.

Several extensions of this model are necessary for application to specific lasers. Use of a saturable absorption model other than the fast saturable absorption model will modify the calculated stability regions as seen in Figure 5.6. While TPA provides stabilization against Q-switched mode-locking, it will also lower the threshold for the occurrence of multiple pulses. As the peak intensity of a pulse increases, TPA-induced loss will also increase, thus a lower-loss condition for multiple, reduced peak intensity pulses will be favored. Generation of multiple pulses via pulse break-up does not necessarily result in pulses equally spaced at multiples of the cavity round-trip time, but rather can result in "pulse bunching".

5.2.3 Implementation in Fiber-Based and Solid-State Lasers

Er/Yb Waveguide Laser

Shown in Figure 5.7 is a diagram of a the fiber laser containing an Er/Yb codoped phosphate glass waveguide amplifier. This laser cavity is extremely attractive since it is theoretically scalable to very short cavity lengths, such that the entire cavity consists of the waveguide amplifier with a high reflector and saturable absorber mirror both butt-coupled to the waveguide facets. (For this type of arrangement, the laser diode amplifier pump will reside outside of the laser cavity.) An ultrashort laser cavity of this type is particularly attractive for use in all-optical communication networks. The compactness of the cavity is not only beneficial from a size perspective (5.2 cm), but also from a repetition rate perspective; such a small mode-locked cavity is expected to generate pulses at repetition rates of ~2 GHz.

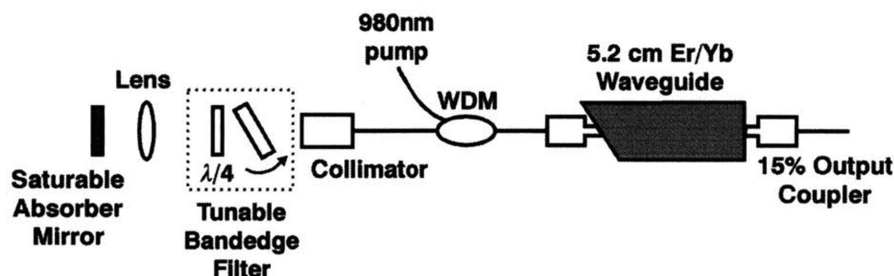

Figure 5.7 Diagram of the mode-locked fiber laser containing an Er/Yb codoped phosphate glass waveguide as the amplifying medium.

The best results obtained from this laser cavity were obtained with the use of a semiconductor saturable absorber mirror in which the InP absorber region consists of an InP/InGaAs heterostructure with ~100 nm of InGaAs (λ ~ 1.57 μm) centered within the InP $\lambda/2$ layer. An antireflective coating was also deposited on the absorber mirror. The shortest mode-locked pulses achieved were ~1 ps in width at a wavelength of 1.545 μm, and demonstrated at a repetition rate of 25 MHz. The 1 ps pulses were only obtainable with the use of the filtering elements (see Figure 5.7). Without the filtering elements, the operating wavelength of the laser was restricted to 1.53 μm, which corresponds to the peak of the Er/Yb gain spectrum. Operation of the laser at 1.53 μm resulted in ~9.8 ps pulses that were slightly chirped; the chirping is attributed to the gain peak-limited operating wavelength. With the addition of the filtering elements and the subsequent suppression of the strong gain feature at 1.53 μm, tuning of the laser was also achieved (1.542 - 1.553 μm) with pulsewidths of ~3 ps.

Actively Harmonically Mode-Locked Fiber Laser

Actively harmonically mode-locked fiber lasers are attractive for generation of ultrashort pulses at GHz repetition rates. As the gain medium is typically Er-doped silica fiber, the required lengths for the gain section are quite long, thus the fundamental repetition rate of the fiber cavity is much lower than the GHz regime. By means of an active mode-locking mechanism, for example a $LiNbO_3$ amplitude modulator, the laser can be mode-locked at repetition rates that are multiples of the fundamental cavity-defined repetition rate. A diagram of the actively harmonically mode-locked fiber laser is depicted in Figure 5.8.

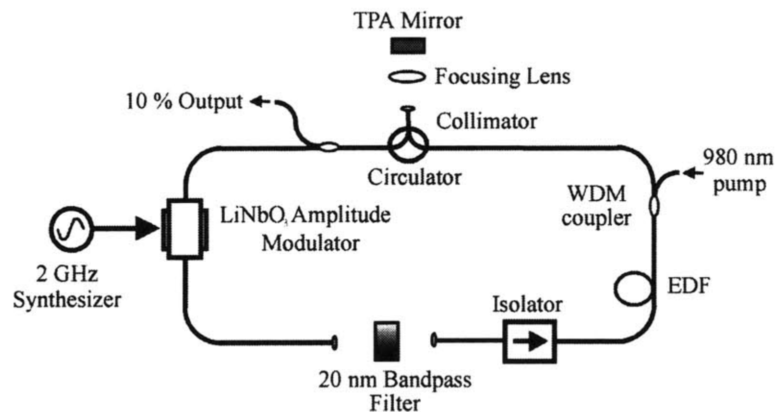

Figure 5.8 Schematic of an actively harmonically mode-locked fiber laser stabilized with a TPA structure.

Active mode-locking of a fiber laser very often results in varying pulse intensities or missing pulses. Various techniques have been applied in order to stabilize the intensities, however issues such as the need

for active control (e.g. phase-locking circuits to control the cavity length [134]), environmental sensitivity (e.g. nonlinear polarization rotation [135]), the addition of hundreds of meters of fiber (e.g. self-phase modulation plus filtering [136]), etc., are not highly desirable. The ability to equalize the pulse intensities and subsequently reduce the dropout of pulses via a passive technique is extremely attractive. The use of two-photon absorption (TPA) as a passive intensity limiter in mode-locked lasers (see Section 5.2.2) has also been applied to the fiber ring laser depicted in Figure 5.8.

The TPA structure utilized consists of a ~5.2 μm InP layer deposited on a 22-pair GaAs/AlAs DBR (centered at 1.55 μm, reflectivity > 99%). With the addition of the TPA structure, and a focusing element to control the magnitude of TPA, the pulse intensities were stabilized, and verified via the absence of missing pulses.

5.2.4 Additional Device Designs

Additional semiconductor saturable absorber mirror designs that have been considered throughout the duration of the project include a broadband saturable absorber mirror and a cascaded semiconductor saturable absorber mirror. The broadband absorber mirror design is based on a $GaAs/Al_xO_y$ DBR design. The cascaded absorber mirror design is comprised of multiple $\lambda/2$ layers in order to increase the absorption depth (or saturable loss).

Current absorber mirror designs are, in most cases, based on GaAs/AlAs DBRs, which generate a reflectivity bandwidth of ~ 100 nm (see Figure 5.1). The ability to fabricate a DBR in which the materials have a large index contrast in order to obtain a much larger reflectivity bandwidth is highly attractive since the minimum achievable pulsewidth in a mode-locked laser is dependent on the spectral width that the cavity mirrors are able to support. For laser cavities such as Ti:sapphire and Cr^{4+}:YAG, in which the operating wavelengths span a few microns, broadband mirrors are needed in order to mode-lock the entire gain spectrum. Sub-7 fs pulses demonstrated in Ti:sapphire lasers [115, 137], have been obtained by use of dielectric mirrors with reflectivity bandwidths on the order of ~0.5 μm. Although these lasers have been mode-locked via the Kerr-lens effect, and the dielectric mirrors are custom designed to compensate for chirp [138], the mirrors must support a laser spectrum of ~0.5 μm in order to obtain ultrashort pulses. The disadvantage of the current chirped mirror designs is the inability to monolithically integrate them with an absorber; current chirped mirrors are comprised of ion-beam sputtered dielectric materials such as SiO_2 and TiO_2 [138]. Thus far, integration of semiconductor saturable absorber mirrors within the Ti:sapphire lasers with mode-locked pulses in the sub-7 fs pulse regime [116,139] has required additional fabrication steps. For instance, the absorber used by Sutter, *et al* [140] is comprised of GaAs and AlAs, with a thick

Ag highly reflective layer deposited following epitaxy; this procedure requires the somewhat painful process of removing the substrate.

As the reflectivity bandwidth is a function of the index difference between the two materials, in order to increase the bandwidth, a material of index lower than AlAs needs to be incorporated. Recently, wet thermal oxidation of AlAs-based materials has been intently studied [e.g. 141,142,143,144,145,146,147, 148], and implemented in a variety of structures (e.g. vertical cavity surface emitting lasers [149,150,151,152,153,154,155] and one-dimensional [156] and two-dimensional [157] photonic bandgap devices). Following oxidation, the refractive index of Al_xO_y is ~ 1.5-1.6 [147], thus 6 pairs of GaAs/Al_xO_y would result in a DBR with a reflectivity greater than 99% over ~0.5 μm. Depicted in Figure 5.9 is the

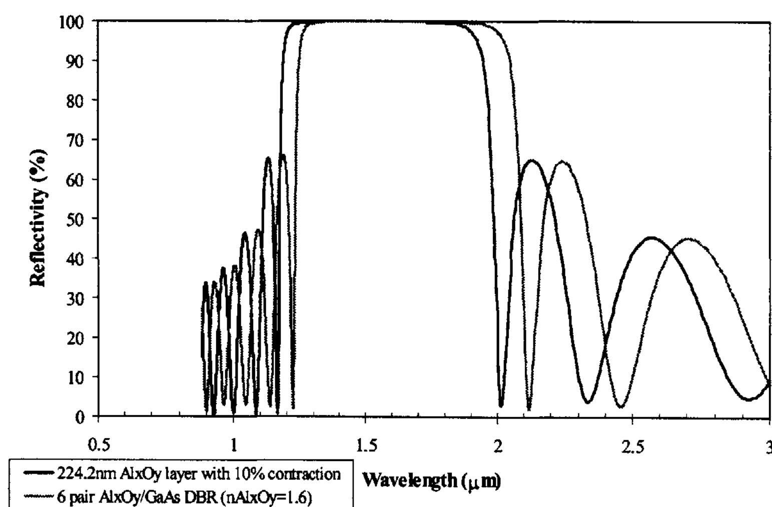

Figure 5.9 Simulation of the reflectivity spectrum of a 6-pair GaAs/Al_xO_y DBR. The dark trace assumes 10% contraction of the Al_xO_y layer resulting from the oxidation process.

simulated reflectivity spectrum of a 6-pair GaAs/Al_xO_y DBR, centered at 1.55 μm (note: the simulation is performed with the index of refraction of Al_xO_y independent of wavelength); the thickness of the GaAs layer is 115 nm and the oxidized layer 224.2 nm. However, upon oxidation, AlAs layers have been found to contract roughly 10% [142,158]. Shown for comparison in Figure 5.9 is the reflectivity spectrum with 10% contraction of the oxidized layer. Even with modification of the oxidized layer height, the reflectivity bandwidth in which R > 99% is still greater than 0.4 μm, a four-fold increase over the unoxidized version.

For design of the oxidizable DBR, the introduction of strain between the GaAs layer and the oxidized layer must be considered, as well as the robustness of the interface. Various research groups have found that oxidation of pure AlAs, although it oxidizes quite rapidly, results in delamination of the GaAs layers

[142,158]. In order to minimize GaAs delamination from the oxidized layer, the AlAs-GaAs interface can be graded, leaving an $(Al_xGa_{1-x})_xO_y$-GaAs interface, which introduces less strain [142,145] and results in a more thermally stable interface [158]. Furthermore, pure AlAs is a relatively unstable material; AlGaAs materials, due to the addition of Ga, are significantly more stable. As has been observed in GaAs/AlAs DBRs, AlAs, over time, will degrade and oxidize in air, with the oxygen route being growth defects within the structure or the edges of the sample. Oxidation through the defects results in destruction of the layered structure akin to an explosion; shown in Figure 5.10 is a Nomarksi interference contrast microscopy image

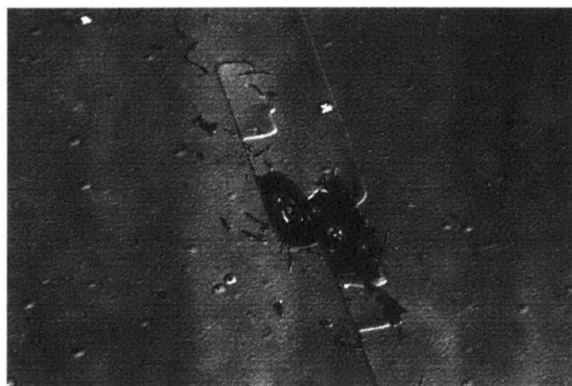

Figure 5.10 Nomarski interference contrast image (200x magnification) of the surface of the structure depicted in Figure 5.2. The slip lines and wire-like pieces are the result of oxidation of the AlAs layers in the DBR. Any visible vertical and horizontal striations are caused by the printer.

of a GaAs/AlAs DBR-based semiconductor saturable absorber mirror in which the AlAs in the mirror has oxidized and locally damaged the layered structure. For the above mentioned reasons, the designed broadband semiconductor saturable absorber mirror structure consists of AlGaAs/GaAs with graded interfaces. The chosen AlGaAs composition is 90% Al, graded to 78% Al over 30 nm; the thickness of the $Al_{0.78}Ga_{0.12}As$ layer at the GaAs interface is ~ 5 nm. The designed total thickness of the AlGaAs layer is 224.2 nm.

In order to increase the absorption depth of a semiconductor saturable absorber mirror, more of the absorbing material needs to be placed near the maximum of the standing-wave electric field profile within the structure. One means of achieving this is to replace quantum wells with a single layer; however, from pump-probe measurements as well as performance in mode-locked fiber lasers, this modification does not change the absorption depth of the devices described in Section 5.2 significantly. In order to more significantly alter the absorption depth, without the addition of dielectric coatings, multiple absorber regions may be cascaded. Furthermore, within each absorber region, the absorbing material is located near

the maximum of the electric field profile. Also, by cascading multiple absorber regions, not only is the saturation depth increased, but the magnitude of TPA may likewise be increased.

Further tailoring of the semiconductor saturable absorber mirror structures may include material and structural choices so as to select a specific contribution of TPA and FCA for the designated laser cavity.

6

Development of Semiconductor Optical Amplifiers for All-Optical Switching Techniques

Thus far, the most rapid switching rates have been achieved in fiber-based systems, utilizing a nonlinear medium. An advantage of nonlinear optical switching is the dependence of the switching state on the intensity of a propagating signal. Utilizing nonlinearities, either in fiber or semiconductors, is beneficial as the nonlinearity typically recovers on a time scale less than a nanosecond [113,160]. The primary advantage of using a semiconductor to provide the nonlinear switching mechanism is the larger refractive index nonlinearity as compared to silica fiber; fiber lengths required to nonlinearly induce a change in refractive index equivalent to a ~1 mm semiconductor device are typically on the order of meters [113]. Switching of bit rates upwards of 1 Tbps, using fiber-based switching schemes that incorporate a semiconductor medium, have recently been reported [5,159]. Monolithic integration of interferometric optical switching schemes in InP materials is also very promising; demultiplexing of data rates just under 100 Gbps have been reported [161].

In addition to operation at rates faster than current electronic switching rates (~ 40 GHz), all-optical switching is attractive since direct integration with current optical communication networks is feasible. In order perform simple network functions using optical logic, operations such as AND, NAND, OR, XOR, and INVERT, need to be performed in the optical domain. Additionally, operations such as wavelength conversion (e.g. for integration of wavelength division multiplexing (WDM) and time division multiplexing (TDM) technologies), rate conversion, clock recovery, and all-optical buffering need to be implemented.

6.1 Semiconductor Optical Amplifiers for All-Optical Switching

In general, semiconductor optical amplifiers (also termed semiconductor laser amplifiers) are semiconductor lasers without feedback. Thus, analysis of Semiconductor Optical Amplifiers (SOAs) stems from the well known analysis of semiconductor lasers. The basic SOA structure is similar to that of a laser, in which the active region (or gain region) is comprised of a double heterostructure or quantum well structure. Issues pertaining to material quality, maximum achievable gain, and electrical pumping efficiency are likewise similar to those addressed in laser structures.

For amplification of optical signals, operation of the SOA within a region in which the gain is roughly linear is preferred in order to suppress undesired effects such as crosstalk and chirp [162]. For implementation in optical switching schemes, the nonlinear behavior, in response to an optical pulse, is exploited. For optical switching applications, SOAs are generally used as gain-modifying mechanisms or wavelength-modifying mechanisms. For application to an ultrafast nonlinear interferometer, the gain-modifying mechanism is utilized and will be discussed.

Commensurate with variation in the carrier population (or gain) of a SOA is a subsequent variation of the refractive index [160]. The response of the SOA to an incident light pulse falls into two general categories: the long-lived ($>$ 1 ps) and ultrashort ($<$ 1 ps). The long-lived (or interband) response is dominated by recovery of intensity-induced changes in the carrier population; the recovery time is typically on the order of 1 ns for InP-based devices [55]. The response of the SOA to incident pulses with durations greater than 1 ps will be affected predominantly by the long-lived refractive index changes. For ultrashort pulses, the ultrafast response of the SOA is dominated by intraband dynamics, and is dependent on effects such as spectral hole burning and carrier heating and cooling. Intraband dynamics are dominant on a time scale less than 1 ps, therefore pulses of width less than 1 ps will be affected by the ultrafast response.

Typically in all-optical switching configurations, the control pulse is of significant intensity in order to modify the carrier density within the SOA. The signal pulses, on the other hand, are typically weak such that they will not significantly alter the carrier dynamics of the SOA, but rather experience the altered SOA medium. Furthermore, for maximum interaction with the SOA medium, the wavelength of the control and signal pulses need to be near the gain peak of the SOA [163].

For incident light having a wavelength near the bandgap of the SOA, the changes in refractive index are approximately linearly proportional to the changes in the carrier density [164]. Thus, the refractive index is also dependent on the intensity of the incident signal. The variation of the refractive index, due to variations in the carrier density, results in an associated phase change for an incident light pulse

propagating through the SOA immediately following the carrier density manipulations and prior to recovery of the population inversion. The phase change, $\Delta\phi$. accumulated over the length of the device can be determined from

$$\frac{E_{out}}{E_{in}} = e^{-j\Delta\phi - \alpha} \qquad \text{Eq. (6.1)}$$

where α is the absorption and

$$\Delta\phi = \frac{2\pi L \Delta n(N)}{\lambda_o} \qquad \text{Eq. (6.2)}$$

in which L is the SOA device length, λ_o is the freespace wavelength, and $\Delta n(N)$ is the change in refractive index as a function of the carrier density. In interferometric switching schemes, the phase change required for alteration of the switch output is an odd integer-multiple of π.

For operation, a SOA can be biased in three regimes; absorption, transparency, and gain; Figure 6.1 is

Absorption Regime:

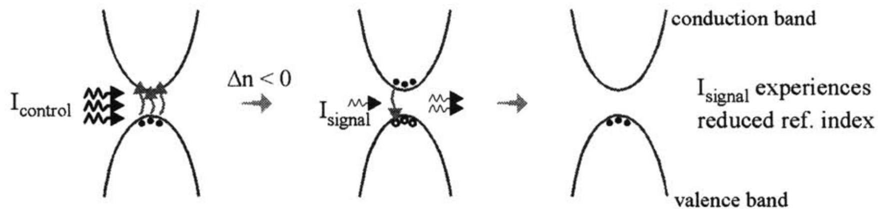

Transparency Regime:

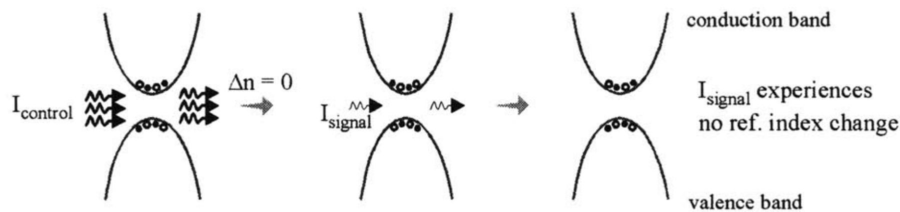

Gain Regime:

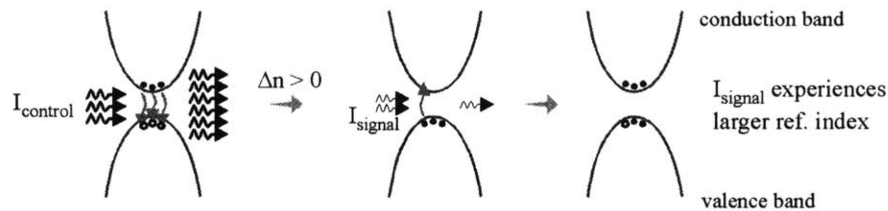

Figure 6.1 Depiction of the three regimes of operation for a SOA.

depiction of the three regimes. In the absorption regime, little or no external current is applied to the device

such that the SOA will absorb the intense incident control pulse. Absorption of the control pulse will generate a large number of carriers in the conduction band such that a signal pulse propagating through the SOA will see a large carrier density in the conduction band and experience amplification via stimulated emission as the pulse passes through the device (see Figure 6.1). For pulses longer than 1 ps, the large carrier density in the conduction band translates to a decrease in the refractive index [160, and references within]. For a SOA biased in the gain regime (large external current is applied to create a large population inversion), propagation of an intense control pulse will generate stimulated emission (and possibly saturate the gain), and deplete the carrier density in the conduction band. Thus, a weaker signal pulse following the control pulse will "see" a smaller population inversion and subsequently a larger refractive index (see Figure 6.1) [160]. Furthermore, the weak signal pulse will experience less amplification or possibly absorption due to the reduced population inversion. If the SOA is biased in the transparency regime (as in Figure 6.1), such that the carrier density in the conduction band and the valence band are equal, propagation of an intense control pulse will leave the carrier density virtually unchanged as the probability of stimulated emission and absorption are roughly equal, and likewise the long-lived refractive index will be unaltered; an applied signal pulse will not experience an altered refractive index or amplification [160]. The chosen bias regime is determined in part by device applications. In general, for a large applied bias, the carrier density will return to the steady state biased value more quickly, effectively reducing the carrier lifetime [164]. With the proper wavelength choice for the signal pulse (i.e. bandgap less than that of the SOA), the signal pulse may propagate through the SOA without being absorbed, but will still be affected by the control pulse-induced refractive index changes.

The available phase change in a SOA is many multiples of π [165]. Shown in Figure 6.2(a) is a

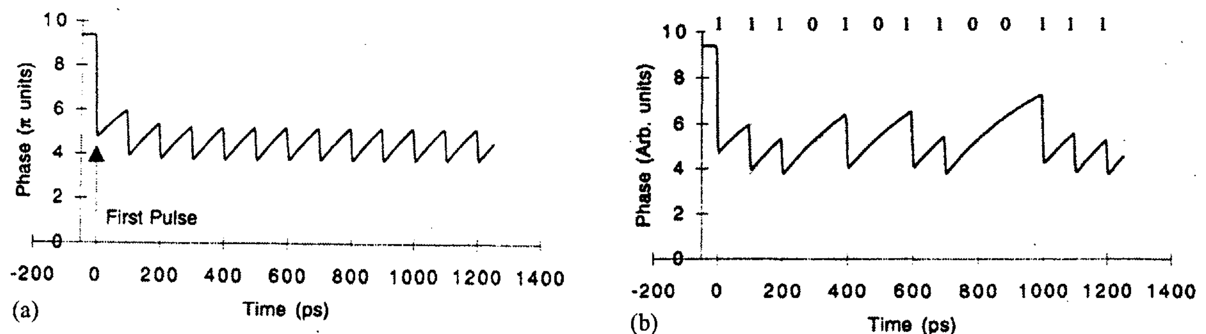

Figure 6.2 (a) Calculated phase response of a SOA a a continuous train of intense pulses. (b) Calculated phase response of a SOA to a variable train of intense pulses. Figures from [165].

calculation of the phase response of a SOA, having a 300 ps lifetime, to a regular train of pulses [165], i.e.

the control pulse for a demultiplexer. The initial phase change in response to the first pulse is much larger than π, yet after application of the first pulse, the gain reduction is periodic, such that the gain recovers to roughly the same magnitude between adjacent pulses. In contrast, Figure 6.2(b) is the calculated phase response of a SOA to a variable train of pulses. By optimum choice of the recovery time (i.e. by applied bias) with respect to the control pulse repetition rate, a consistent phase change of π is easily achieved. Manning, *et al* have experimentally measured recovery of a π phase shift in a SOA in as little as ~12.5 ps [165].

Apparent in Figure 6.2 is the gain recovery of the SOA between incident pulses. The slope associated with the carrier density changes subsequently imparts a phase change on any signals propagating through the SOA. Thus, the repetition rate of the signal pulses with respect to the gain recovery dynamics is critical to the performance of an all-optical switch. Switching techniques that utilize two independent propagation paths (i.e. Mach-Zehnder-based devices), in which the SOA is located in only one arm, are highly susceptible to the SOA recovery dynamics. Switching schemes which utilize a single arm, or identical paths, effectively cancel the gain recovery dynamics since the all pulses traverse the same path.

6.2 The Ultrafast Nonlinear Interferometer

The development of ultrafast all-optical time division multiplexed (TDM) communication networks necessitates the need for all-optical signal processing and routing. The Ultrafast Nonlinear Interferometer (UNI) has been successfully demonstrated at data rates up to 40 Gbps as a demultiplexer [166], and up to 100 Gbps data rates performing bitwise logic functions [8]. The UNI has also been implemented in a circulating shift register as the regenerative switch [166]. The UNI is an attractive device not only because it is a single arm interferometer (see Figure 6.3), which eliminates path length difference instabilities, but

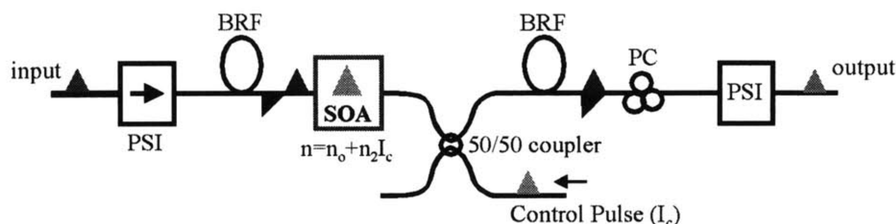

Figure 6.3 Diagram of the ultrafast nonlinear interferometer (UNI). PSI is polarization-sensitive isolator, SOA is semiconductor optical amplifier, BRF is birefringent fiber, and PC is polarization controller.

also because it is geometrically suitable for the cascading of multiple devices. An input pulse launched into the interferometer passes through a polarization sensitive isolator (PSI) to control all incoming pulse polarizations. After propagation through a section of birefringent fiber, separating the pulse into TE- and TM-polarized components that are delayed with respect to one another, both components pass through the SOA. Another segment of birefringent fiber is traversed to reverse the delay between the TE and TM components. The polarized components then pass through a polarization controller (PC), which effectively recombines the two components by rotating the polarization state. The final PSI is traversed to control the polarization of the output pulse. If the PC rotates the polarization such that the pulse is not polarized along the propagation axis of the PSI, the pulse will be attenuated within the PSI and the resulting output will be a "0". If the polarization of the pulse and the propagation axis of the PSI are aligned, the pulse will pass through the PSI unhindered and the output will be a "1".

If a control pulse overlaps with the trailing pulse, the additional light (the control pulse) within the SOA will instigate a carrier population change within the SOA, and shift the phase of the delayed component. The phase shift imparted on the delayed component, via refractive index changes in the SOA, will alter the resulting polarization rotation via the PC. Thus, application of a control pulse is required to induced a phase shift so as to switch the output state (e.g. between a "1" and a "0").

As mentioned in Section 6.1, the passing of intense pulses through semiconductor devices creates both instantaneous and long-lived refractive index and gain changes [160]. Since the relaxation time of the long-lived nonlinearities is longer than the bit rate, these nonlinearities affect both polarization components roughly equally and are negligible [167]. The sub-picosecond nonlinearities are on a time scale that can affect both propagating polarization components, thus the delayed component is chosen to overlap with the control pulse [167]. Since both components experience the same SOA medium following passage of the control pulse, the output of the UNI will be the same state for a pulse that passes through the device either in the absence of a control pulse or following a control pulse.

6.3 Semiconductor Optical Amplifier Designs for the UNI

SOA design requirements for the UNI include polarization insensitivity, large confinement factors, and short recovery times. Polarization sensitivity deals with available transitions whereas the recovery time is governed by the number of carriers available to participate in the required transitions. Larger confinement factors are desired so as to obtain a higher internal efficiency, and concurrently an increase in achievable gain.

Polarization insensitivity is required in order for both polarization components to traverse the UNI without attenuation, such that each component effectively propagates through the same environment. Polarization selection is somewhat inherent in semiconductor materials due to the arrangement of the heavy- and light-hole valence bands (see Figure 6.4). The light-hole band is typically more sharply defined

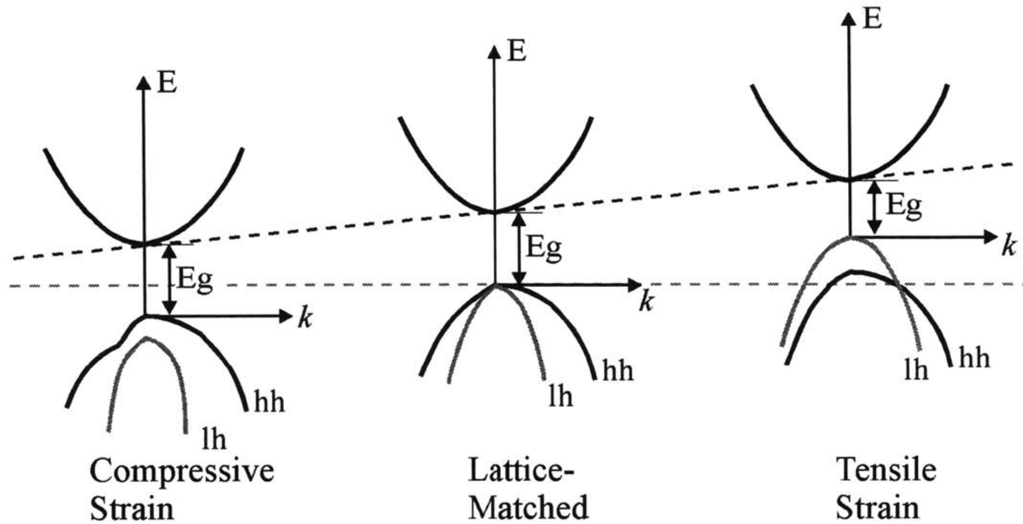

Figure 6.4 Diagram of strain effects on energy band arrangements in semiconductor materials. Diagram after [109].

and thus the states accessible for transition (at a specific energy) between the light-hole and conduction band are more restricted. The heavy-hole valence band is much broader and thus more transition states are available between the heavy-hole band and the conduction band for a given energy. Transitions involving the heavy-hole valence band corresponds to a TE-polarized state while transitions involving the light-hole valence band are TM-polarized [168]. For a SOA based on a double-heterostructure design, the active region is relatively polarization insensitive. Since both the light-hole and heavy-hole valence bands overlap in the absence of strain, both TE- and TM-polarized modes will be supported. However, due to the inherent sharpness of the light-hole valence band, a double-heterostructure device in not completely polarization insensitive.

With the introduction of strain into a semiconductor material, the heavy- and light-hole valence bands may be separated. For compressive strain, the heavy-hole to conduction band transition has the lowest energy transition. Likewise, for tensile strain, the light-hole to conduction band transition is the transition requiring the least amount of energy (see Figure 6.4 for a pictorial description). However, the introduction of strain into the active region of a double-heterostructure device can significantly damage the material

quality if the critical thickness of the strained layer is surpassed. One example of achieving polarization insensitivity in a double-heterostructure-type SOA is the use of strain-compensated layers within the waveguide core [170]. This device is not considered a quantum well-based device as the compositional difference between the two materials in the core is not drastic enough to preferentially confine carriers.

In most cases, quantum well-type structures are preferred over bulk or double-heterostructure devices due to the larger achievable gain per injected carrier [171]. However, quantum well structures are also not inherently polarization insensitive. In general, a quantum well is TE-polarized, as the first quantized valence band state is a heavy-hole band [168]. Common techniques for realizing polarization insensitivity within quantum well-based devices are alternating the strain of the quantum wells [i.e. 172] or strain-compensated quantum well regions [i.e. 173]. By alternating the valence band-conduction band transition, transitions to both the heavy-hole and light-hole are equally probable. An additional technique that has been used to realize polarization insensitivity is the addition of delta tensile-strained layers, a few monolayers thick, placed in quantum wells [174].

The confinement factor in a heterostructure-type device is governed by the severity of the index difference between the active region and the cladding region, and the area of the mode constrained within the active region. A large confinement factor is preferred in order to increase the number of carriers available for participation in the population dynamics required for refractive index changes. Methods used to increase the confinement factor are the use of double-heterostructure active regions (a large modal overlap) or multiple quantum well active regions. Although the confinement factor for quantum wells is smaller than that of double-heterostructures, the carrier efficiency attained via increased confinement outweighs the drop in the confinement factor.

The recovery time of the SOA is also of importance, in that the time required to recover from a π-phase shift will limit the repetition rate of the control pulse. As the control pulse is typically a clock pulse, repetition rate limitations can be detrimental to the performance of the UNI. Various methods exist for reducing the recovery times in semiconductors, including low temperature-grown material, bombardment (i.e. ion or proton), or simply device biasing. However, detrimental effects are inherent in all of the mentioned techniques. The use of low temperature-grown material to reduce carrier lifetimes has been successfully utilized in the development of semiconductor saturable absorber mirrors for realization of ultrashort-pulsed mode-locked lasers [121 and references within]. However, the introduction of non-radiative recombination centers inherent in low temperature-grown material is not a large concern for saturable absorber mirror structures. Likewise, lifetime reduction via bombardment schemes introduces non-radiative recombination centers. The presence of non-radiative recombination locations within a SOA structure effectively removes a portion of the carriers able to participate in the population dynamics

required to achieve the necessary refractive index changes. Thus, the use of low temperature-grown material and bombardment schemes to decrease carrier recovery times must be delicately balanced with the need for carriers available to induce refractive index changes. Furthermore, as both low temperature-grown and bombarded materials have atoms located in interstitial sites, the additional atoms located between the crystal lattice arrangement can introduce scattering centers. Thus, for the mode propagating through the SOA, the loss experienced by the light as it traverses the structure may be increased.

A simple increase in bias current to reduce the carrier recovery time is also a viable option. However, with an increase in bias comes an increase in amplified spontaneous emission (ASE). Since ASE is amplification of incoherent light, it effectively raises the noise floor thereby decreasing the signal-to-noise ratio following propagation through the SOA. Like the balance required for utilization of low temperature-grown or bombarded materials, a balance also exists when increasing the bias of a SOA. Also of concern in a high bias regime is the onset of Auger recombination. In many ways, Auger recombination is apparent in a manner similar to intentionally introduced non-radiative recombination centers; injected carriers are removed from the population dynamics via non-radiative recombination.

The need to both decrease the carrier lifetime and simultaneously increase the number of available carriers to induce refractive index changes is driven by the need to decrease the length of the SOA. Typical device lengths used in recent switching demonstrations are 0.5 to 1.0 mm. Propagation through a 0.5 mm long device requires ~5 ps; thus, for an SOA of this length, the time required for a pulse to be switched, from introduction to the UNI through to the output, is at least 5 ps. Likewise, since the two polarization components may not simultaneously pass through the SOA (in the UNI arrangement), the polarization components are required to be spaced by at least 5 ps, requiring the data pulses to be separated by more than 5 ps. If the data pulse separation is ~7 ps, for example, the input data rate is limited to ~143 Gbps. Reduction of the length of the SOA will allow a significant increase in both the input data rate and the switching rate of all-optical switching techniques.

6.3.1 Current SOA Designs

The current SOA structure being investigated was designed by J.P. Donnelly at Lincoln Laboratory, and is shown in Figure 6.5. Because of the 50 nm active region, the designed device possesses very little polarization preference [168]. In order to support only a single TE and TM mode, the ridge width for the structure in Figure 6.5 must be 2.5 μm. Three-dimensional modal simulations for the structure have been performed for $\lambda = 1.55$ μm using a mode solver developed by Optiwave [169]. Shown in Figure 6.6(a) is the supported TE mode electric field intensity as calculated by the 3-D mode solver. Figure 6.6(b) and (c) are the modal profile intensity cross-sections graphed with the refractive index profile of the structure. The

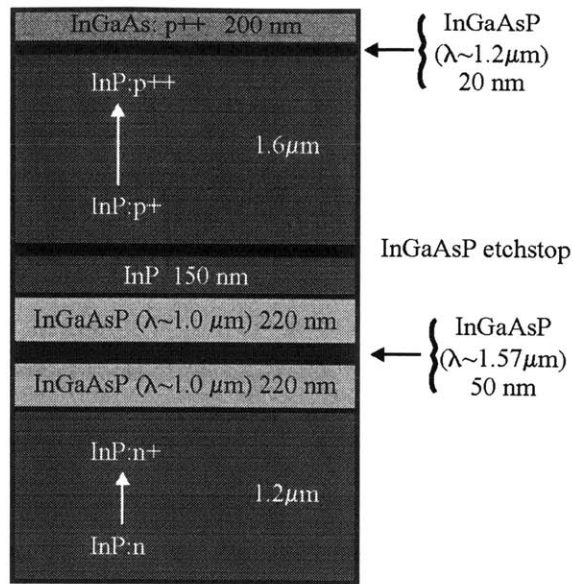

Figure 6.5 Schematic of the current SOA structure under development.

corresponding confinement factors, calculated using an overlap integral approach, are ~85% horizontal mode confinement and ~8.5% vertical mode confinement. The resulting total mode confinement (horizontal multiplied by the vertical confinement) for the TE mode is ~7.2%.

Simulations were likewise performed for the TM mode, with the results displayed in Figure 6.7. Upon close inspection of Figure 6.7(c), the TM mode is less intense within the active region than within the InGaAsP cladding regions. Smaller discontinuities are also visible at the other locations of refractive index changes, such as the changes between the InP electrical confinement regions and the InGaAsP cladding regions (at y ~ 0 and ~0.5 μm) as well as both InP-InGaAsP etch-stop interfaces.

For a TE mode, the electric field and its derivative must be continuous across an interface. The tangential magnetic field, however, is not necessarily continuous. For a TM mode, the magnetic field must be continuous across an interface, but not necessarily the electric field. The discontinuity observed in the modal vertical cross-section of Figure 6.7(c) is attributed to the TM mode electric field discontinuity. One possible means of decreasing the severity of the electric field discontinuity is to reduce the index difference between the active and cladding regions. As the gain dynamics of the SOA take place within the 50 nm active region, is it very important to minimize the discontinuity such that the most intense portion of the TM mode overlaps more strongly with the active region than the cladding regions so that the desired phase change will be appropriately instigated. The calculated confinement factors from Figure 6.7(b) and (c) are

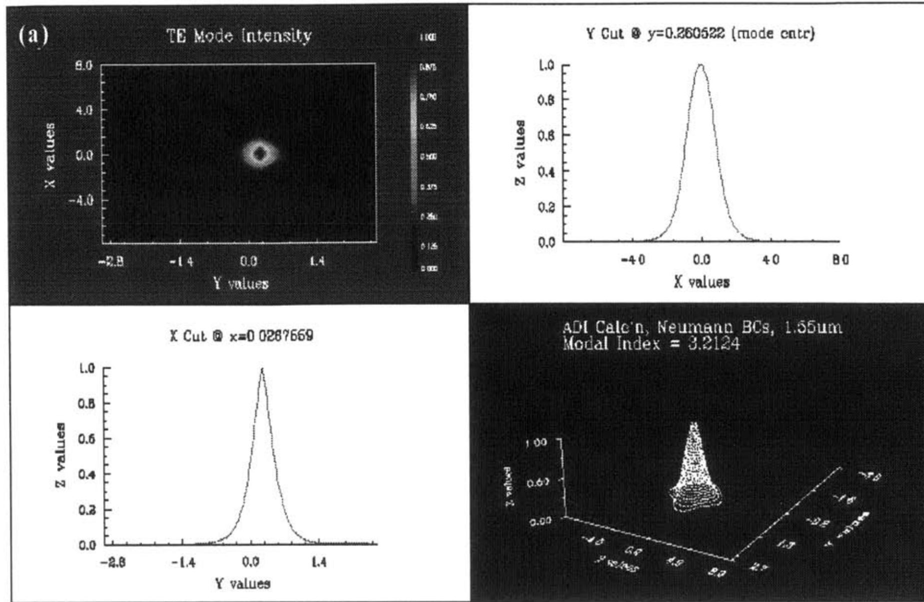

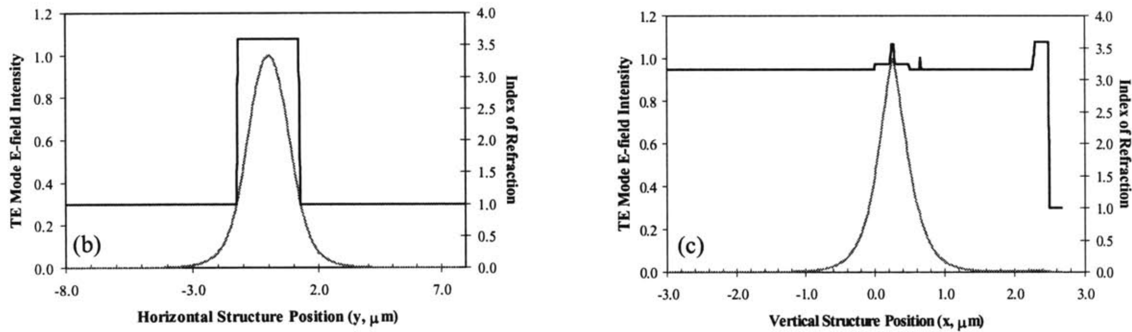

Figure 6.6 (a) 3-D mode solver solution for a TE mode supported in a 2.5 μm ridge SOA structure (structure depicted in Figure 6.5). Depicted is the electric field intensity. (b) Horizontal and (c) vertical cross-section of the TE mode intensity graphed along with the index profile of the structure.

~90% horizontal confinement and ~5.6% vertical confinement. The resulting total confinement for the TM mode is ~5%.

Although not as evident in the intensity profiles, a portion of both the TE and TM modes extends to the InGaAs contact layer. Shown in Figure 6.8 is the amplitude of the vertical electric field cross-section for both the TM and TE modes. Extension of the supported modes to the contact layer significantly increases the loss that both modes will experience in propagation through the as-designed SOA structure. In order to reduce the loss, structural changes must be made to Figure 6.5. Possible changes include an increase in the thickness of the InP electrical confinement layer or an increase in the refractive index of the InGaAsP

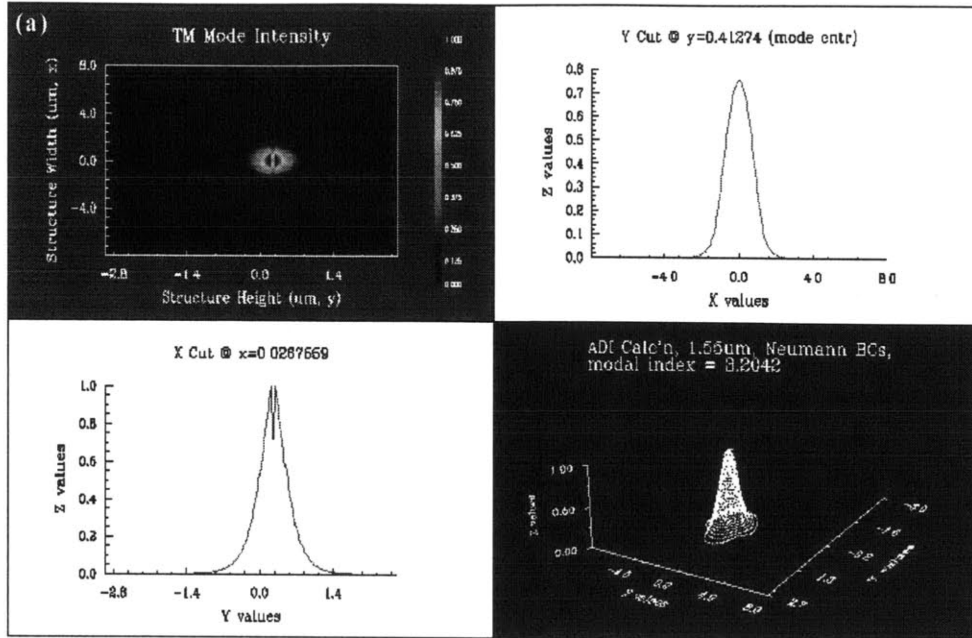

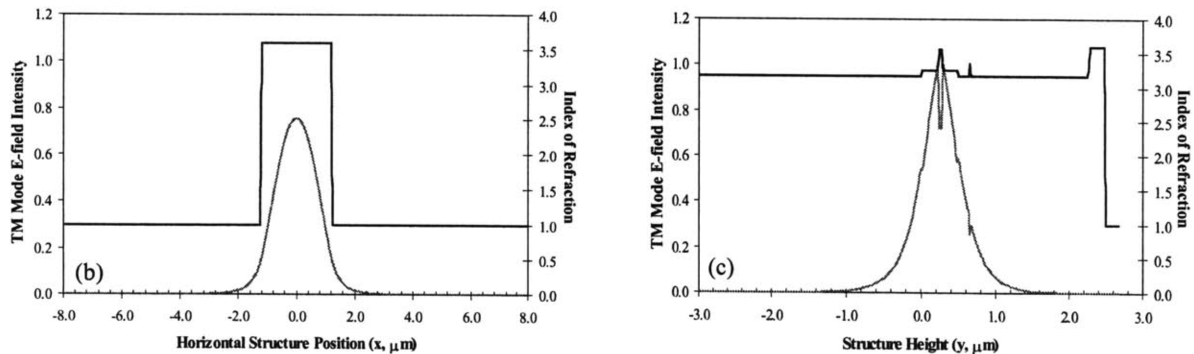

Figure 6.7 (a) 3-D mode solver solution for a TM mode supported in a 2.5 μm ridge SOA structure (structure depicted in Figure 6.5). Depicted is the electric field intensity. (b) Horizontal and (c) vertical cross-section of the TM mode intensity graphed along with the index profile of the structure.

optical cladding layer (adjacent to the active region). Increasing the thickness of the InP layer will effectively place the InGaAs contact layer a farther distance from the supported mode. Increasing the refractive index of the InGaAsP material adjacent to the active region will confine a larger portion of the mode in the vicinity of the active region, effectively reducing the energy present in the tails of the mode. However, both mentioned structural alterations must be adjusted while keeping in mind (i) that an increase in the InP region may subsequently increase the resistance of the device and (ii) that an increase in the

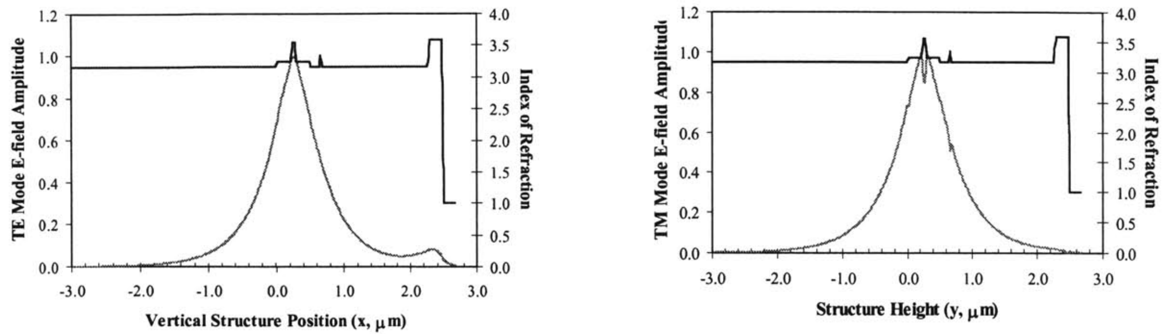

Figure 6.8 Diagrams of the simulated electric field amplitude for the TE mode and TM mode in the SOA structure of Figure 6.5.

InGaAsP cladding region index may decrease the modal confinement factors. Additional double-heterostructure SOA designs (also by J.P. Donnelly) being considered are depicted in Figure 6.9.

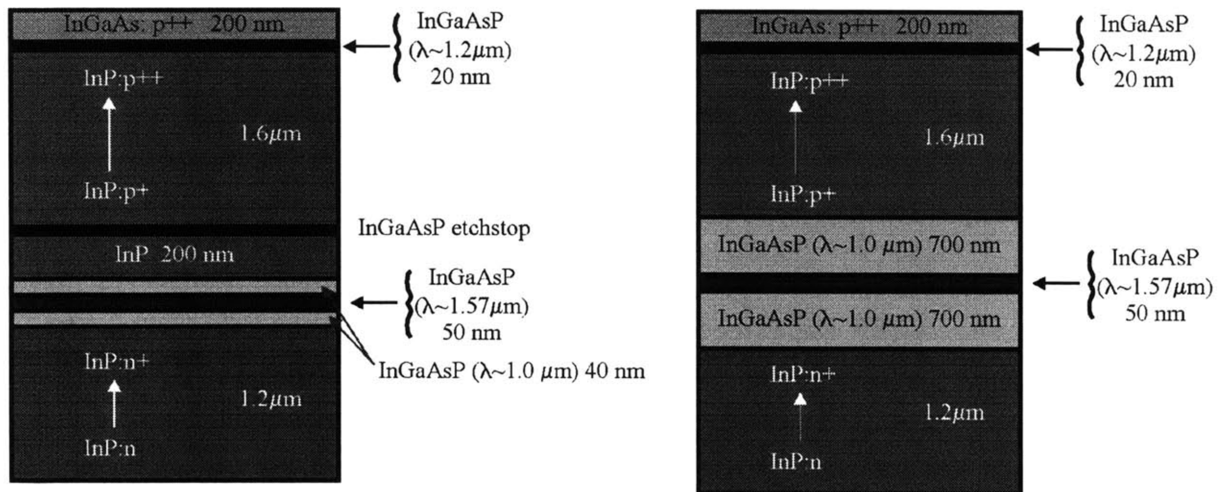

Figure 6.9 Schematics of other double heterostructure SOA designs being considered.

Status of SOA Fabrication

The development of semiconductor optical amplifiers for implementation in the ultrafast nonlinear interferometer is in the early stages. Regarding SOA fabrication, the InGaAsP materials are currently being calibrated via GSMBE for the structure shown in Figure 6.5. Simultaneous calibration of dopants and

achievable dopant concentrations is being accomplished by A. Markina in Prof. Leslie A. Kolodziejski's laboratory at MIT. Of concern at this time is the calibration of the InGaAsP ($\lambda \sim 1.57$ μm) for the active region of the SOA. Thus far, calibration of the active region has proven to be quite difficult. Specifically, PL spectra from calibration layers contain a feature located at $\lambda \sim 1.55$ μm, for compositions approaching that of $In_{(1-x)}Ga_xAs$ ($x = 0.47$). The 1.55 μm feature is similar to that observed in InGaAsP layers found to lie within the InGaAsP miscibility gap (see Section 2.2.5). Also, obtaining the desired arsenic concentration within the InGaAsP layer has as yet been unattainable. A more detailed investigation into the deposition parameters for InGaAsP ($\lambda \sim 1.57$ μm) is needed in order to realize the SOA structures.

6.3.2 InP-Based Monolithic Integration of the UNI

Development of an SOA for the ultrafast nonlinear interferometer is coupled to the long-term goal of monolithically integrating the UNI in the InP materials system. The single arm geometry is suitable for monolithic integration since two interferometric arms do not need to be accurately balanced, and only a single SOA is required.

For realization of a monolithically integrated UNI, waveguide-based sections to induce a polarization separation, to delay a polarization component, and to reverse the latter two actions, must be developed. Use of a Y-junction power splitter (typically a 50:50 power splitter), to attain polarization splitting [i.e. 175] is one viable method. By lowering the effective refractive index of one of the branches (via bombardment, quantum well mixing, or deposition of a low index substance on one branch), the TM and TE modes will prefer to traverse separate paths. The use of mode-matching via multiple Y-branches is also a technique that has been demonstrated for realization of polarization separation [i.e. 176]. Although the mentioned techniques have been demonstrated, the required real-estate is quite large. Use of a two-dimensional photonic bandgap structure may provide a more compact polarization splitting section. Implementation of a delay between the polarization components may be implemented via a path length difference in either a waveguide or a photonic bandgap. The use of a photonic bandgap structure may allow the delay to be realized within a smaller footprint. Reversal of the delay, as well as recombination of the polarization components, will most likely be performed in the opposite manner of the initial separation.

With regard to epitaxy, integration of the waveguide/photonic bandgap sections and the SOA must be considered. Since the waveguide sections must be transparent to both the control and signal pulses, the waveguide core must have a bandgap significantly larger than that of the SOA. However, to minimize loss at the waveguide/SOA interfaces, the mode profiles in the waveguide and SOA must be similar. Thus, proper design of the waveguide and SOA is required. Furthermore, investigation of GSMBE on large

dimensioned structures (i.e. deposition of the waveguide following RIE definition of the SOA) and selective-area deposition must be accomplished for realization of a monolithically integrated UNI.

7

Summary and Future Work

7.1 Accomplishments

In summary, the development of components for all-optical communication networks is necessary in order to support the continued increase in communication traffic. Although Wavelength Division Multiplexing (WDM) has been successfully implemented in order to increase the capacity of the current communication system, the limits of this technique are not yet clear. Increasing network data rates via all-optical Time Division Multiplexing (TDM) is also a viable technique actively being pursued in research laboratories. As each technique has advantages and disadvantages, it is highly likely that the future all-optical communication networks will consist of a marriage of WDM and TDM.

With the more rapid data rates, obtained either by decreasing the wavelength channel spacing or the bit spacing, the demands placed on the network components for generation and processing (i.e. routing and switching) of the ultrafast aggregate data rates brings fabrication issues to the forefront. Within the frequency domain, decreased channel spacing requires optical sources and filters with specific linewidth and wavelength characteristics. For high repetition rates, optical sources capable of generating pulses at ultrafast bit rates are required.

Investigation of the procedures required to realize high quality epitaxial overgrowth of refractive index modulations, applicable to DFB lasers as well as wavelength-selective filters, has been accomplished. An extensive review of sawtooth-patterned index modulation overgrowth has been conducted, and reveals that high quality overlayers are obtainable, provided an appropriately prepared initial surface is created. Alternatively, rectangular-patterned surfaces also provide a variation in refractive index, but do not require mass transport or pre-growth modification of the grating profile for growth of a high quality overlayer. Repeatable and well-controlled surface preparation has been conducted using a low temperature (~200°C)

atomic hydrogen-assisted surface cleaning procedure to remove the native oxide and preserve the as-fabricated rectangular-patterned surface. Extensive investigation of the index modulations, both exposed and buried, has been carried out using triple axis x-ray diffractometry. Subsequent analysis of (In,Ga)(As,P) structures reveals that the material residing within the grating region accommodates the lattice parameter differences in an equal and opposite orthorhombically strained manner (for relatively close lattice-matched conditions). Additionally, the overlayer material deposited on top of the grating region experiences an orthorhombic lattice distortion as a result of the buried grating. However, for the various structures investigated, the magnitude of the strain, both within and adjacent to the grating region, is very small and is not anticipated to significantly affect device performance. The initial investigations highlighted regarding compositional modulation for overgrown rectangular-patterned surfaces suggest that composition modulation is reduced for fully-preserved grating profiles, but is most likely still present for overlayers containing large concentrations of low mobility (small diffusion length) atoms (i.e. Ga and As). Investigation of defect generation within the grating region of the rectangular-patterned overgrown structures has not been accomplished to date, however the number of defects is anticipated to be small due to the equal and opposite elastic compliance of the InP and InGaAs(P) materials.

The development of fiber lasers capable of generating pulse trains suitable for TDM networks has also been investigated. Passive mode-locking via semiconductor saturable absorber mirrors was the chosen method for pulse generation. The designed saturable absorber mirrors incorporate a GaAs/AlAs DBR and an InP-based absorber region. Deposition of the structures was accomplished in two parts; the DBR was deposited and characterized prior to deposition of the InP absorber region. An atomic-hydrogen surface cleaning process (similar to that used for deposition on rectangular surface corrugations) was utilized for removal of the native oxide prior to the InP/InGaAs regrowth. Ultrafast optical characterization was accomplished via dynamic differential reflectivity measurements as well as saturation fluence measurements. Analysis of the structures under conditions attainable within mode-locked laser systems reveals the presence of two-photon absorption and free carrier absorption. Detailed analysis of both effects, as well as the influence on mode-locked laser cavities, was investigated. The presence of two-photon absorption is predicted to increase the stability regime of the laser cavity against Q-switched-mode-locking.

Preliminary investigation of Semiconductor Optical Amplifiers (SOAs) for implementation in all-optical interferometric switching schemes has also been addressed. Requirements placed on the SOA for implementation in a single-arm ultrafast nonlinear interferometer include polarization insensitivity, large modal confinement, and rapid recovery times. Beam propagation modeling of the designed structures

has been performed, with respective calculations of the confinement factors. Preliminary material calibration has also been accomplished in preparation for device fabrication.

7.2 Suggestions for Future Work

As the topics addressed in this thesis are relevant to the next generation(s) of communication networks, there is much work that may be continued.

7.2.1 Overgrowth of Rectangular-Patterned Refractive Index Modulations

As mentioned in Chapter 4, the defect generation within the overlayer deposited on rectangular-patterned index modulations has not yet been investigated. Analysis of this aspect, via Transmission Electron Microscopy (TEM) would be very beneficial. From the pictorial model presented in this thesis, it is expected that the generation of defects during overlayer nucleation and deposition on preserved rectangular gratings is small since the overlayer growth is dominated by (100) growth fronts. However, techniques such as TEM are required to confirm this speculation. Furthermore, a detailed study of the manner in which material is deposited within the grating trenches is needed to confirm (or dispute) the rectangular-patterned grating overgrowth model presented.

Not only is deposition on rectangular-patterned gratings applicable to devices requiring buried index contrasts, but deposition on rectangular corrugations is also applicable to quantum wire- and quantum dot-based devices. Given the speculated increase in uniformity of overgrown rectangular-patterned gratings (as opposed to sawtooth-patterned gratings that must be subjected to mass transport prior to overgrowth), realization of highly uniform quantum wire or quantum dot regions is probable.

7.2.2 Development of Semiconductor Saturable Absorber Mirrors

The successful implementation of semiconductor saturable absorber mirrors in fiber-based laser cavities suggests that further development and tailoring of saturable absorber mirrors would be fruitful. Early saturable absorber designs are currently being implemented in a Cr^{4+}:YAG laser cavity. The analysis of the mode-locking regime and the saturable absorber mirror structure, as well as further tailoring of the absorber mirror for this cavity, is desirable. Investigation of proton bombarded absorber mirror structures has just begun, with the hope of implementing the bombarded structures in fiber laser systems. Design variations to induce more, or less, two-photon absorption for increased stability of various laser cavities has also just begun, and can be further developed.

Fabrication of a broadband semiconductor saturable absorber mirror would be highly favorable, not only from a materials and fabrication point of view, but also from an implementation angle. The flexibility obtained with a broadband DBR, with respect to generation of ultrashort pulses, is highly sought after. With the realization of ultrashort pulses, i.e. in a Ti:sapphire or Cr^{4+}:YAG laser cavity, significant flexibility is attained in terms of tunability, allowing detailed exploration of devices (i.e. photonic bandgap devices) as well as spectroscopy-type measurements.

7.2.3 Ultrafast Nonlinear Interferometer

In addition to continued development of semiconductor saturable absorber mirrors, the monolithic integration of the Ultrafast Nonlinear Interferometer (UNI) will be investigated. Integration of the UNI in InP-based materials would not only increase the manufacturability, but would also reduce the size of the device to a few centimeters. Components of the UNI to be designed and fabricated in InP materials include, polarization splitters and combiners, as well as the integration of the waveguides with the SOA. An important design issue is the minimization of loss at the necessary waveguide-SOA interfaces, thus the mode profiles within both the SOA and the waveguides must be nearly identical. Extensive design and beam propagation modeling is required prior to device fabrication. One method of incorporating a polarization splitting region may be the use of a two-dimensional photonic bandgap structure.

Appendix A

Triple Axis X-ray Diffractometry and Reciprocal Space Mapping

The use of x-ray diffractometry for analysis and determination of crystallographic structures is a well developed, and heavily utilized, technique. For analysis of semiconductor materials, x-ray diffractometry is probably the single-most relied upon technique to determine the material quality. Other techniques, such as Transmission Electron Microscopy (TEM), may be utilized to provide comparable information, but at the expense of time-consuming (and destructive) sample preparation. A brief overview of diffraction theory and the resulting implementation via double axis and triple axis x-ray geometries will be discussed. Generation of reciprocal space maps via triple axis x-ray diffractometry, and the subsequent analysis, will also be addressed.

A.1 Diffraction Theory

The underlying mechanism in diffraction of any type is the interference of radiation as it traverses a material or structure. Constructive interference occurs if the radiation diffracted from a single (or multiple) interface(s) is in phase. For radiation λ, incident on a periodically layered medium (comprised of either alternating material layers or an atomic arrangement) with period d, at some angle θ, constructive interference and thus coherent diffraction of the incident radiation will occur when

$$n\lambda = 2d\sin\theta \qquad \text{Eq. (A.1)}$$

Eq. (A.1) is known as Bragg's Law; depicted in Figure A.1 is the graphical representation. For coherent diffraction from multiple layers, the path length difference, ABC, must equal $n\lambda$. In a crystallographic

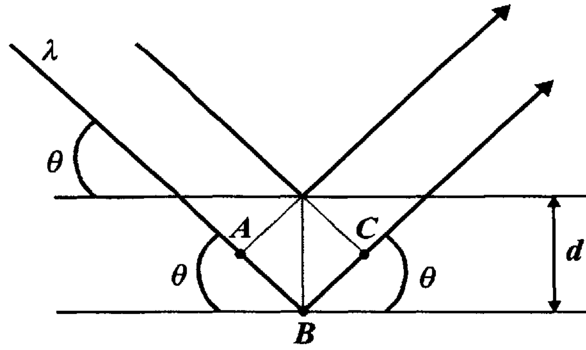

Figure A.1 Geometric representation of Bragg's Law. The path length difference between two layers is *ABC*.

structure, the multiple diffraction planes are defined by the atomic planes within the crystal, and the condition for coherent diffraction is satisfied if $\theta = \theta_B$, the Bragg angle.

A.1.1 Reciprocal Space Formalism

Inherent in any diffraction scenario, be it transmission-diffraction through slits or reflection-diffraction off of atomic planes, is the relationship between the actual structure being probed and the resulting diffraction pattern. This relationship may be modeled by a Fourier Series [31,177], however since intensity is detected, all phase information is lost. Thus, analysis of the diffraction pattern can be approximately related to the actual structure via a Fourier series transformation. The Fourier space represented by the diffracted pattern is termed "reciprocal lattice space" and is inversely proportional to real space [178].

In reciprocal space, given a plane wave incident on a crystal structure, traveling along a vector defined by r, the plane wave can be defined as

$$E = E_o e^{i(k_i \cdot r)} \qquad \text{Eq. (A.2)}$$

where k_i is the wave vector whose magnitude is $2\pi/\lambda$. (Note, in crystallography, the wave vector is not scaled by the factor 2π. Thus, 2π is excluded from formulas in the remainder of the text.) Following diffraction from the crystal structure, the incident radiation will experience a phase shift

$$e^{i(k_e - k_i)r} = e^{i(G \cdot r)} \qquad \text{Eq. (A.3)}$$

where k_e is the diffracted wave vector and G is the path length difference between the incident and diffracted wave vectors [178]. Shown in Figure A.2. is a geometrical depiction of G. The magnitude of each k-vector is $1/\lambda$; the sphere formed with a radius of $1/\lambda$ is known as the Ewald sphere [177, 178]. Note, Bragg's law is satisfied for $|G| = n/d$, since $|k_e - k_i| = (2/\lambda)\sin\theta_B$.

Reciprocal lattice points are related to the real space lattice by the following equations:

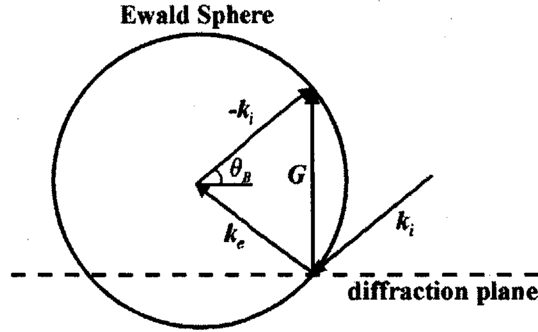

Figure A.2 Geometrical representation of the Ewald sphere construction.

$$a'_1 = \frac{a_2 \times a_3}{a_1 \cdot (a_2 \times a_3)}, a'_2 = \frac{a_3 \times a_1}{a_2 \cdot (a_3 \times a_1)}, a'_3 = \frac{a_1 \times a_2}{a_3 \cdot (a_1 \times a_2)} \quad \text{Eq. (A.4)}$$

where a_i' defines the reciprocal lattice vectors and a_i designates the real space lattice vectors [177]. The reciprocal lattice vector, G, defined in terms of the reciprocal lattice axes is

$$G = ha'_1 + ka'_2 + la'_3 \quad \text{Eq. (A.5)}$$

where hkl are the Miller indices [31].

Coherent diffraction is obtained if the incident vector, k_i, and the crystal specimen are aligned such that diffraction from the atomic planes interferes constructively and a vector G is defined. Recall, G only exists between reciprocal space lattice points; thus, proper alignment of the sample and k_i result in the intersection of the Ewald sphere with reciprocal lattice points. A geometrical depiction of the latter statement is shown in Figure A.3(b). Rotation of k_i with respect to the atomic planes results in rotation of the Ewald sphere in reciprocal space. Shown in Figure A.3(a) is alignment of k_i (with respect to the sample) in which the condition for coherent diffraction is *not* satisfied.

Given a specific semiconductor material and a fixed wavelength of incident radiation, a diagram in reciprocal space can be generated depicting the reciprocal lattice points that may be probed. Shown in Figure A.4 is an example of such a diagram for (100) silicon. The reciprocal lattice points in the shaded areas are unreachable due to geometric limitations (i.e. required incident angle is behind surface of sample) or location outside of the Ewald sphere (as defined by the incident radiation, λ).

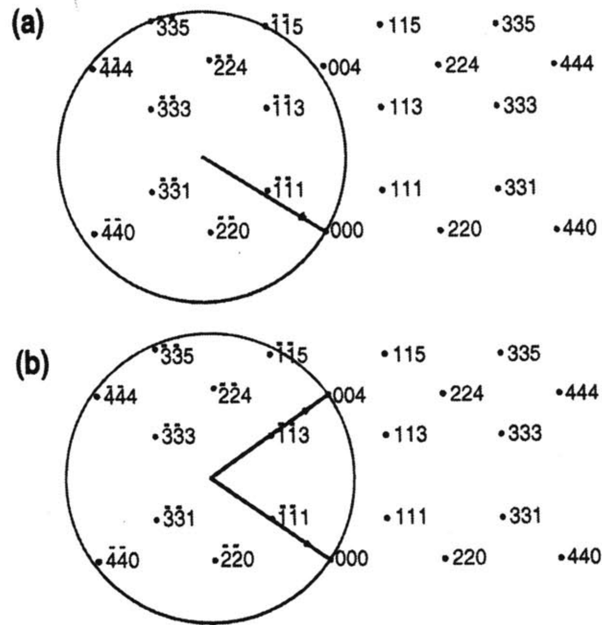

Figure A.3 The Ewald sphere constructed in reciprocal space. The (400) diffraction conditions are not satisfied in (a). The (400) diffraction conditions are satisfied in (b). Figure from [177].

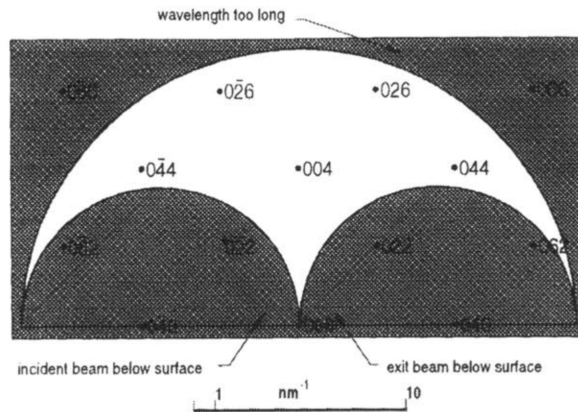

Figure A.4 Diagram of available diffraction conditions for (100) Si.

A.2 X-ray Diffractometry

Radiation sources typically used for diffraction analysis of semiconductor crystallographic structures are located within the x-ray spectrum. Specific wavelength requirements are that the incident radiation be

able to penetrate the crystal, yet not be significantly shorter than the atomic spacing so as to hinder resolution [31]. Typical sources used in diffractometry systems for semiconductor analysis are the x-ray $K\alpha$ lines from a copper target [177], which have a characteristic wavelength of 1.54 Å.

In practice, the radiation incident on a sample in not a pure, single wavelength delta function, but rather comprised of a narrow range of wavelengths. Thus, inherent in the measurement is linewidth broadening of the diffracted intensity due to the width of the source radiation. The incident radiation width can be reduced via conditioning prior to reaching the specimen of interest, and will be discussed in more detail in Section A.2. Following [31], shown in Figure A.5 is a geometric depiction of diffraction with an

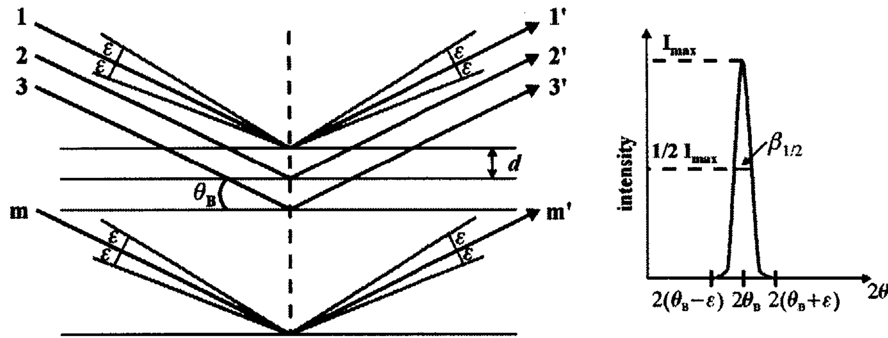

Figure A.5 Geometrical depiction of diffraction of an incident source having a linewidth $\beta_{1/2}$ due to an angular deviation, ε, from the Bragg condition. Figure from [31].

incident source having a width with angular deviation ε from the Bragg condition; the inset is a depiction of the resulting diffracted intensity and corresponding linewidth ($\beta_{1/2}$). As the thickness of the analyzed crystal structure is increased, the probability of destructive interference along the periphery (or wings) of the diffracted beams increases. For thin crystal layers, the probability of complete destructive interference of the diffracted beam periphery is low, and thus the resulting linewidth of the diffracted intensity will increase as the analyzed layer thickness decreases. In reality, an incident x-ray beam will not fully penetrate an infinitely thick sample due to scattering and absorption of the incident beam. Thus, even the diffracted intensity from an infinitely thick sample will be inherently broadened. A thorough analysis of the diffraction geometry with an incident source having a finite linewidth results in the definition of $\beta_{1/2}$, the linewidth of the diffracted intensity as a function of the analyzed layer thickness, D:

$$\beta_{1/2} = \frac{0.9\lambda}{D\cos\theta_B} \qquad \text{Eq. (A.6)}$$

Eq. (A.6) is known as the Scherrer formula [31]. Although Eq. (A.6) may not be applied to high resolution x-ray diffraction measurements, the inverse relationship between $\beta_{1/2}$ and the layer thickness is still valid.

The most straight-forward diffraction measurements are of the symmetric variety, in which the incident and exiting angles, with respect to the sample surface, are identical (see Figure A.6). For (100)-

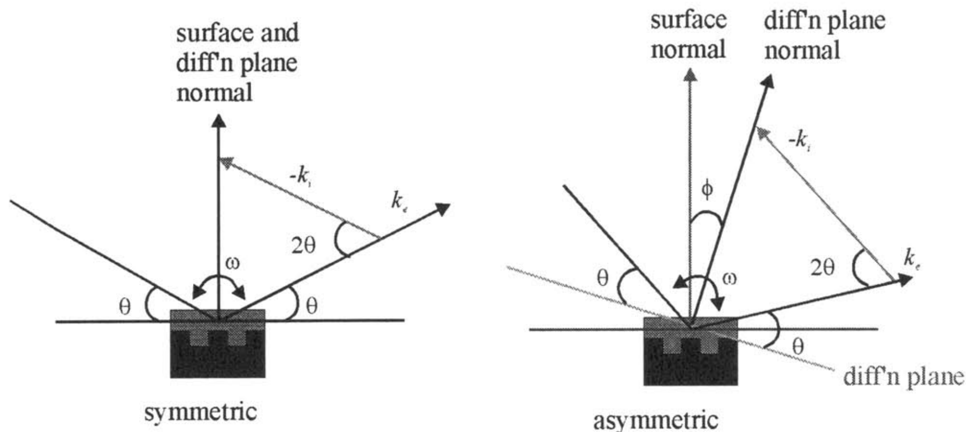

Figure A.6 Basic diffraction geometries for symmetric and asymmetric arrangements.

oriented semiconductor samples, symmetric measurements encompass diffraction from (*h*00) planes. The most common symmetric diffraction condition for (100)-oriented zincblende and diamond semiconductor samples is the (400) geometry. From symmetric measurements, information about the perpendicular lattice constant, a_z, can be obtained. As the incident x-ray beam traverses the crystal mostly in large part along the *z*-direction, a_z is accurately probed. Additional information obtainable from symmetric diffraction measurements includes lattice plane tilt. For a sample experiencing curvature or multiple lattice cell orientations, the varying perpendicular lattice parameters will satisfy multiple Bragg conditions (i.e. constructive interference will occur for more than one incident angle).

In order to probe the parallel lattice constants, a_x and a_y, in conjunction with the perpendicular lattice constant (a_z), asymmetric geometries must be used. In asymmetric arrangements, the incident radiation is either entering or exiting at a shallow angle. Information about the parallel lattice parameters is obtained in these orientations since the incident radiation passes through the sample in a more horizontal orientation (as compared to symmetric geometries). Shown in Figure A.6 is the basic arrangement for symmetric and asymmetric diffraction measurements. One of the more common asymmetric geometries is the {422} orientation, since the incident (or exiting) angles are not so shallow as to degrade the diffracted intensity.

Asymmetric diffraction geometries typically suffer from a decrease in diffracted intensity. The intensity decrease is commensurate with the acuteness of the incident (or exiting) angle. Shown in Figure

A.7 is a depiction of symmetric diffraction for an incident beam with some width. In general, for

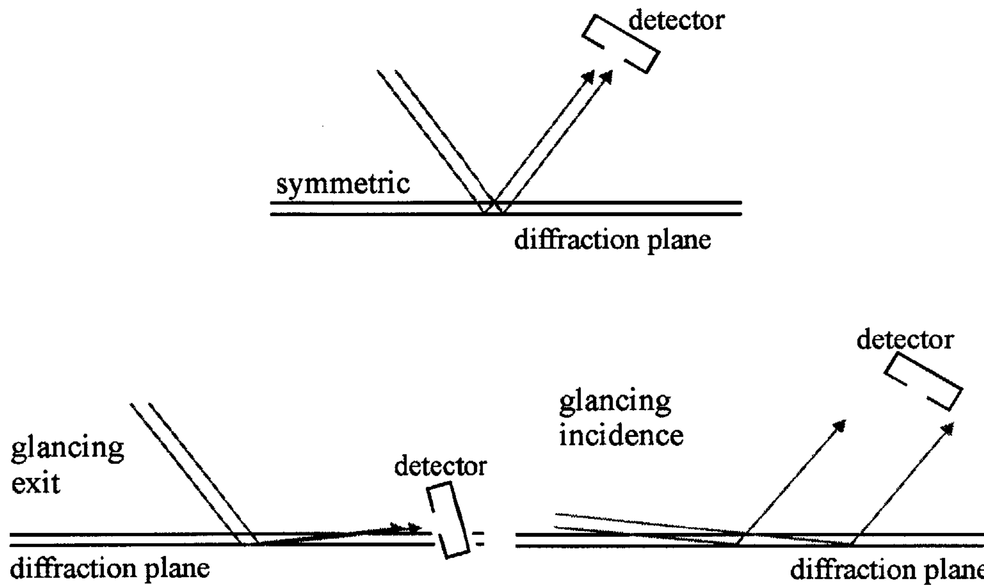

Figure A.7 Diagram of diffraction geometries.

symmetric diffraction geometries with low loss, the diffracted beam will be similar to the incident beam. Also, the near collimation of the diffracted beam allows the majority of intensity to be collected by the detector. For a glancing exit geometry, the incident beam will sample an area similar to that of a symmetric geometry. The exiting (diffracted) beam, however, will pass laterally through much more material than the incident beam (see Figure A.7). Although the diffracted beam may appear more collimated, the additional propagation through the sample due to the shallow exiting angle promotes both scattering and absorption of the diffracted beam prior to the beam fully exiting the sample, and thus less intensity will reach the detector. Also shown in Figure A.7 is a glancing incident geometry. Due to the acute entrance angle, the incident beam will sample an area much larger than that sampled by a symmetric or glancing exit geometry. Both scattering and absorption of the incident radiation will also occur during lateral propagation of the incident beam, decreasing the diffracted intensity. As a result of the large sample area, the diffracted beam will be very broad, and only a portion of the diffracted beam will be collected by the detector.

A.2.1 Double Axis X-ray Diffractometry

Double axis diffraction has become a common technique for the analysis of semiconductor materials, epitaxial layers, and structures. In many manufacturing lines, the analysis process is now automated. Shown in Figure A.8 is a generic high resolution double axis x-ray diffraction arrangement. The

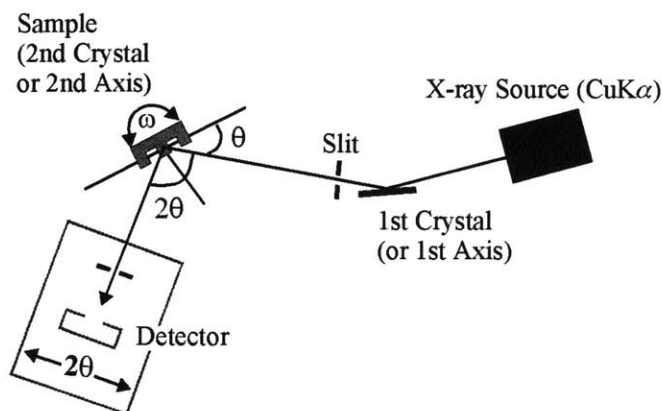

Figure A.8 General high-resolution double axis x-ray diffraction arrangement.

predecessor of double axis diffraction is high resolution double crystal x-ray diffraction. Double crystal diffraction involves diffraction of the incident x-rays off of a 1st crystal, which is typically the same material as the semiconductor sample being analyzed. After diffraction off of the sample, the x-rays are collected via a detector. By using the same materials for both the 1st and 2nd crystals, in a non-dispersive arrangement (adjacent diffraction directions are opposite in sense) as shown in Figure A.8, the obtainable resolution is quite high. However, it is not always practical to match the first crystal to the sample being analyzed. As a consequence of fixing the first crystal (i.e. such as choosing Si), the incident x-rays must be "conditioned", or diffracted more than once through the first crystal, in order to obtain comparable resolution to the use of identical crystals. Double crystal x-ray diffraction with unmatched crystals is termed double axis x-ray diffraction.

Beam conditioners provide a means of narrowing both the divergence and the wavelength spread of the incident x-ray beam [177]. For multiple diffractions from the same material, both the wavelength spread and divergence will be reduced, because destructive interference of the intensity that does not exactly satisfy the Bragg condition will be compounded. The reduction in both divergence and FWHM afforded by multiple diffractions from conditioning crystals effectively increases the resolution of the diffractometer. Depicted in Figure A.9 are rocking curves for an increasing number of diffractions from a (220) Si crystal. With a more conditioned incident x-ray beam, the sample is essentially probed by a more uniform x-ray

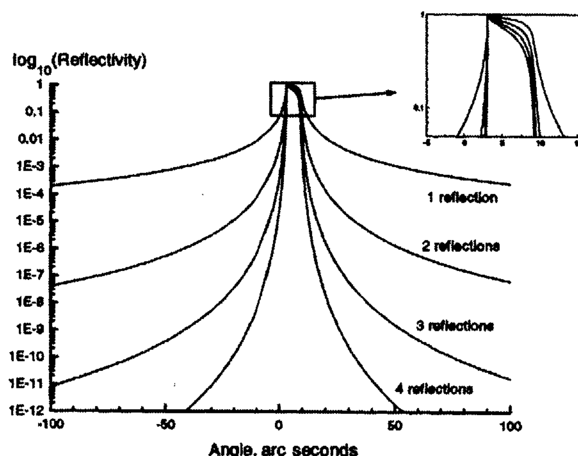

Figure A.9 Rocking curves depicting the increased beam conditioning obtained with an increase in the number of diffractions from a (220)-oriented Si crystal. Figure from [177].

beam, which subsequently minimizes the FWHM of the diffracted intensity. Also, since the sample is probed by a narrower beam, any effects due to substrate curvature, epilayer nonuniformity, etc. will be minimized in the resulting diffracted signal.

The basic geometry of a double axis diffraction arrangement is such that the 1st and 2nd axes are arranged in a non-dispersive configuration. In other words, diffraction from the two crystals is opposite in sense. In a non-dispersive configuration, the divergence of the diffracted beam is essentially corrected, whereas in a dispersive arrangement the divergence inhibits the measurement resolution. For example, with the Bede D^3 x-ray diffractometer at MIT in a double axis configuration, a dispersive arrangement (with the conditioning crystals in low resolution mode) results in a maximum resolution of ~ 20 arcsec (FWHM from a ~5 mm thick Ge sample). In a non-dispersive arrangement, the resolution increases to ~13 arcsec.

In general, measurements utilizing a double axis x-ray diffractometer are performed by rotating the sample (2nd crystal) about the Bragg angle for the given geometry, and simultaneously rotating the detector arm at twice the rate of the sample. This type of measurement is termed a rocking curve or a $\theta/2\theta$ scan. This technique is highly accurate for the measurement of perpendicular lattice parameters since differing lattice spacings will satisfy different Bragg conditions. In the rocking curve arrangement, layers with perpendicular lattice constants smaller than that of the substrate will satisfy larger Bragg angles; conversely, layers with perpendicular lattice constants larger than that of the substrate will be present at smaller Bragg angles. Mathematically, this is apparent [see Eq. (A.1)] as the Bragg angle and the atomic

spacing are inversely proportional. Typical scan times required for rather detailed measurements are usually less than an hour.

Shown in Figure A.10 is a reciprocal space representation of a double axis rocking curve. A $\theta/2\theta$

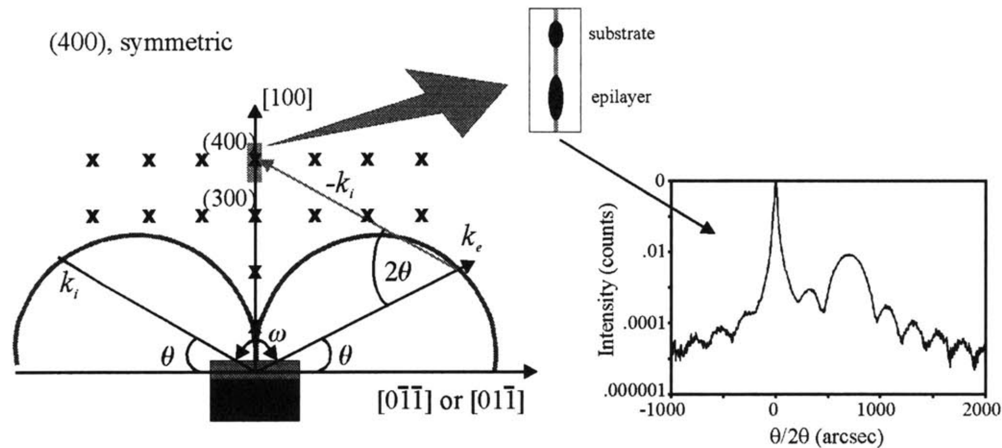

Figure A.10 Arrangement for a (400) θ/2θ scan in reciprocal space. An example of a double axis θ/2θ measurement of an InGaAsP ($x \sim 0.42$, $y \sim 0.81$) epilayer deposited on an InP substrate is shown to the right.

measurement effectively traces a portion of the Ewald sphere in reciprocal space parallel to the diffraction vector. Because in most cases the angular spread of the measurement is quite small, the probed portion of the Ewald sphere is assumed to be linear.

(400) Analysis of Epitaxial Layers

Symmetric rocking curves are essentially two-dimensional measurements that depict intensity as a function of the angle of the incident radiation. From a symmetric rocking curve, essentially only the perpendicular lattice parameter is probed. Other effects, such as lattice plane tilt, relaxation of the epilayer, surface curvature, etc., may be apparent via reduction of the diffracted intensity, but they are not able to be fully investigated using a 2-D symmetric technique since these effects alter both the perpendicular and parallel lattice spacings. Furthermore, as is apparent in Figure A.10, a symmetric rocking curve of a (100)-oriented crystal analyzes only the reciprocal space parallel to [100].

Shown in the inset of Figure A.10 is a (400) High Resolution Double Axis X-ray Diffraction (HRDAXD) rocking curve of an InGaAsP layer deposited on a (100) InP substrate. As the InP substrate is the crystal to which deposited layers are referenced, the $\theta/2\theta$ axis is typically normalized to the substrate peak. From the inset of Figure A.10, the epilayer is ~715 arcsec tensile-strained with respect to the InP

substrate. Apparent in the HRDAXD measurement is the presence of multiple periodically spaced features; these features are referred to as Pendellösung fringes (or thickness fringes) and are a function of the epilayer thickness. The oscillations are caused by the finite thickness of the epilayer. The period of the Pendellösung fringes is inversely proportional to the epilayer thickness, and thus layer thickness can be determined:

$$t = \frac{\lambda \sin\theta_B}{\Delta\theta \sin 2\theta_B} \qquad \text{Eq. (A.7)}$$

[179], where θ_B is the Bragg angle of the substrate and $\Delta\theta$ is the difference between the Pendellösung features.

As the distance between the substrate peak and the epilayer peak in (400) HRDAXD rocking curves is related to the difference in perpendicular lattice constants, both a_z and the associated biaxial strain, ε_z, of the InGaAsP can be determined from the measurement. The change in lattice spacing with respect to the substrate lattice parameter is derived from Bragg's law,

$$\frac{\Delta a_z}{a_{sub}} = \frac{\sin\theta_B - \sin(\theta_B + \Delta\theta)}{\sin(\theta_B + \Delta\theta)} \cdot \frac{\cos\phi}{\cos(\phi + \Delta\phi)} \approx -\Delta\theta \cot\theta_B = \varepsilon_z \qquad \text{Eq. (A.8)}$$

where $\Delta\theta$ is the angular distance between the substrate Bragg peak and the epilayer Bragg peak and ϕ is the angle between the surface normal of the sample and the diffraction vector. Simplification of Eq. (A.8) is accomplished via the small angle approximation ($\Delta\theta \sim 0$), which is valid for typical Bragg peak separations in rocking curve measurements of nearly lattice-matched semiconductor materials. Using Eq. (A.8), the strain in the perpendicular lattice parameter for the InGaAsP epilayer of Figure A.10 is $\sim -5.62 \times 10^{-3}$.

Asymmetric Analysis of Epitaxial Layers

Asymmetric diffraction analysis of epilayers reveals information about both the parallel and perpendicular lattice constants, as previously mentioned. Shown in Figure A.11 is a depiction of the area in reciprocal space probed by an asymmetric measurement (i.e. a {422} rocking curve). As is apparent from the figure, both the lattice parameter along [100] and $[0\bar{1}\bar{1}]$ or $[0\bar{1}1]$ are probed. (The directions quoted are those applicable to (100) InP, however the exact directions are dependent on the orientation of the sample being investigated.) Thus, analysis of rocking curves in asymmetric geometries must incorporate aspects of both dimensions.

The strain in the perpendicular lattice constant is determined via simplification of Eq. (A.8).

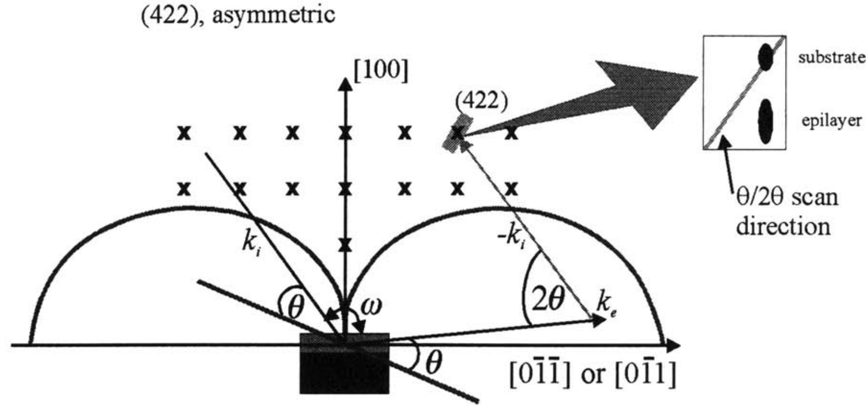

Figure A.11 An asymmetric {422} θ/2θ scan depicted in reciprocal lattice space.

$$\frac{\Delta a_z}{a_{sub}} = -\Delta\theta\cot\theta_B + \Delta\phi\tan\phi = \varepsilon_z \qquad \text{Eq. (A.9)}$$

and the parallel lattice constant, a_x or a_y, via

$$\frac{\Delta a_{x,y}}{a_{sub}} = \frac{\sin\theta_B - \sin(\theta_B + \Delta\theta)}{\sin(\theta_B + \Delta\theta)} \cdot \frac{\sin\phi}{\sin(\phi + \Delta\phi)} \approx -\Delta\theta\cot\theta_B - \Delta\phi\cot\phi = \varepsilon_{x,y} \qquad \text{Eq. (A.10)}$$

using the small angle approximation for $\Delta\theta$. Typically, a more accurate value for the strain (or lattice constant) of the epilayer is obtained by taking two asymmetric measurements, rotated 180° with respect to each other. The lattice constant of interest is then calculated from each measurement, and the average of the two calculated numbers is close to the actual lattice constant of the material of interest.

A.2.2 Triple Axis X-ray Diffractometry

Triple Axis x-ray Diffractometry (TAD) is, as the name indicates, similar to double axis x-ray diffractometry with the addition of a third axis. As with the double axis geometry, the first and second crystals (or axes) are the beam conditioning crystal(s) and the sample, respectively. The third axis is an additional crystal that further conditions the x-ray beam diffracted from the sample, and effectively increases the resolution of the measurement by further constraining the acceptance angle of the detector. Shown in Figure A.12 is a generic diagram of a TAD system.

For data presented in this thesis, three TAD systems were utilized. The majority of the TAD data was generated using a Bede D^3 diffractometer at UCLA (see Figure A.13); this diffractometer has an x-ray tube source for generation of CuKα lines for the incident x-ray beam, (111)-oriented Si beam-conditioning crystals, and a (220)-oriented Si analyzer crystal. The advantage of the (111)-oriented conditioning crystals

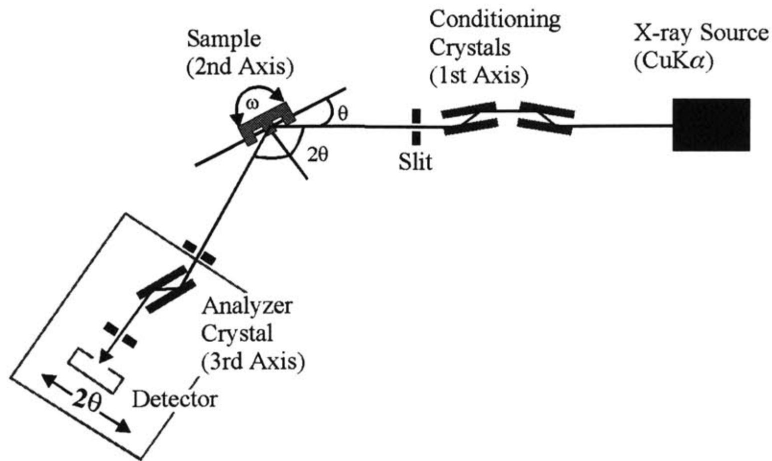

Figure A.12 Generic diagram of a triple axis x-ray diffractometry system. The conditioning crystals are typically configured in either a 2- or 4-bounce arrangement. Likewise, the analyzer crystal is typically configured in either a 2- or 4-bounce arrangement (or possibly a 3-bounce arrangement, depending on the crystal material).

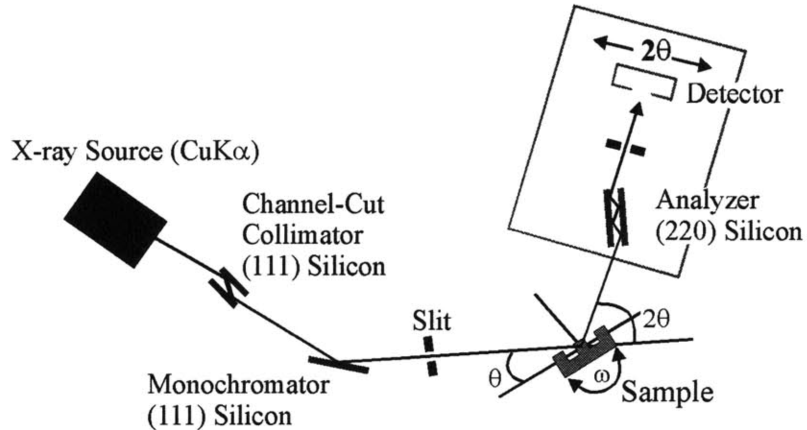

Figure A.13 Diagram of the Bede D^3 diffractometer used at UCLA.

is the resulting narrowness of the x-ray beam incident on the sample (from extensive penetration of the Si conditioning crystals), however the increased beam conditioning comes at a penalty: a decrease in incident beam intensity. The (220)-oriented third crystal is configurable in either a two-bounce or four-bounce mode. Similar to the incident beam conditioning crystals, a larger number of diffractions from the 3rd

crystal narrows the diffracted beam, and thus increases the obtainable resolution. The diffractometer at UCLA is capable of resolving features separated by less than five arcseconds.

At MIT, the diffractometer utilized is also a Bede D^3, however both the instrument and the x-ray source differ from those at UCLA. The incident beam conditioning crystals are two (220)-oriented Si crystals, in which both crystals may be configured for either two or four-bounce modes. If configured in the two-bounce mode, the instrument resolution is ~12 arcsec. With both Si crystals configured in the four-bounce mode, the resolution increases to ~5 arcsec. Like the D^3 at UCLA, the third crystal is also a (220)-oriented Si crystal configurable in either a two- or four-bounce arrangement. As previously mentioned, the x-ray source at MIT differs from that at UCLA; the source utilized at MIT is a Rigaku rotating anode x-ray source. The Cu$K\alpha$ lines are generated at much higher intensities than a Cu tube source. However, as can be deciphered from the fact that the source is a rotating anode, rotation of the Cu anode produces significant vibration. The arrangement of the diffractometer at MIT is such that the housing of the first beam conditioning crystal is essentially connected to the rotating anode column, and thus the resulting vibration is transferred directly to the D^3 instrument. Although it may seem that the vibration is not an issue as the entire diffractometer should vibrate en masse, when attempting to resolve ~5 seconds of arc, any vibration is significant. Furthermore, continuous exposure to vibration detrimentally affects the alignment of the conditioning crystals, resulting in broadening of the incident x-ray beam as well as a subsequent decrease in intensity. The decision to collect the majority of the x-ray data presented in this thesis using diffractometers outside of MIT was made following an extensive investigation of the limitations of the system at MIT.

Additional TAD measurements were performed at MIT Lincoln Laboratory by D. Calawa, using a Philips MRD diffractometer. The Philips diffractometer utilizes a sealed Cu x-ray tube for generation of the incident x-ray beam. The conditioning crystals are (220)-oriented Ge crystals, configured in a two-bounce arrangement. The advantage of Ge over Si is the higher intensity following diffraction, however the resulting FWHM of the diffracted beam is slightly larger than that obtainable with Si. (Cu$K\alpha$ lines penetrate a Si crystal further than Ge, and are thus more strongly conditioned, although at the price of a decrease in intensity.) Likewise, the third crystal is also (220)-oriented Ge, and the diffraction arrangement allows three bounces. Although the resolution of this system may be slightly lower than the Bede D^3, the FWHM of an InP substrate was measured to be ~7 arcseconds. For comparison, the minimum FWHM obtained from the Bede D^3 at UCLA was ~3.5 arcseconds.

A.3 Reciprocal Space Mapping

As described in Section A.1.1, diffraction from a crystal lattice is a representation of the crystal in reciprocal space. Thus, a series of diffraction measurements can be used to map the crystal in reciprocal space. To generate a reciprocal space map (RSM), a series of rocking curves are generated, each at a different incident angle to the sample, ω. Depicted in Figure A.14 is a diagram, in reciprocal space, of the

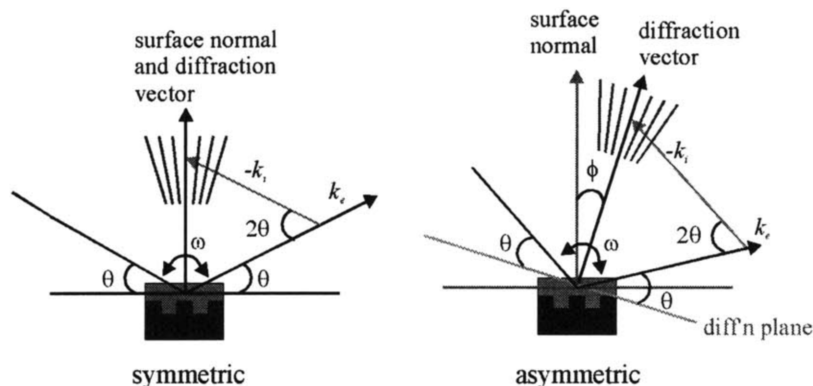

Figure A.14 Generic reciprocal space diagrams of reciprocal space map generation.

mapped area for symmetric and asymmetric reciprocal space maps. As is apparent in the diagrams of Figure A.14, the probed reciprocal space is not perfectly rectangular as the measurements are in reality movement of the Ewald sphere (recall Figure A.3) . However, due to the small angular range in which reciprocal space maps are typically generated, it is rather accurate to assume that the resulting RSM is rectangular. Symmetric RSMs are useful for determining perpendicular lattice parameters as well as detecting curvature (or tilt). Curvature of a crystal lattice appears perpendicular to the reciprocal space vector.

Asymmetric RSMs are useful for detecting relaxation of epitaxial layers since the measurement geometry is sensitive to both the perpendicular and parallel lattice constants. For example, relaxation of a compressive-strained epilayer involves a reduction of the perpendicular lattice constant and a subsequent increase in the parallel lattice constant; the simultaneous occurrence of opposing changes in the lattice constants causes the diffraction conditions to shift towards those along the diffraction vector. Asymmetric RSMs are also sensitive to sample curvature, and the features are apparent perpendicular to the asymmetric diffraction vector. Figure A.15 is a depiction of an asymmetric RSM and the associated orientations in which the above mentioned aspects would be apparent.

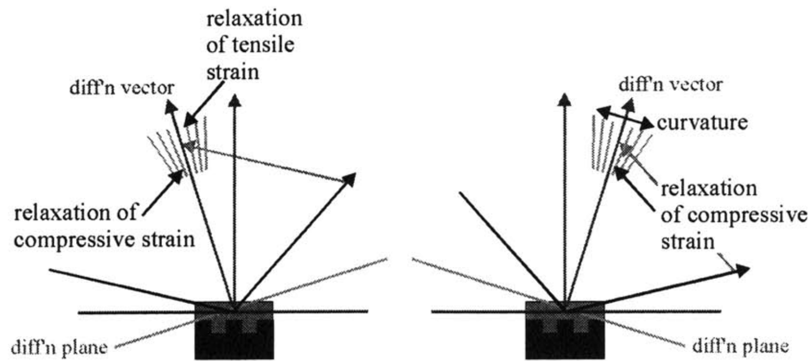

Figure A.15 Depiction of relaxation and curvature directions in asymmetric RSMs. Note, the figure on the left is a glancing incidence arrangement and the figure on the right is glancing exit.

For asymmetric RSMs, four possible diffraction geometries exist; glancing exit and entrance, and diffraction along $[0\bar{1}\bar{1}]$ or $[0\bar{1}1]$ (for InP). Thus, in analyzing the generated RSM, it is important to know which reciprocal space point the map is centered upon for correct interpretation of the data. Because the asymmetric reciprocal lattice vector will be oriented differently depending on the sample direction and diffraction geometry, orientation of aspects such as relaxation are critical for correct analysis of the RSM.

Typical detailed rocking curves are usually generated in under an hour. Since reciprocal spaces maps are a series of rocking curves the data collection times are multiple hours. Typical measurement times for the RSMs presented in this thesis are on the order of 15 hours. Since the data collections times are quite long, it is important to have the source, sample, and instrument stable for accurate data collection. As mentioned in Section A.2.2, the TAD instrument at MIT was hindered by vibration from the rotating anode source, making the collection of data for a reciprocal space map having features with FWHMs less than ~20 arcsec effectively impossible. Shown in Figure A.16 is a (400) RSM generated via (a) the Philips MRD diffractometer at Lincoln Laboratory and (b) the diffractometer at MIT, for the same sample. Alteration of the diffraction conditions following alignment is the cause for the decreased intensity observed in Figure A.16(b).

A.3.1 *q*-space Conversion

Crystallographers typically convert the raw diffraction data into *q*-space units for ease of interpretation as well as ease of comparison between multiple diffraction geometries. *q*-space is reciprocal space, and is in units of inverse length (μm^{-1} used in this thesis). For a more generic basis for comparison, e.g. between different samples and geometries, RSMs are commonly graphed in Δq-space, in which all features are

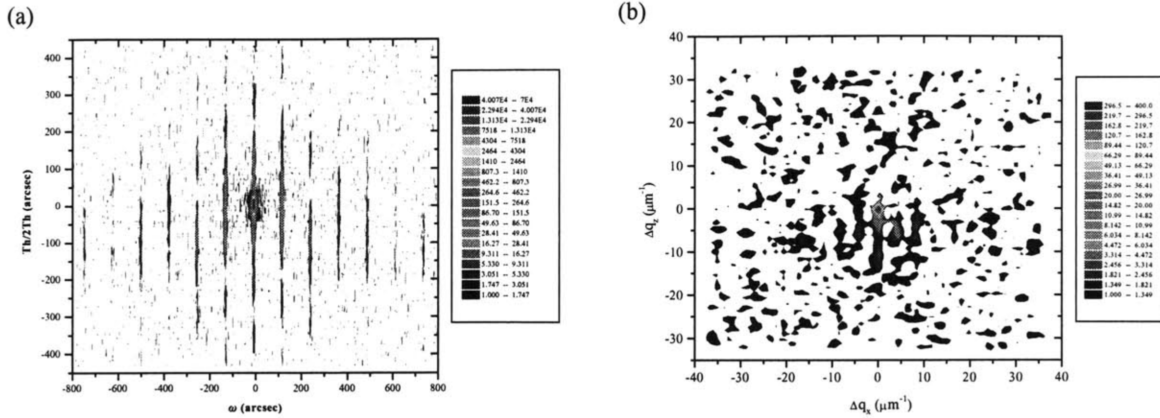

Figure A.16 (a) (400) RSM of a rectangular-patterned InP substrate measured on a Philips MRD at Lincoln Laboratory. (b) (400) RSM of the same patterned substrate measured on the Bede D^3 at MIT.

referenced to the reciprocal space position of the substrate (i.e. the substrate Bragg diffraction peak is located at $\Delta q_{x,y} = \Delta q_z = 0$). For conversion of the raw diffractometer data to Δq-space, the following equations are utilized:

$$\Delta q_{x,y} = \frac{2}{\lambda}[\sin\theta_B + \Delta\theta\cos\theta_B]\sin(\phi + \Delta\omega) - \frac{2}{\lambda}\sin\theta_B\sin\phi \quad \text{Eq. (A.11)}$$

$$\Delta q_z = \frac{2}{\lambda}[\sin\theta_B + \Delta\theta\cos\theta_B]\cos(\phi + \Delta\omega) - \frac{2}{\lambda}\sin\theta_B\cos\phi \quad \text{Eq. (A.12)}$$

where $\Delta\theta$ is the relative angular position parallel to the diffraction vector with respect to the substrate and $\Delta\omega$ is the relative angular position perpendicular to the diffraction vector with respect to the substrate (see labeling in Figure A.17 for geometrical description). The first term in Eq. (A.11) and Eq. (A.12) is the

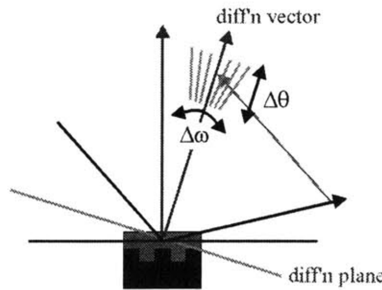

Figure A.17 Geometrical depiction of $\Delta\omega$ and $\Delta\theta$ for Δq-space conversion.

location of the diffracted feature in reciprocal space, and the second term is the absolute position the substrate feature in reciprocal space (subtraction of the substrate position normalizes the equation to the

substrate). In the small angle approximation in which $\Delta\omega \sim 0$, which is valid for most RSM measurements, Eq. (A.11) and Eq. (A.12) become

$$\Delta q_x \approx \frac{2}{\lambda}(\Delta\theta \cos\theta_B)\sin(\phi + \Delta\omega) \quad \text{Eq. (A.13)}$$

$$\Delta q_z \approx \frac{2}{\lambda}(\Delta\theta \cos\theta_B)\cos(\phi + \Delta\omega) \quad \text{Eq. (A.14)}$$

For a symmetric RSM, i.e. (400), ϕ, the angle between the surface normal and the diffraction vector, is zero, thus Eq. (A.13) is zero. Therefore, the small angle approximation can not be assumed for conversion of symmetric measurements. For conversion of symmetric measurements, the following relationships are utilized [177]:

$$\Delta q_x \approx \frac{(2\Delta\omega - \Delta\theta)\sin\theta_B}{\lambda} \quad \text{Eq. (A.15)}$$

$$\Delta q_z \approx \frac{\Delta\theta \cos\theta_B}{\lambda} \quad \text{Eq. (A.16)}$$

For analysis of the RSMs presented in this thesis, the raw data is immediately converted to Δq units. Thus, strain values are calculated by determining the corresponding $\Delta\theta$ and $\Delta\omega$ from Eq. (A.13) and Eq. (A.14), followed by use of Eq. (A.9) and Eq. (A.10).

For analysis of corrugated substrates, the period of the satellite fringes in reciprocal space is inversely proportional to the actual period of the corrugation. The grating period may be calculated using

$$\Lambda \approx \frac{\lambda \cos(\theta_B - \phi)}{\Delta\theta_f \sin 2\theta_B} \quad \text{Eq. (A.17)}$$

where $\Delta\theta_f$ is the angular fringe separation [59].

References

[1] Compound Semiconductor 6(1) (2000) p. 6.

[2] WaveStar 400G product listing on www.lucent.com.

[3] R.A. Berry, V.W.S. Chan, K.L. Hall, E.S. Kintzer, J.D. Moores, K.A. Rauschenbach, E.A. Swanson, L.E. Adams, C.R. Doerr, S.G. Finn, H.A. Haus, E.P. Ippen, W.S. Wong, and M. Haner, "All-Optical Network consortium - Ultrafast TDM Networks", *IEEE J. Select. Areas Commun.* **14** (1996) 999.

[4] F.-S. Choa and H.J. Choa, "All-optical packet routing-architecture and implementation", *Photon. Network Commun.* **1** (1999) 303.

[5] S. Nakamura, Y. Ueno and K. Tajima, "Ultrafast (200-fs Switching, 1.5 Tb/s Demultiplexing) and High-Repetition (10 GHz) Operations of a Polarization-Discriminating Symmetric Mach-Zehnder All-Optical Switch", *IEEE Photon. Technol. Lett.* **10** (1998) 1575.

[6] K. Suzuki, K. Iwatsuki, S. Nishi and M. Saruwatari, "Error-free demultiplexing of 160 Gbit/s pulse signal using optical loop mirror including semiconductor laser amplifier", *Electron. Lett.* **30** (1994) 1501.

[7] I. Glesk, J.P. Sokoloff and P.R. Prucnal, "Demonstration of all-optical demultiplexing of TDM data at 250 Gbit/s", *Electron. Lett.* **30** (1994) 339.

[8] K.L. Hall and K.A. Rauschenbach, "100-Gbit/s bitwise logic", *Opt. Lett.* **23** (1998) 1271.

[9] J. Leuthod, P.-A. Besse, E. Gamper, M. Dülk, S. Fischer, G. Guekos and H. Melchior, "All-Optical Mach-Zehnder Interferometer Wavelength Converters and Switches with Integrated Data- and Control-Signal Separation Scheme", *J. Lightwave Technol.* **17** (1999) 1056.

[10] W.D. Johnston, Jr., private communication.

[11] A. Katz, Ed., *Indium Phosphide and Related Materials: Processing, Technology, and Devices* (Boston: Artech House, Inc.) 1992.

[12] K. Takahei and H. Nagai, "Instability of In-Ga-As-P Liquid solution during Low Temperature LPE of $In_{1-x}Ga_xAs_{1-y}P_y$ on InP", *Jpn. J. Appl. Phys.* **20** (1981) L313.

[13] R.R. LaPierre, T. Okada, B.J. Robinson, D.A. Thompson and G.C. Weatherly, "Lateral composition modulation in InGaAsP strained layers and quantum wells grown on (100) InP by gas source molecular beam epitaxy", *J. Crystal Growth* **158** (1996) 6.

[14] H. Asonen, K. Rakennus, K. Tappura, M. Hovinen and M. Pessa, "Growth of InP, InGaAs, and InGaAsP on InP by Gas-Source Molecular Beam Epitaxy", *J. Crystal Growth* **105** (1990) 101.

[15] L. Vegard, *Z. Phys.* **5** (1921) 17.

[16] M.B. Panish and H. Temkin, *Gas Source Molecular Beam Epitaxy Growth and Propoerties of Phosphorus Containing III-V Heterostructures* (Berlin: Springer-Verlag) 1993.

[17] H. Lüth, *Surfaces and Interfaces of Solids* (Berlin: Springer-Verlag) 1993.

[18] N. Takeyasu, H. Asahi, S.J. Yu, K. Asami, T. Kaneko and S. Gonda "Gas source MEE (migration enhanced epitaxy) growth of InP", *J. Crystal Growth* **111** (1991) 502.

[19] EPI MBE Products Group, "The EPI SUMO Cell: A Revolutionary Group III Source", company brochure, February 1996.

[20] Instruction Manual for High Temperature Gas Cell, Riber Division d'Instruments S.A., 1990.

[21] G.B. Stringfellow, *Organometallic Vapor-Phase Epitaxy* (San Diego: Academic Press, Inc.) 1989.

[22] EPI MBE Products Group, "Cracking Efficiency of the EPI Atomic Hydrogn Source", company brochure, January 1996.

[23] EPI MBE Products Group, "Epitaxial Phosphides by Solid Source MBE", company brochure.

[24] G.W. Wicks, M.W. Koch, J.A. Varriano, F.G. Johnson, C.R. Wie, H.M. Kim and P. Colombo, "Use of a valved, solid phosphorus source for the growth of $Ga_{0.5}In_{0.5}P$ and $Al_{0.5}In_{0.5}P$ by molecular beam epitaxy", *Appl. Phys. Lett.* **59** (1991) 342.

[25] W-Y. Hwang, J.N. Baillargeon, S.N.G. Chu, P.F. Sciortino and A.Y. Cho, "GaInAsP/InP distributed feedback lasers grown directly on grated substrates by solid-source molecular beam epitaxy", *J. Vac. Sci. Technol. B* **16** (1998) 1422.

[26] J.M. Milikow, *Growth and Characterization of III-V Compound Semiconductors*, M.S. Thesis, Massachusetts Institute of Technology, June 1997.

[27] E.A. Marley, *The Development of InP-Based Optoelectronic Devices*, M.S. Thesis, Massachusetts Institute of Technology, June 1996.

[28] M.A. Cotta, R.A. Hamm, S.N.G. Chu and L.R. Harriot, "On the origin of oval defects in metalorganic molecular beam epitaxy of InP", *Appl. Phys. Lett.* **66** (1995) 2358.

[29] D.J. Arent, S. Nilsson, Y.D. Galeuchet, H.P. Meier and W. Walter, "Indium adatom migration during molecular beam epitaxial growth of strained InGaAs/GaAs single quantum wells", *Appl. Phys. Lett.* **55** (1989) 2611.

[30] K. Ohta, T. Kojima and T. Nakagawa, "Aniostropic surface migration of Ga atoms on GaAs (001)", *J. Crystal Growth* **95** (1989) 71.

[31] M.A. Herman and H. Sitter, *Molecular Beam Epitaxy Fundamentals and Current Status* (Berlin: Springer-Verlag) 1996.

[32] H.Q. Hou and C.W. Tu, "In-situ control of As composition in InAsP and InGaAsP grown by gas-source molecular beam epitaxy", *Appl. Phys. Lett.* **60** (1992) 1872.

[33] T. Mozume, H. Kashima, K. Hosomi, K. Ouchi, H. Sato, H. Masuda and T. Tanoue, "Effect of source-supply interruptions on the interface abruptness in gas source molecular beam epitaxy grown InGaAs/ InP heterostructures", *J. Crystal Growth* **150** (1995) 591.

[34] G.-J. Shiau, C.-P. Chao, P.E. Burrows and S.R. Forrest, "Growth of Abrupt InGaAs(P)/In(GaAS)P heterointerfaces by Gas Source Molecular Beam Epitaxy, "*J. Appl. Phys.* **77** (1995) 201.

[35] H.Q. Hou and C.W. Tu, "InGaAsP/InP multiple quantum wells grown by gas-source molecular beam epitaxy", *J. Crystal Growth* **120** (1992) 167.

[36] T.-L. Lee, J.-S. Liu and H.-H. Lin, "the incorporation behavior of As and P in GaInAsP ($\lambda \sim 1.3$ μm) on InP grown by gas source molecular beam eptiaxy", *J. Crystal Growth* **155** (1995) 16.

[37] K. Tappura, "Incorporation of group V elements in gas-source molecular beam epitaxy of GaInAsP with x~0.15 and y~0.33", *J. Crystal Growth* **123** (1992) 133.

[38] M. Pessa, K. Tappura, and A. Ovtchinnikov, "GaInAsP gas-source MBE technology", *Thin Solid Films* **267** (1995) 99.

[39] B. de Cremoux, P. Hirtz and J. Ricciardi, *Proc. 1980 Int. Symp. GaAs & Related Compounds* (Inst. Phys., London, 1981) p. 115.

[40] K. Onabe, "Calculation of Miscibility Gap in Quaternary InGaPAs with Strictly Regular Solution Approximation", *Jap. J. Appl. Phys.* **21** (1982) 797.

[41] G.B. Stringfellow, "Miscibility Gaps in Quaternary III/V Alloys", *J. Crystal Growth* **58** (1982) 194.

[42] P. Henoc, A. Izrael, M. Quillec and H. Launois, "Composition modulation in liquid phase epitaxial $In_xGa_{1-x}As_yP_{1-y}$ layers lattice matched to InP substrates", *Appl. Phys. Lett.* **40** (1982) 963.

[43] K. Tappura and J. Laurila, "Unstable regions in the growth of GaInAsP by gas-source molecular beam epitaxy", *J. Crystal Growth* **131** (1993) 309.

[44] R.R. LaPierre, T. Okada, B.J. Robinson, D.A. Thompson and G.C. Weatherly, "Spinodal-like decomposition of InGaAsP/(100) InP grown by gas source molecular beam epitaxy", *J. Crystal Growth* **155** (1995) 1.

[45] R.R. LaPierre, T. Okada, B.J. Robinson, D.A. Thompson and G.C. Weatherly, "Lateral composition modulation in InGaAsP strained layers and quantum wells grown on (100) InP by gas source molecular beam epitaxy", *J. Crystal Growth* **158** (1996) 6.

[46] R.R. LaPierre, B.J. Robinson and D.A. Thompson, "Growth mechanisms of III-V compounds by atomic hydrogen-assisted epitaxy", *J. Crystal Growth* **191** (1998) 319.

[47] R.R. LaPierre, D.A. Thompson and B.J. Robinson, "Reduction of composition modulation of InGaAsP grown by atomic-hydrogen-assited epitaxy producing improved double-heterostructure laser performance", *Semicond. Sci. Technol.* **13** (1998) 637.

[48] L.E. Davis, N.C. MacDonald, P.W. Palmberg, G.E. Riach and R.E. Weber, *Handbook of Auger Elecron Spectroscopy,* (Eden Prairie, MN : Physical Electronics Industries, Inc.) 1976.

[49] P.D. Healy, K. Bao, M. Gokhale, J.E. Ayers and F.C. Jain, "X-ray Determination of the Dislocation Densitites in Semicondcutor Crystals Using a Bartels Five-Crystal Diffractometer", *Acta Cryst.* **A51** (1995) 498.

[50] K.K. Smith, "Photoluminescence of Semiconductor Materials", *Thin Solid Films* **84** (1981) 171.

[51] R. Benzaquen, S. Charbonneau, N. Sawadsky, A.P. Roth, R. Leonelli, L. Hobbs and G. Knight, "Alloy broadening in photoluminescence spectra of $Ga_xIn_{1-x}As_yP_{1-y}$ lattice matched to InP", *J. Appl. Phys.* **75** (1994) 2633.

[52] I. Suemune, Y. Kunitsugu, Y. Kan and M. Yamanishi, "Incidence angle effect of a hydrogen plasma beam for the cleaning of semiconductor surfaces", *Appl. Phys. Lett.* **55** (1989) 760.

[53] Y.J. Chun, T. Sugaya, Y. Okada and M. Kawabe, "Low Temperature Surface Cleaning of InP by Irradiation of Atomic Hydrogen", *Jpn. J. Appl. Phys.* **32** (1993) L287.

[54] J.E. Cunningham, W.Y. Jan, W.H. Knox and S. Tsuda, "Saturable Bragg reflector and process for fabricating the same", U.S. Patent No. 5701327 (1997).

[55] G.P. Agrawal and N.K. Dutta, *Long Wavelength Semiconductor Lasers* (Princeton, NJ: Van Nostrand) 1986; H. Ghafouri-Shiraz and B.S.K. Lo, *Distributed Feedback Laser Diodes Principles and Physical Modeling* (New York: John Wiley and Sons) 1996.

[56] Z.L. Liau and H.J. Zeiger, "Surface-energy-induced mass-transport phenomenon in annealing of etched compound semiconductor structures: Theoretical modeling and experimental confirmation", *J. Appl. Phys.* **67** (1990) 2434L.

[57] A.A. Darhuber, E. Koppensteiner, H. Straub, G. Brunthaler, W. Faschinger and G. Bauer, "Triple axis x-ray investigations of semiconductor surface corrugations", *J. Appl. Phys.* **76** (1994) 7816.

[58] P. van der Sluis, "High resolution X-ray diffraction of one- and two-dimensional periodic surface gratings", *J. Phys III France* **4** (1994) 1639.

[59] A.T. Macrander and S.E.G. Slusky, "X-ray diffraction from corrugated crystalline surfaces and interfaces", *Appl. Phys. Lett.* **56** (1990) 443.

[60] A. Perales, L. Goldstein, A. Accard, B. Fernier, F. Leblond, C. Gourdain and P. Brosson, "High Performance DFB-MQW Lasers at 1.5 μm Grown by GSMBE", *Electron. Lett.* **26** (1990) 236.

[61] B. Fernier, C. Artigue, D. Bonnevie, L. Goldstein, A. Perales and J. Benoit, "Low-Threshold 1.5 μm DFB Lasers Growth by GSMBE", *Electron. Lett.* **25** (1989) 768.

[62] K. Sato, M. Oishi, Y. Itaya, M. Nakao and Y. Imamura ,"Defect generation due to surface corrugation in InGaAsP/InP DFB laser structures grown by MOVPE on grating-formed InP substrates", *J. Crystal Growth* **93** (1988) 825.

[63] T. Koui, Y. Sakata, Y. Sasaki, T. Matsumoto and K. Komatsu, "Mass-transport effect on InP corrugation shape control of DFB-LDs under atmospheric pressure MOVPE", *J. Crystal Growth* **195** (1998) 503.

[64] M. Kito, N. Otsuka, Y. Yabuuchi, S. Nakamura, M. Ishino and Y. Matsui, "Formation of InAsP layer on corrugated InP substrate by MOVPE for buried grating of DFB lasers", 1997 *Proc. 9th Int. Conf. on InP and Related Materials* (IEEE, Piscataway, NJ) p. 606.

[65] T. Tanbun-Ek, R.A. Logan, H. Temkin, N.A. Olsson, M.C. Wu, A.M. Sergent and K.W. Wecht, "Reproducible growth of narrow linewidth multiple quantum well graded index separate confinement distributed feedback (MQW-GRIN-SCH-DFB) lasers by MOVPE", *J. Crystal Growth* **107** (1991) 751.

[66] A. Izrael, D. Robein and C. Vaudry, "Epitaxial overgrowth on nanometric InP wires processed by reactive ion etching", *Microelectron. Eng.* **13** (1995) 395.

[67] H.A. Haus and Y. Lai, "Narrow-Band Distributed Feedback Reflector Design", *J. Lightwave Technol.* **9** (1991) 754; H.A. Haus and Y. Lai, "Narrow-Band Optical Channel-Dropping Filter", *J. Lightwave Technol.* **10** (1992) 57.

[68] J.N. Damask, "Practical Design of Side-Coupled Quarter-Wave Shifted Distributed-Bragg Resonant Filters", *J. Lightwave Technol.* **14** (1996) 812.

[69] D. Rosenblatt, A. Sharon and A.A. Friesem, "Resonant Grating Waveguide Structures", *IEEE J. Quantum Electron.* **33** (1997) 2038.

[70] K.-Y. Lim, D.J. Ripin, G.S. Petrich, L.A. Kolodziejski, E.P. Ippen, M. Mondol, Henry I. Smith, P.R. Villeneuve, S. Fan and J.D. Joannopoulos, "Photonic band-gap waveguide microcavities: Monorails and air bridges", *J. Vac. Sci. Technol. B* **17** (1999) 1171.

[71] S.N.G. Chu, W.T. Tsang, F.S. Choa, R.A. Logan, E.J. Flynn and D.L. Coblentz, "Elimination of light scattering from grating irregularities by using a quantum well grating in index or gain-coupled distributed feedback lasers", *Appl. Phys. Lett.* **63** (1993) 1886.

[72] J.-W. Han, J.-H. Cha and S.-B. Kim, "Effects of the Random Fluctuation in Grating Period on the Characteristics of Quarter-Wavelengh-Shifted DFB Lasers", *IEEE Photon. Technol. Lett.* **11** (1999) 1569.

[73] J.N. Damask, private communication (1997).

[74] S.N.G. Chu, T. Tanbun-Ek, R.A. Logan, J. Vandenberg, P.F. Sciortino, Jr, P. Wisk and T.L. Pernell, "Grating Overgrowth and Defect Structures in Distributed-Feedback-Buried Heterostructure Laser Diodes", *IEEE J. Selected Topics Quantum Electron.* **3** (1997) 862.

[75] J. Wang, D.A. Thompson, B.J. Robinson and J.G. Simmons, "Molecular beam epitaxial growth of InGaAs/InGaAsP quantum wires on V-grooved InP substrates with (111) sidewalls", *J. Crystal Growth* **175/176** (1997) 793.

[76] M. Kappelt , V. Turck and D. Bimber, "$InAs_xP_{1-x}$ Groove Quantum Wires", *Proc. 9th Int. Conf. on InP and Related Materials,* 1998 (IEEE, Piscataway, NJ) p 587.

[77] T. Nishida, M. Nakao, T. Tamamura, A. Ozawa, Y. Saito, K. Nishimura and H. Yoshihara, "Synchrotron Radiation Lithography for DFB Laser Gratings", *Japan. J. Appl. Phys.* **28** (1989) 2333.

[78] N. Haider, M.R. Wilby and D.D. Vvedensky, "Epitaxial growth kinetics on patterned substrates", *Appl. Phys. Lett.* **62** (1993) 3108.

[79] D.J. Arent, S. Nilsson, Y.D. Galeuchet, H.P. Meier and W. Walter, "Indium adatom migration during molecular beam epitaxial growth of strained InGaAs/GaAs single quantum wells", *Appl. Phys. Lett.* **55** (1989) 2611.

[80] J. Jian, J.X. Zhou, Z. Zhong and C. Soo-Jin, "Atom diffusion during MBE growth on patterned substrate", *Microelectron. Eng.* **43-44** (1998) 409.

[81] N.J. Bultika, A. Gupta, B.J. Robinson, D.A. Thompson, G.C. Weatherly and J.C. Simmons, "Characterization of InGaAs/InP Epitaxial Layers Grown Over V-Groove Patterned InP Substrates Using Gas Source Molecular Beam Epitaxy", *Mater. Res. Soc. Symp. Proc.* **326** (1994) 39.

[82] C.A. Mullan, G.C. Weatherly and D.A. Thompson, "Compositional variations in InGaAsP films grown on patterned substrates", *J. Crystal Growth* **182** (1997) 266.

[83] N. Inoue, "MBE monolayer growth control by in-situ electron microscopy", *J. Crystal Growth* **111** (1991) 75.

[84] M. Hata, T. Isu, A. Watanabe and Y. Katayama, "Distributions of growth rates on patterned surfaces measured by scanning microprobe reflection high-energy electron diffraction", *J. Vac. Sci. Technol. B* **8** (1990) 692.

[85] M.P.P. de Castro, N.C. Frateschi, J. Bettini, C.A. Ribeiro and M.M. de Carvalho, "Spatial composition dependence in InGaP grwoth on pre-patterned GaAs substrates by chemical beam epitaxy", *J. Crystal Growth* **203** (1999) 317.

[86] D. Wüllner, M. Chahoud, T. Schrimpf, P. Bönsch, H.-H. Wehmann and A. Schlachetzki, "Diffusion during metalorganic vapor-phase epitaxy on V-groove patterned substrates", *J. Appl. Phys.* **85** (1999) 249.

[87] M. Hata, A. Watanabe and T. Isu, "Surface diffusion length observed by in situ scanning microprobe reflection high-enrgy electron diffraction", *J. Crystal Growth* **111** (1991) 83.

[88] A.R. Pratt, R.L. Williams, C.E. Norman, M.R. Fahy, A. Marinopoulou and F. Chatenoud, "Indium migration control on patterned substrates for optoelectronic device applications", *Appl. Phys. Lett.* **65** (1994) 1009.

[89] G. Biasiol and E. Kapon, "Mechanism of self-limiting epitaxial growth on nonplanar substrates", *J. Crystal Growth* **201/202** (1999) 62.

[90] C.A. Mullan, B.J. Robinson, D.A. Thompson and G.C. Weatherly, "An investigation into gas source molecular beam epitaxy deposition onto non-planar InP patterned substrates", *Microscopy of Semiconducting Materials* (Inst. Phys. Conf. Ser. 146) ed. A.G. Cullins and A.E. Staton-Bevan (Norfolk: Institue of Physics) 1995, p. 231.

[91] N. Darowski, U. Pietsch, U. Zeimer, V. Smirnitzki and F. Bugge, "X-ray study of lateral strain and composition modulation in an AlGaAs overlayer induced by a GaAs lateral surface grating", *J. Appl. Phys.* **84** (1998) 1366.

[92] R. Bhat, E. Kapon, J. Werner, D.M. Hwang, N.G. Stoffel and M.A. Koza, "Organometallic chemical vapor deposition of InP/InGaAsP on nonplanar InP substrates: Application to multiple quantum well lasers", *Appl. Phys. Lett.* **56** (1990) 863.

[93] Z.L. Liau and H.J. Zeiger, "Surface-energy-induced mass-transport phenomenon in annealing of etched compound semiconductor structures: Theoretical modeling and experimental confirmation", *J. Appl. Phys.* **67** (1990) 2434.

[94] H. Nagai, Y. Noguchi and T. Matsuoka, "Thermal Deformation of Surface Corrugations on InGaAsP Crystals", *J. Crystal Growth* **71** (1985) 225.

[95] M. Kappelt, V. Türck, D. Bimberg, H. Kirmse, I. Hähnert and W. Newmann, "InGaAs and InAsP V-groove quantum wires using arsenic/phorphorus exchange preparation", *J. Crystal Growth* **195** (1998) 552.

[96] B.-T. Lee, R.A. Logan and S.N.G. Chu, "Observation of growth patterns during atmospheric pressure metalorganic vapor phase epitaxy regrowth of InP around etched mesas", *J. Crystal Growth* **130** (1993) 287.

[97] R. Butendeich, M. Hurich and H. Heinecke, "Material localisation at GaInAsP-ridge-structures selectively grown by MOMBE", *J. Crystal Growth* **195** (1998) 510.

[98] T. Matsui, K. Ohtsuka, H. Sugimoto, Y. Abe and T. Ohishi, "1.5 mm GaInAsP/InP buried-heterostructure laser diode fabricated by reacitve ion etching using a mixture of ethane and hydrogen", *Appl. Phys. Lett.* **56** (1990) 1641.

[99] R.J. Simes, E.G. Goarin, C. Labourie, D. Bonnevie, A. Perales, D. Lesterlin and L. Goldstein, "GSMBE Growth on Patterned Substrates for Optoelectronic Devices", *Proc. 4th Int. Conf. on InP and Related Materials* (IEEE, Piscataway, NJ) 1992, pp. 198.

[100] B.-T. Lee, R.A. Logan, R.F. Kalicek, Jr., A.M. Sergent, D.L. Coblentz, K.W. Wecht, T. Tanbun-Ek, "Fabrication of InGaAsP/InP Buried Heterostructure Laser Using Reactive Ion Etching and Metalorganic Chemical Vapor Deposition", *IEEE Photon. Technol. Lett.* **5** (1993) 279.

[101] B. Baur, H. Heinecke, M. Schier and N. Emeis, "Growth of GaInAs(P)/InP heterostructures on nonplanar substrates using MOMBE (CBE)", *J. Crystal Growth* **127** (1993) 175.

[102] X.G. Xu, Ch. Giesen, R. Hövel, M. Heuken and K. Heime, "Surface morphology and growth rate variation of InP on patterned substrates using tertiarybutylphosphine", *J. Crystal Growth* **191** (1998) 341.

[103] E.L. Hu, C.-H. Chen and D.L. Green, "Low-energy ion damage in semiconductors: A progress report", *J. Vac. Sci. Technol. B* **14** (1996) 3632.

[104] S. Murad, M. Rahman, N. Johnson, S. Thoms, S.P. Beaumont and C.D.W. Wilkinson, "Dry etching damage in III-V semiconductors", *J. Vac. Sci. Technol. B* **14** (1996) 3658.

[105] N. Yamamoto, H. Mawatari and K. Kishi, "Electrical Evaluation of Dry Etching Damage on the Side Wall of Mesa Structure", *Proc. 10th Int. Conf. on InP and Related Materials* (IEEE, Piscataway, NJ) 1998, pp. 467.

[106] J. Behrend, A. Rudra, L. Sagalowicz, C.-A. Berseth, J.-F. Carlin, A. Schoenberg, P.H. Jouneau and E. Kapon, "Sructural and Optical Characterization of InP/IngaAsP Distributed Bragg Reflectors Grown by CBE", *Proc. 9th Int. Conf. on InP and Related Materials* (IEEE, Piscataway, NJ) 1997, pp. 428.

[107] L. Leprince, G.T. Baumbach, A. Talneau, M. Gailhanou and J. Schneck, "Observation of strain relaxation phenomena in buried and nonburied III-V surface gratings through high resolution x-ray diffraction", *Appl. Phys. Lett.* **71** (1997) 3227.

[108] Q. Shen, S.W. Kycia, E.S. Tentarelli, W.J. Schaff and L.F. Eastman, "X-ray-diffraction study of size-dependent strain in quantum-wire structures", *Phys. Rev. B* **54** (1996) 16381.

[109] S.L. Chuang, *Physics of Optotlectronic Devices* (New Yrok: Wiley) 1995.

[110] M. Ohtsuka, "A numerical simulation model for molecular-beam epitaxial (MBE) growth on nonplanar surfaces", *J. Crystal Growth* **205** (1999) 112.

[111] J. Shah, *Ultrafast Spectroscopy of Semiconductors and Semiconductor Nanostructures*, (Berlin: Springer-Verlag) 1996.

[112] B.E. Bouma, G.J. Tearney, S.A. Boppart, M.R. Hee, M.B. Brezinski, J.G. Fujimoto, "High-resolution optical coherence tomographic imaging using a mode-locked Ti:Al_2O_3 laser source", *Opt. Lett.* **20** (1995) 1486.

[113] G.P. Agrawal, *Nonlinear Fiber Optics* (San Diego: Academic Press, Inc.) 1995.

[114] G.R. Fowles, *Introduction to Modern Optics* (Mineola, NY: Dover Publications, Inc.) 1989.

[115] U. Morgner, F.X. Kärtner, S.H. Cho, Y. Chen, H.A. Haus, J.G. Fujimoto, and E.P. Ippen, "Sub-two-cycle pulses from a Kerr-lens mode-locked Ti:sapphire laser", *Opt. Lett.* **24** (1999) 411.

[116] D.H. Sutter, G. Steinmeyer, L. Gallmann, N. Matuschek, F. Morier-Genoud, U. Keller, V. Scheuer, G. Angelow and T. Tschudi, "Semiconductor saturable-absorber mirror-assited kerr-lens mode-locked Ti:sapphire laser producing pulses in the two-cycle regime", *Opt. Lett.* **24** (1999) 631.

[117] P. Das, *Lasers and Optical Engineering* (New York: Springer-Verlag, Inc.) 1991.

[118] H.A. Haus, "Parameter ranges for CW passive mode locking", *IEEE J. Quantum Electron.* **QE-12** (1976) 169.

[119] M. Jiang, G. Sucha, M. Fermann and D. Harter, "CW passive mode-locking evloved from Q-switched mode-locking in erbium doped fiber lasers", in *Conference on Lasers and Electro-Optics*, OSA Technical Digest (Optical Society of America, Washington, DC, 1999) pp.440.

[120] G.D. Boyd, D.A.B. Miller, D.S. Chemla, S.L McCall, A.C. Gossard and J.H. English, "Multiple quantum well reflection modulator", *Appl. Phys. Lett.* **50** (1987) 1119.

[121] E. Garmire and A. Kost, Editors, *Nonlinear Optics in Semiconductors II* (Boston: Academic Press) 1999, p. 211-283.

[122] B.C. Collings, J.B. Stark, S. Tsuda, W.H. Knox, J.E. Cunningham, W.Y. Jan, R. Pathak, and K. Bergman, "Saturable Bragg reflector self-starting passive mode locking of a Cr^{4+}:YAG laser pumped with a diode-pumped Nd:YVO_4 laser", *Opt. Lett.* **21** (1996) *1171.*

[123] S. Tsuda, W.H. Knox, S.T. Cundiff, "High efficiency diode pumping of a saturable Bragg reflector-mode-locked Cr:LiSAF femtosecond laser", *Appl. Phys. Lett.* **69** (1996) 1538.

[124] G.S. Gray and A.B. Grudinin, "Soliton fiber laser with a hybrid saturable absorber", *Opt. Lett.* **21** (1996) 207.

[125] Z. Zhang, K. Torizuka, T. Itatani, K. Kobayashi, T. Sugaya, T. Nakagawa, "Femtosecond Cr:Forsterite Laser with Mode Locking Initiated by a Quantum-Well Saturable Absorber", *IEEE J. Quantum Electron.* **33** (1997) 1975.

[126] B.C. Collings, K. Beregman, S.T. Cundiff, S. Tsuda, J.N. Kutz, J.E. Cunningham, W.Y. Jan, M. Koch and W.H. Knox, "Short Cavity Erbium/Ytterbium Fiber Lsers Mode-Locked with a Saturable Bragg Reflector", *IEEE J. Select. Topics in Quantum. Electron.* **3** (1997) 1065.

[127] M.J. Lederer, B. Luther-Davies, H.H. Tan and C. Jagadish, "GaAs based anti-resonant Fabry-Perot saturable absorber fabricated by metal organic vapor phase epitaxy and ion implantation", *Appl. Phys. Lett.* **70** (1997) 3428.

[128] J. Mangeney, J.L. Oudar, J.C. Harmand, C. Mériadec, G. Patriarche, G. Aubin, N. Stelmakh and J.M. Lourtioz, "Ultrafast staurable absorption at 1.55 mm in heavy-ion-irradiated quantum-well vertical cavity", *Appl. Phys. Lett.* **76** (2000) 1371.

[129] P. Langlois, M. Joschko, E.R. Thoen, E.M. Koontz, F.X. Kärtner, E.P. Ippen, and L.A. Kolodziejski, "High fluence ultrafast dynamics of semiconductor saturable absorber mirrors", *Appl. Phys. Lett.* **75** (1999) 3841.

[130] K. Seeger, *Semiconductor Physics* (New York: Springer-Verlag) 1991.

[131] E.R. Thoen, *Development of Ultrashort Pulse Fiber Lasers for Optical Communication Utilizing Semiconductor Structures*, Ph.D. Thesis, Massachusetts Institute of Technology, June 2000.

[132] A. T. Obeidat, W. H. Knox, and J. B. Khurgin, "Effects of two-photon absorption in saturable Bragg reflectors used in femtosecond solid state lasers", *Opt. Express* **1** (1997) 68.

[133] F.X. Kärtner, L.R. Brovelli, D. Kopf, M. Kamp, I. Calasso and U. Keller, "Control of Solid State Laser Dynamics by Semiconductor Devices", *Opt. Eng.* (Bellingham) **34** (1995) 2024.

[134] X. Shan, D. Cleland and A. Ellis, "Stabilising Er Fibre Soliton Laser with Pulse Phase Locking", *Electron. Lett.* **28** (1992) 182.

[135] C.R. Doerr, H.A. Haus, E.P. Ippen, M. Shirasaki and K. Tamura, "Additive-pulse limiting", *Opt. Lett.* **19** (1994) 31.

[136] M. Nakazawa, K. Tamura and E. Yoshida, "Supermode noise suppression in a harmonically modelocked fibre laser by selfphase modulation and spectral filtering", *Electron. Lett.* **32** (1996) 461.

[137] D.H. Sutter, G. Steinmeyer, L. Gallmann, N. Matuschek, F. Morier-Genoud, U. Keller, V. Scheuer, G. Angelow and T. Tschudi, "Semiconductor saturable-absorber mirror-assisted Kerr-lens mode-locked Ti:sapphire laser producing pulses in the two-cycle regime", *Opt. Lett.* **24** (1999) 631.

[138] N. Matuschek, F.X. Kärtner and U. Keller, "Analytical Design of Double-Chirped Mirrors with Custom-Tailored Dispersion Characteristics", *IEEE J. Quantum. Electron.* **35** (1999) 129.

[139] I.D. Jung, F.X. Kärtner, N. Matuschek, D.H. Sutter, F. Morier-Genoud, G. Zhang, U. Keller, V. Scheuer, M. Tilsch and T. Tschudi, "Self-starting 6.5-fs pulses from a Ti:sapphire laser", *Opt. Lett.* **22** (1997) 1009.

[140] D.H. Sutter, I.D. Jung, F.X. Kärtner, N. Matuschek, F. Morier-Genoud, V. Scheuer, M. Tilsch, T. Tschudi and U. Keller, "Self-Starting 6.5-fs Pulses from a Ti:Sapphire Laser Using a Semiconductor Saturable Absorber and Double-Chirped Mirrors", *IEEE. J. Select. Topics Quantum. Electron.* **4** (1998) 169.

[141] Y.-S. Lee, Y.-H. Lee and J.-H. Lee, "Wet oxidation of AlAs grown by molecular beam epitaxy", *Appl. Phys. Lett.* **65** (1994) 2717.

[142] K.D. Choquette, K.M. Geib, C.I.H. Ashby, R.D. Twesten, O. Blum, H.Q. Hou, D.M Follstaedt, B. E. Hammons, D. Mathes and R. Hull, "Advances in Selective Wet Oxidation of AlGaAs Alloys", *IEEE J. Select. Topics Quantum. Electron.* **3** (1997) 916.

[143] R.D. Twesten, D.M. Follstaedt and K.D. Choquette, "Microstructure and interface properties of laterally oxidized $Al_xGa_{1-x}As$", SPIE vol. 3003 (1997) p. 55.

[144] J.H. Seo and K.S. Seo, "Strain relaxation of InGaAs/GaAs superlattices by wet oxidation of underlying AlAs layer", *Appl. Phys. Lett.* **72** (1998) 1466.

[145] Z. Pan, Y. Zhang, Y. Du, H.X. Han and R.H. Wu, "Stress measurements in oxidized GaAs/AlAs structures by micro-Raman spectroscopy", *1998 IEEE Lasers and Electro-Optics Society Annual Meeting*, vol. 2 (IEEE, Piscataway, NJ) p. 242.

[146] H. Reese, Y.J. Chiu and E. Hu, "Low-temperature-grown GaAs enhanced wet thermal oxidation of $Al_{0.98}Ga_{0.02}As$", *Appl. Phys. Lett.* **73** (1998) 2624.

[147] K.J. Knopp, R.P. Mirin, D.H. Christensen, K.A. Bertness, A. Roshko and R.A. Synowicki, "Optical constants of $(Al_{0.98}Ga_{0.02})_xO_y$ native oxides", *Appl. Phys. Lett.* **73** (1998) 3512.

[148] C.I.H. Ashby, M.M. Bridges, A.A. Allerman, B.E. Hammons and H.Q. Hou, "Origin of the time dependence of wet oxidation of AlGaAs", *Appl. Phys. Lett.* **75** (1999) 73.

[149] M.H. MacDougal, H. Zhao, P.D. Dapkus, M. Ziari and W.H. Steier, "Wide-bandwidth distributed Bragg reflectors using oxide/GaAs multilayers", *Electron. Lett.* **30** (1994) 1147.

[150] L.A. Coldren, E. Hegblom, E. Strzelecka, J. Ko, Y. Akulova and B. Thibeault, "Recent advances and important issues in vertical-cavity lasers", SPIE vol. 3003 (1997) p. 2.

[151] M.H. MacDougal, J. Geske, C.-K. Lim, A.E. Bond and P.D. Dapkus, "Low Resistance Intracavity-contacted oxide-Aperature VCSEL's", *IEEE Photon. Technol. Lett.* **10** (1998) 9.

[152] T.-H. Oh, M.R. McDaniel, D.L. Huffaker and D.G. Deppe, "Cavity-Induced Antiguiding in a Selectively Oxidized Vertical-Cavity Surface-Emitting Laser", *IEEE Photon. Technol. Lett.* **10** (1998) 12.

[153] D.L. Huffaker, H. Deng and D.G. Deppe, "1.15-µm Wavelength Oxide-Confined Quantum-Dot Vertical-Cavity Surface-Emitting Laser", *IEEE Photon. Technol. Lett* **10** (1998) 185.

[154] C. Starck, A. Plais, E. Derouin, A. Pinquier, F. Gaborit, C. Fortin, L. Goldstein, J. Boucart, P. Salet, D. Carpentier and J. Jacquet, "Fabriation of 1.55 mm oxidized VCSELs with top metamorphic GaAs/GaAsAs and bottom InP/InGaAsP Bragg reflectors", *10th Intern. Conf. on Indium Phosphide and Related Materials*, 11-15 May, 1998, p.369.

[155] P.W. Evans, J.J. Wierer and N. Holonyak, Jr., "$Al_xGa_{1-x}As$ native-oxide-based distributed Bragg reflectors for vertical cavity surface emitting lasers", *J. Appl. Phys.* **84** (1998) 5436.

[156] Kuo-Yi Lim, D.J. Ripin, G.S. Petrich, L.A. Kolodziejski, E.P. Ippen, M. Mondol, Henry I. Smith, P.R. Villeneuve, S. Fan, and J.D. Joannopoulos, *J. Vac. Sci. Technol. B* **17** (1999) 1171.

[157] rA.A. Erchak, D.J. Ripin, S. Fan, G.S. Petrich, J.D. Joannopoulos, L.A. Kolodziejski and E.P. Ippen, "Increased Light Extraction from a Light-Emitting Diode Using a Two Dimensional Photonic Crystal", accepted for presentation at the *Conference on Lasers and Electro-Optics* 2000.

[158] M.H. MacDougal and P.D. Dapkus, "Wavelength Shift of Selectively Oxidized Al_xO_y-AlGaAs-GaAs Distributed Bragg Reflectors", *IEEE Photon. Technol. Lett.* **9** (1997) 884.

[159] H. Kobayashi, R. Takahaski, Y. Matsuoka and H. Iwamura, "1 Tbit/s demultiplexing using low temperature grown InGaAs/InAlAs multiple quantum wells", *Electron. Lett.* **34** (1998) 908.

[160] K.L. Hall, G. Lenz, A.M. Darwish and E.P. Ippen, "Subpicosecond gain and index nonlinearities in InGaAsP diode lasers", *Opt. Commun.* **111** (1994) 589.

[161] R. Hess, M. Caraccia-Gross, W. Vogt, E. Gamper, P.A. Besse, M. Duelk, E. Gini, H. Melchior, B. Mikkelsen, M. Vaa, K.S. Jepsen, K.E. Stubkjaer and S. Bouchoule, "All-Optical Demultiplexing of 80 to 10 Gbit/s Signals with Monolithic Integrated High-Performance Mach-Zehnder Interferometer", *IEEE Photon. Technol. Lett.* **10** (1998) 165.

[162] D. Cotter, R.J. Manning, K.J. Blow, A.D. Ellis, A.E. Kelly, D. Nesset, I.D. Phillips, A.J. Poustie and D.C. Rogers, "Noninear Optics for High-Speed Digital Information Processing", *Science* **286** (1999) 1523.

[163] A.E. Siegman, *Lasers* (Mill Valley, CA: University Science Books) 1986.

[164] M.J. Adams, D.A.O. Davies, M.C. Tatham and M.A. Fisher, "Nonlinearities in semicondcutor laser amplifiers", *Opt. and Quantum Electron.* **27** (1995) 1.

[165] R.J. Manning, A.D. Ellis, A.J. Poustie and K.J. Blow, "Semiconductor laser amplifiers for ultrafast all-optical signal processing" *J. Opt. Soc. Am. B* **14** (1997) 3204.

[166] N.S. Patel, K.L. Hall, and K.A. Rauschenbach, "Interferometric All-Optical Switches for Ultra-Fast Signal Processing", *Applied Optics* **37** (1998) 2831.

[167] N.S. Patel, K.L. Hall, and K.A. Rauschenbach, "40-Gbit/s cascadable all-optical logic with an ultrafast nonlinear interferometer", *Opt. Lett.* **21** (1996) 1466.

[168] S.W. Corzine, R-H. Yan, and L.A. Coldren, in *Quantum Well Lasers*, edited by P.S. Zory, Jr. (Academic, San Diego) 1993, pp. 17-96.

[169] BPM_CAD, Waveguide Optics Modelling Software System, Version 3.0, Optiwave Corporation, 1997.

[170] J.B.D. Soole, C. Caneau, H.P. LeBlanc, N.C. Andreadakis, A. Rajhel, C. Youtsey and I. Adesida, "Suppression of Modal Birefringence in InP-InGaAsP Waveguides Through Use of Compensated Tensile Strain", *IEEE Photon. Technol. Lett.* **9** (1997) 61.

[171] C.H. Henry, in *Quantum Well Lasers*, edited by P.S. Zory, Jr. (Academic: San Diego)1993, pp.1-16.

[172] M.A. Newkirk, B.I. Miller, U. Koren, M.G. Young, M. Chien, R.M. Jopson and C.A. Burrus, "1.5 μm multiquantum-well semiconductor optical amplifier with tensile and compressively strained wells for polarization-independent gain", *IEEE Photon. Technol. Lett.* **4** (1993) 406.

[173] D. Sigogne, A. Ougazzaden, B. Mersali, J. Landreau, C. Amra and A. Ramdane, "1.55 μm Polarisation Insensitivie InGaAsP Strained MQW Optical Amplifier with a High Confinement Factor", *Proc. 21st Eur. Conf. on Opt. Comm.* (ECOC '95) p. 267.

[174] F. Seiferth, F.G. Johnson, S.A. Merritt, S. Fox, R.D. Whaley, Y.J. Chen, M. Dagenais and D.R. Stone, "Polarization Insensitive 1.55-μm Optical Amplifier with GaAs Delta-Strained $Ga_{0.47}In_{0.53}As$ Quantum Wells", *IEEE Photon. Technol. Lett.* **9** (1997) 1340.

[175] Y. Suzuki, H. Iwamura, T. Miyazawa and O. Mikami, "A Novel Waveguided Polarization Mode Splitter Using Refractive Index Changes Induced by Superlattice Disordering", *Electron. Lett.* **30** (1994) 1794.

[176] J.J.G.M. van der Tol, J.W. Pedersen, E.G. Metaal, J.J.-W. van Gaalen, Y.S. Oei and F.H. Groen, "A Short Polarization Splitter Without Metal Overlayes on InGaAsP-InP", *IEEE Photon. Technol. Lett.* **9** (1997) 209.

[177] D.K. Bowen and B.K. Tanner, *High Resolution X-ray Diffractometry and Topography* (London: Taylor and Francis) 1998.

[178] C. Kittel, *Introduction to Solid State Physics* (New York: John Wiley and Sons, Inc.) 1996.

[179] P.F. Fewster, "X-ray diffraction from low-dimensional structures", *Semicond. Sci. Technol.* **8** (1993) 1915.